UCLouvain

FACULTE DES SCIENCES

Faculté des sciences

Master [120] à finalité approfondie

TOWARDS HYDROGEN PHOTOPRODUCTION BY IRON COMPLEXES

Author : ULYSSE FERIER

Supervisors : Pr. Ludovic TROIAN GAUTIER, Pr. Benjamin ELIAS

Readers: Pr. Michel DEVILLERS, Pr. Daniel ESCUDERO, Pr. Raphaël ROBIETTE

Academic year 2022-2023

Master [120] in advanced Chemistry

Acknowledgments

During this year, many people have helped me to carry out this work, and I cannot express how grateful I am to them.

First of all, I would like to thank Professors B. Elias and L. Troian-Gautier for their help with this master thesis. I immediately felt very welcome in their team and they always supported me in my research. I've lost count of the number of times I've stopped by their offices unannounced to ask questions, which have always been kindly answered.

In addition, I would really like to thank the team of PhD students – Milan, Noémie, Martin x3 and Simon – who have supported me throughout this task, and whom I consider to be my friends with which I hope to work with in the future.

Finally, I would especially like to thank Alexia Ripak for her commitment to my master thesis. I'm particularly grateful for the time she took to proofread the many drafts of this work, the number of times she helped me analyse my data and the number of hours she spent discussing future reactions to test. I'm really pleased to have met her and I'll keep very pleasant memories of this year.

And to all the people who supported me in their own way for this thesis, to the cleaning staff in the laboratories, to the administrative staff, to my family, to my friends, to my classmates,

Thank you, from the bottom of my heart.

Summary

Over the lasts decades, Humanity started facing one of its biggest threats: itself. We are currently destroying our planet by the overconsumption of fossil fuels that emit tremendous quantities of pollutant. It is becoming an urge to develop new technologies to replace our energy consumption habits, with the aim of a more ecological energy production.

Nowadays, the solar energy is targeted by numerous works, as it is cheap, abundant and eco-friendly. This energy is already being used for many applications, but the most relevant one is clearly the silicon-based solar panels. However, these are not the only technology that has been developed to harvest light energy. Gratzel cells, known as *dye-sensitized solar cells* (DSSC), are also capable of producing electricity directly from light by the use of photosensible dyes. However, as the electricity production seems nearly perfected for silicon panels, it would be pointless to try replacing them and we should aim to use the DSSC technology differently.

Indeed, the photoproduction of high energetical fuels (*Solar Fuels*) directly by converting solar energy into chemical bonds is possible through the use of *dye-sensitized photoelectrochemical cells* (DSPEC). These cells are receiving an increasing interest in literature as they may offer an eco-friendly solution to produce tomorrow's energy, which motivated us to research on that subject.

As one of the main concerns of such cells is the scarcity of Ruthenium used for the dyes, here, we tried to develop now cheap Iron-based dyes to overcome this scarcity issue. Very recently, Wärnmark's group developed a new Iron(III) complex exhibiting a nanosecond excited state, which is a breakthrough for such complexes.

In this work, we aim to functionalise this new structure by adding anchoring groups, in a larger objective of building the very first electrochemical cells based on these complexes.

Résumé

Au cours des dernières années, l'Humanité a commencé à faire face à sa plus grande menace : elle-même. Nous sommes en train de détruire les ressources de notre planète par la surconsommation d'énergie fossiles, qui émettent d'énormes quantités de polluants. Il devient urgent de développer de nouvelles technologies pour remplacer nos habitudes de consommation, avec pour but la production d'énergie plus *eco-friendly*.

Ces dernières années, l'énergie solaire a été l'objet de nombreuses recherches grâce à son faible prix, son abondance et son faible impact sur l'environnement. Cette énergie est déjà utilisée pour de multiples applications, mais la plus développée reste les panneaux solaires à base de silicium. Cependant, cette technologie n'est pas la seule à avoir été inventée pour récolter l'énergie solaire. En effet, les *cellules à pigments photosensibles* (DSSC) sont aussi capables de produire de l'électricité en convertissant directement l'énergie solaire par des pigments photosensibles. Cependant, vu que la production d'électricité semble perfectionnée pour les panneaux à silicium, il serait vain de vouloir les remplacer. La technologie des DSSC devrait donc être utilisée différemment.

En effet, la photoproduction de carburants à haute valeur énergétique (*Solar Fuels*) en transformant l'énergie solaire en énergie chimique est possible grâce aux *cellules photoélectrochimiques* (DSPEC). Ces cellules solaires reçoivent un intérêt croissant dans la littérature car elles pourraient offrir une solution respectueuse de l'environnement pour subvenir à nos besoins énergétiques.

Vu que l'un des principaux problèmes de ces cellules est la rareté du Ruthénium utilisé dans les pigments, ce travail est axé sur la possibilité d'utiliser des pigments à base de fer, peu coûteux, pour contrer ce problème de rareté. Très récemment, l'équipe de Wärnmark a développé un complexe de fer présentant des états excités d'un temps de vie atteignant la nanoseconde, ce qui est très rare pour ce genre de structure. Ainsi, la fonctionnalisation de ces structures sera étudiée de façon expérimentale et théorique, pour y ajouter des groupements d'ancrage sur surface, dans un objectif plus large de produire les premières DSPEC sur base de ces complexes.

Table of contents

Illustration table

List of abbreviations

DSSC	Dye Sensitized Solar Cell
TCO	Transparent Conductive Oxide
ITO	Indium-doped Transparent Oxide
FTO	Fluor-doped Transparent Oxide
S	Photosensible compound
hv	Light
k_{inj}	Electron injection rate constant
DSPEC	Dye Sensitized Photo Electrochemical Cell
nm	Nanometre
Cat	Catalyst
CB	Conduction Band
VB	Valence Band
e^-	Electron
$Wm^{-2}/\mu m^{-1}$	Watt per surface unit
HOMO	Highest Occupied Molecular Orbital
LUMO	Lowest Unoccupied Molecular Orbital
ES	Excited State
bpy	2-2'-Bipyridine
MLCT	Metal to Ligand Charge Transfer
MC	Metal Centred
LC	Ligand Centred
GS	Ground State
IR	Infrared
NCS	Isothiocyanato
MO	Molecular Orbital
TBA	Tertiary Butyl Alcohol
IPCE	Incident Photon to Current conversion Efficiency
Dq/B	Magnitude of the splitting energy
$r_{(M-L)}$	Metal to ligand radius
ISC	Inter System Crossing
CT	Charge Transfer
ps	Picosecond
IC	Internal Conversion
btz	3,3′-dimethyl-1,1′-bis(p-tolyl)-4,4′-bis(1,2,3-tri-azol-5-ylidene)
LMCT	Ligand to Metal Charge Transfer
UV	Ultra Violet
NHC(s)	N-heterocyclic carbene(s)
$E_{x/x}$	Potential
eV	Electron Volt
NHE	Normal Hydrogen Electrode
pH	Potential of Hydrogen
DFT	Density Functional Theory
MO_x	Metal Oxide
kcal/mol	Kilocalorie per mol
phtmeimb	Tris(3-methyl-1H-imidazol-3-ium-1-yl)(phenyl)borate
phC_5	Phenyl Pentyl group

C_9	Nonyl group
PO_3H_2	Phosphonic acid group
P-C	Phosphorus Carbon
PPh_3	Triphenyl Phosphine
dppf	Diphenylphosphino ferrocene
TD-DFT	Time Dependent Density Functional Theory
3D	Three dimensional
BS	Basis Set
PCM	Polarizable Continuum Model
°C	Celsius degree (temperature unit)
h	Hours
min	Minutes
eq	Equivalent
HMDS	Hexamethyldisilazane
TMS	Trimethylsilyl
RT	Room Temperature
TMSCl	Trimethylsilyl Chloride
THF	Tetrahydrofurane
BHT	Butylated hydroxytoluene
PhTMS	Phenyl-trimethylsilyl
LiHMDS	Lithium bis(trimethylsilyl)amide
Et	Ethyl
BrPhTMS	(4-bromophenyl)trimethylsilane
NMR	Nuclear Magnetic Resonance
Me	Methyl
n-BuLi	n-Butyllithium
SN_2	Second order Nucleophilic Substitution
COSY	Correlation Spectroscopy
ppm	Part per million (NMR unit shift)
MS	Mass Spectrum
g/mol	Gram per mol
HPLC	High Performance Liquid Chromatography
XCF	Exchange Correlation Functional
MHz	Mega Hertz
mL	Millilitre (volume unit)
mmol	Millimole (quantity of matter unit)
g	Gram (Mass unit)
s	Singlet
d	Doublet
t	Triplet
dd	Doublet of Doublet
LLCT	Ligand to Ligand Charge Transfer

Part I

Introduction

1 Context

Humanity is in danger. As we all know, Earth's supplies are limited, and a day will come when we will no longer have access to fossil fuels. Moreover, Humanity is continuously increasing its energy demand which is still supplied by non-renewable sources such as gas, oil and coal[1,2] – (**Figure 1.a**). The use of such energy sources emits tremendous quantities of pollutants that inevitably contribute to climate crisis. Indeed, we are facing a constant rise of CO_2 emissions throughout the years, which is among the gases linked to global warming – (**Figure 1.b**).

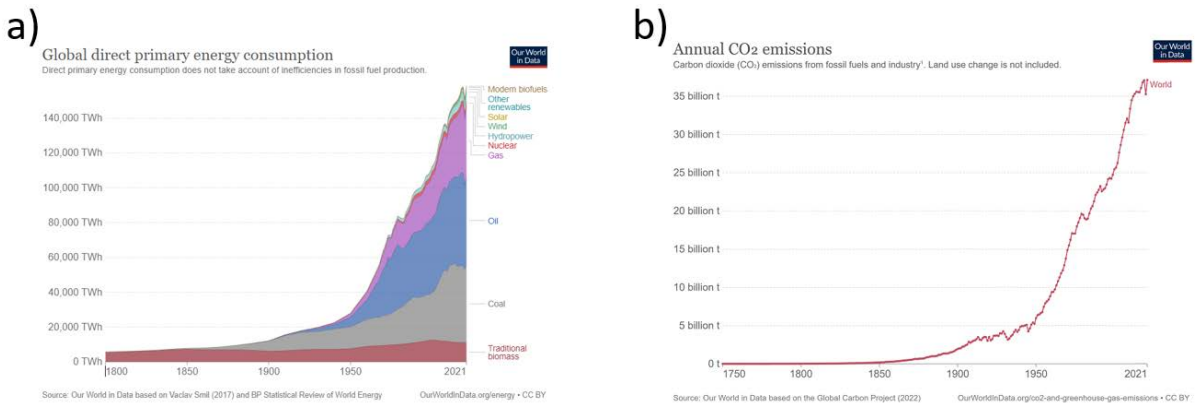

Figure 1: a) Global direct primary energy consumption by Humanity from year 1800 to 2021; b) Annual CO_2 emission from 1750 to 2021.

Therefore, it is becoming urgent to develop new renewable technologies to produce the energy of tomorrow. Cost-effective, eco-friendly and abundant energy is already the aim of numerous research around the globe. This work will be focused on the development of novel solar technologies based on Iron photosensitizers that may one day be used for energy production.

2 Solar technologies

2 . a . Current solar energy production

The 21st century is already marked by the expansion of solar technologies that already produce 1,5% of the world's consumed energy [3]. Moreover, a great increase of solar power generation is seen in nearly all developed countries around the world, which indicates a growing interest for such technologies (**Figure 2**).

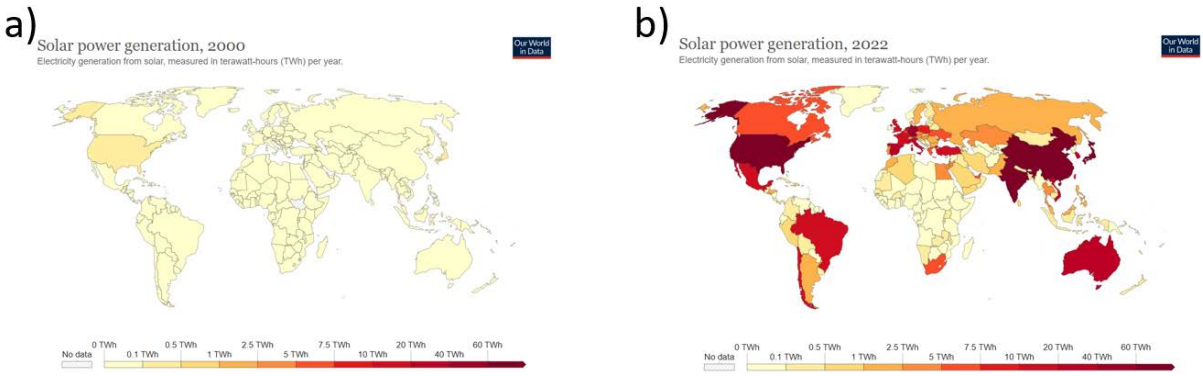

Figure 2: World map of solar power generation in a) 2000 and b) 2022 [3].

Today, most of the solar-generated electricity comes from silicon-based panels. To produce electricity, the panels are made of two types of semiconductors (*n*- and *p*-types). Both are silicon layers doped with atoms containing one electron less (such as boron or gallium) or more in their valence shell than silicon (like phosphorus or selenium), forming *p*-type and *n*-type layers respectively. Therefore, in the semiconductor structure, the *p*-type layer acts as electron holes whereas the *n*-type layer serves as electron donor [4,5].

A silicon based solar cell typically consists of repeated *p*- to *n*-type layers. At the junction of the two layers, also called PN junction, electrons of the *n*-doped side will fill the holes of the *p*-layer via *electron diffusion*. This creates an area called the depletion zone (**Figure 3 – left closeup**).

When all the holes are filled, the *n*-side of the depletion zone now contains positive charges while the *p*-side contains negative ones. The presence of opposite charged ions creates an internal electric field that prevents more *n*-type electrons to fill holes in the *p*-layer (the equilibrium is fulfilled when the induced electric potential is strong enough to prevent more electron to diffuse up to the *p*-layer).

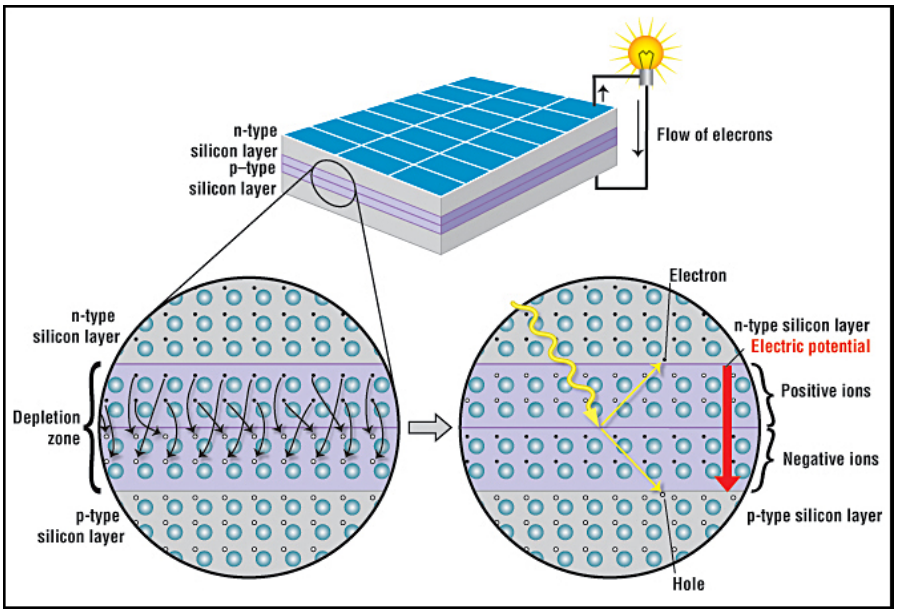

Figure 3: Representation of a silicon-based solar panel [4]. Note that the electric potential shown on the right closeup is noted following physics conventions.

When sunlight strikes the cell, electrons are ejected from the silicon atoms. If this happens in the PN junction, electrons will move to the positive *n*-type layer while holes will be displaced to the *p*-layer. The two layers being linked by a conductive connection, charge recombination will happen by passing through the connected electric circuit therefore producing electricity (indeed, as the electric potential is pointing towards the *p*-type layer, electrons will have no choice than passing through the connection to fulfil the hole (**Figure 3 – right closeup**).

Although these cells are the most used, they are not the only ones to have been invented. Indeed, photosensitive dye-based cells – known as Gratzel cells – are also capable of producing electricity. Moreover, as it will be presented in this work, their design led to the production of cells capable of directly transform solar energy into chemical bonding, which is the main interest of this work.

2 . b . Gratzel cells

Gratzel cells (or Dye-Sensitized Solar Cells, *DSSCs*), first developed in 1991 by Michael Gratzel and Brian O'Regan, are inspired from natural photosynthesis systems and use photosensitizers instead of silicon semiconductors as light harvesters[6]. These cells are built up as following (**Figure 4.a**): i) a transparent anode made up with

a conductive glass sheet treated with a transparent conductive oxide layer (TCO, where Indium-doped Tin Oxide -ITO- or Fluorine-doped Tin Oxide -FTO- are typically used); ii) a mesoporous semiconductor (typically TiO_2 or SnO_2) deposited on the anode to increase the specific surface; iii) a monolayer of photosensitive dyes adsorbed on the surface to increase light absorption; iv) an electrolyte solution containing a redox mediator (such as the I_3^-/I^- couple) in an organic solvent for the dye regeneration and v) a cathode made of conductive glass sheet coated with a catalyst (typically platinum) to facilitate electron collection [6,7].

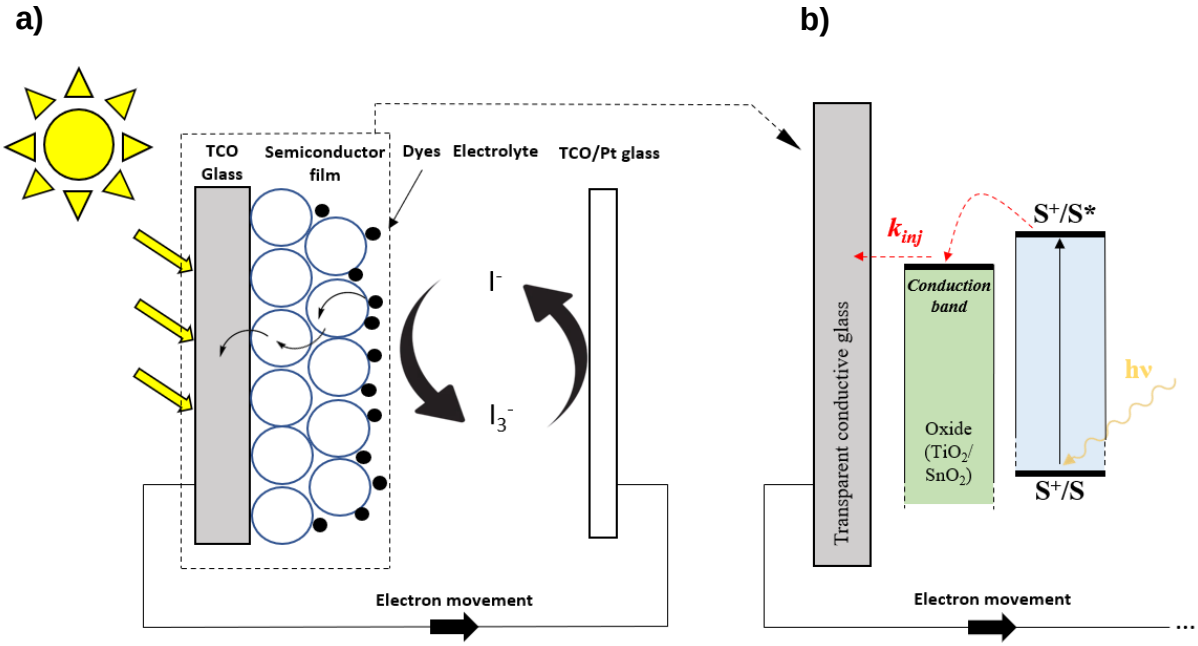

Figure 4: Schematic representation of a) a Gratzel cell and b) electron injection at the photoanode. Adapted from [6,7].

Upon irradiation, the photosensitizer reaches an excited state (one electron is promoted to a state of higher energy than the ground-state), allowing the electron to be injected in the conduction band of the semiconductor (**Figure 4.b**). Then, this electron will move to the cathode where the I_3^- mediator will be reduced to I^-. The dye is regenerated by oxidizing the mediator back to its I_3^- form and thus closing the cycle.

As mentioned before, this technology paved the way to the development of another type of cell: the DSPECs (Dye-Sensitized Photo Electrochemical Cells). These cells are capable of directly using light as energy source for oxidation/reduction reactions. Indeed, *solar fuels* (high energetical synthetic fuel directly produced from solar energy)

can be produced by them, with water splitting for example (to yield only dihydrogen and oxygen). The next section is devoted to them.

2 . c . Dye-sensitized photoelectrochemical cells

In the last ten years, DSPECs have gone from proof of concept[8], to the achievement of the first photocurrent production[9], as well as great photostability [10,11,12]. Such cells may be capable to produce the required *solar fuels* to sustain the next generation's energetic demand and currently receive tremendous interest in literature[13,14]. Despite having numerous applications, only the H_2 photoproduction will be considered in this work.

Historically formed by gas reforming[15], scientists now aim to synthesize H_2 by complete water splitting, only yielding O_2 as a side product. This splitting process was first performed by Fujishima's and Honda's team in 1972[16] upon irradiation of a titanium oxide electrode (at 415 nm - which is equivalent to its band gab), that subsequently allows water oxidation. Nowadays, photochemists try to improve light-driven water splitting by matching the sunlight's spectrum, by DSPECs designs. These are producing dihydrogen as following [17, 18] – **Figure 5:**

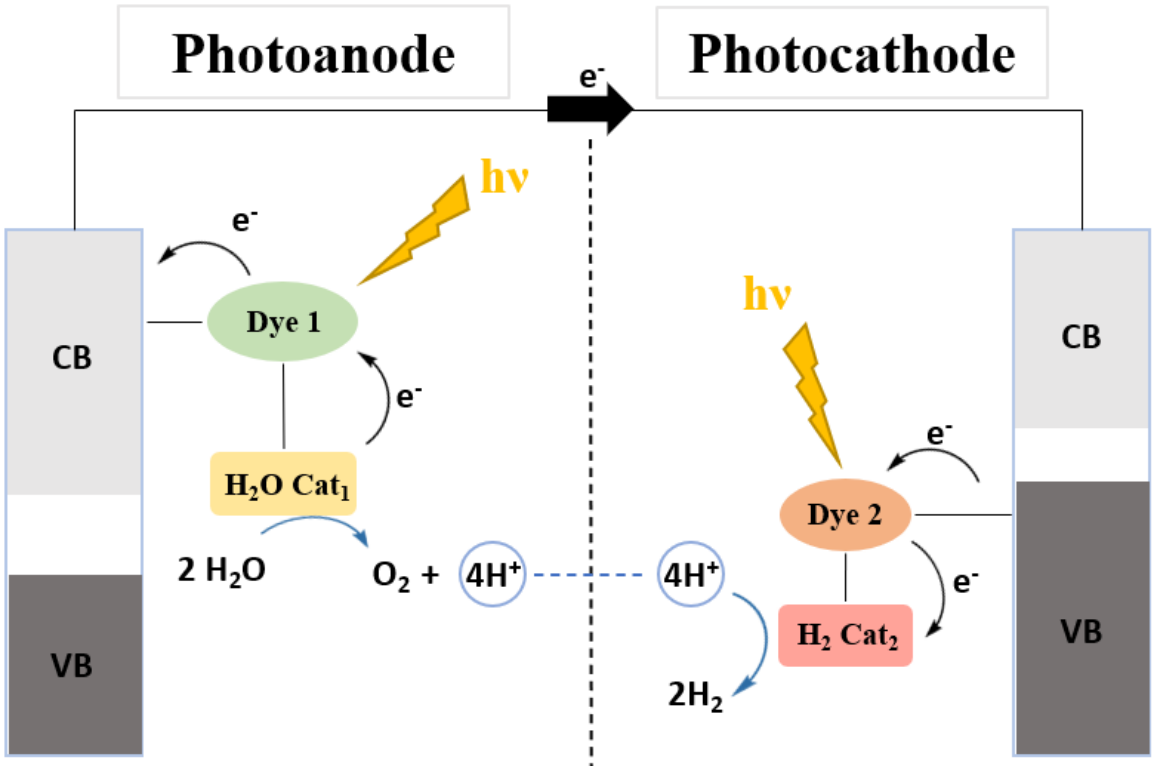

Figure 5: Schematic representation of a typical tandem-based DSPEC for water splitting. Adapted from [17,18].

Initially, **Dye 1** on the photoanode is excited and an electron is injected into the conduction band of the semiconductor (same process as for DSSCs – see above) thus gaining a positive charge. The dye is regenerated by oxidizing the **H_2O Cat$_1$**, a catalyst which will yield oxygen and protons by oxidizing water. Simultaneously, **Dye 2** on the photocathode will absorb light and inject an electron to **H_2 Cat$_2$** which is now capable of reducing protons to hydrogen. **Dye 2** is regenerated by oxidising the semiconductor where it is adsorbed, itself being regenerated by the injected electron coming from the photoanode [17,18].

As DSPECs aim to use sunlight irradiance, they must be able to convert the majority of the solar spectrum, regardless of the wavelengths [12] (in comparison to Fujishima and Honda's first water splitting cell, that could only operate with 415 nm or more energetic irradiation). Thus, as the sunlight covers principally the 300 – 1000 nm region (**Figure 6**), the cell should have the capacity to absorb any photons in this range.

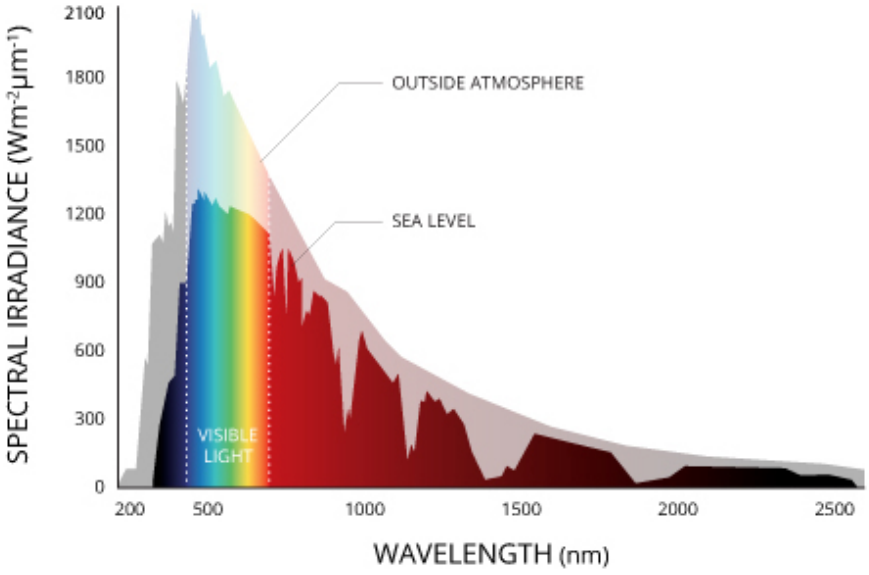

Figure 6: Solar irradiance correlated to the light wavelengths[19].

However, these DSPECs suffer from various drawbacks: i) photons with lower energy than the HOMO-LUMO gap (Highest Occupied Molecular Orbital and Lowest Unoccupied Molecular Orbital) of the photosensitizer will not be absorbed as they do not offer enough energy to excite the dyes (**incomplete absorption**); ii) excess of energy (higher energy photons than the HOMO-LUMO gap) will also be lost by heat production during the relaxation to the lower Excited State (ES), i.e. the ES from which the photo-triggered process will take place (**thermalization**); iii) some fraction of the

ES energy is necessarily lost upon formation of dihydrogen to ensure a thermodynamically favoured reaction (**overpotential**) and iv) a small fraction of the ES will undergo emission, thus losing their acquired energy[12] (**radiative recombination**).

Therefore, it is essential to correctly design the different components of such cells to maximize photoproduction. As a great deal of their efficiency and functioning rely on the dyes used to inject electrons, the next section will be devoted to them in order to understand what happens upon light absorption, i.e. their photophysics.

3 Photosensitive dyes

3 . a . Ruthenium complexes

Historically, Ruthenium-based dyes were the first to be used as they quickly stood out with their excellent photophysical properties[6]. Therefore, they will be treated in this section.

The reference in Ruthenium complexes for any application (solar cells and others) is the prototypical $[Ru(bpy)_3]^{2+}$ complex[20] (**Figure 7.a**) which has undergone numerous researches and its properties are now well-known (its simplified molecular orbitals scheme is presented in **Figure 7.b**). Modifications of this scaffold led to the synthesis of more sophisticated dyes which will be presented hereafter.

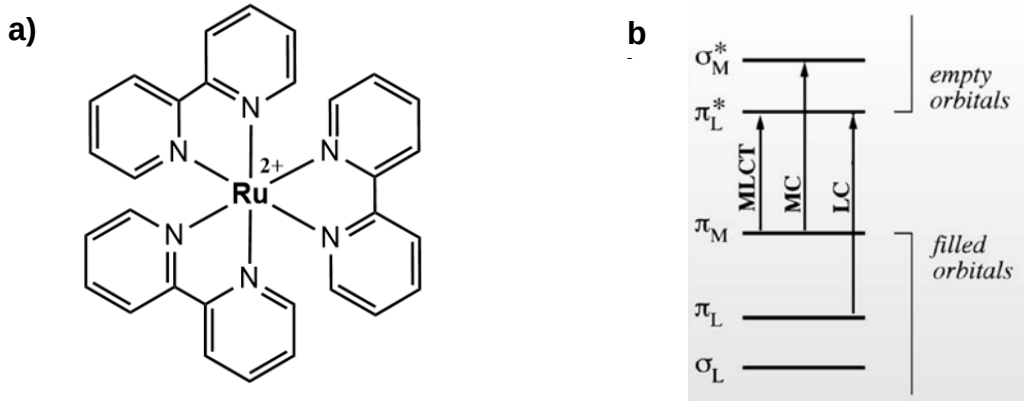

Figure 7: a) $[Ru(bpy)_3]^{2+}$ structure and b) a representation of its simplified molecular orbitals[20].

$[Ru(bpy)_3]^{2+}$ is composed of a d^6 Ruthenium(II) metal centre and polypyridines ligands. These ligands have σ-donors orbitals localized on the nitrogen with π-donors and π*-acceptor orbitals delocalized on the aromatic rings. The complex has a D_3

symmetry and is therefore chiral. When excited, the promotion of an electron from the π_M orbital (metal-centred π orbital, HOMO) to the π_L^* (ligand-centred π orbital, LUMO) leads to a Metal-to-Ligand Charge Transfer (MLCT) transition. Other transitions can be observed such as the promotion of an electron from π_M to σ_M^* or π_L to the π_L^* orbitals via a Metal-Centred (MC) or Ligand-Centred (LC) transitions respectively (**Figure 7.b**). As the molecular orbitals of the bipyridines are the most stable, the MLCT state is more likely to happen following Kasha's rule[20] (which dictates that the photochemical and photophysical properties are determined only by the lowest-lying excited state). Note that the Ligand-to-Metal Charge Transfer (LMCT – the excited electron is sent from the ligand to the metal centre) and Ligand-to-Ligand Charge Transfer (LLCT – the excited electron is sent from a ligand to another ligand) transitions are also possible for certain structures, which is not represented on **Figure 7**.

From this perspective, it is clear that the energy relationship between the different ES of a complex determines its behaviour. MC-type complexes are not suited for electron-injection applications whereas Charge Transfer (CT) types are more interesting due to the photo-induced electron directionality in one case and not the other. To tune a complex and select the type of transition required, the photochemist can rely on the ligand field strength, redox properties of ligands/metals and the intrinsic properties of the ligands (other parameters such as solvatochromism or temperature can also influence the overall properties but they will not be studied in this work).

Thus, for a given metal, the properties are mostly determined by the ligands. Also, as Ruthenium is a heavy metal, fast intersystem crossing (ISC) between the singlet and triplet states is possible, therefore allowing the $[Ru(bpy)_3]^{2+}$ complex to undergo emitting ^{3}MLCT states (triplet states typically exhibit long-lived ES due to the Ground State (GS) relaxation that must pass through spin-forbidden transitions, that considerably increase the ES lifetimes up to the µs regime).

Considering the photosensitizers used for DSSCs and/or for DSPECs, they must meet several requirements to produce a photocurrent. Firstly, they should be able to absorb a maximum of the incident light below the near-IR wavelengths (300 to 920 nm) to match the sunlight spectrum. However, their LUMO must still match with the edge of the semiconductor's conduction band to reduce the energetical potential losses during the electron transfer reaction (**Figure 4.b, "k_{inj}"**). In addition, the HOMO must be sufficiently low to accept electron donation from the electrolyte. Moreover, they must

be functionalized to be easily anchored to the semiconductor surface (developed in section I.4) and must be (photo)stable over time, to ensure years of sunlight exposure without apparent degradation [20].

$[Ru(bpy)_3]^{2+}$ does not fully meet these criteria as it cannot be chemically anchored on surface and its absorption spectrum has to be expanded. Therefore, addition of carboxylic or phosphonic acids on the bipyridines ligands allowed to tackle the first limitation (**anchoring**), and isothiocyanato groups (NCS) were added as their offer π-acceptor orbitals that strongly interact with Ruthenium (**absorption range expand**) which gave mixed molecular orbitals (MO). All taken together, this led to the synthesis of the N3 dye and the black dye (**Figure 8**) which both meet the previous requirements[6]:

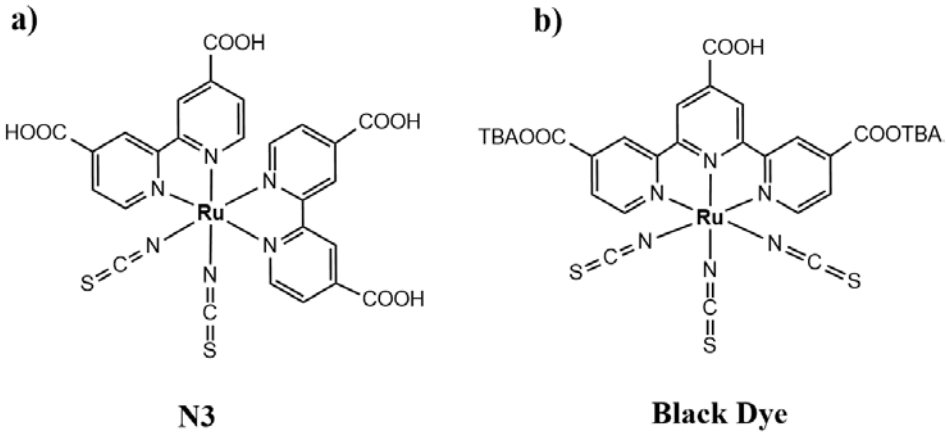

Figure 8: Chemical structures of photosensitizer a) N3 and b) the "Black dye" [6].

For example, *cis*-bis(isothiocyanato)bis(2,2′-bipyridyl-4,4′-icarboxylato)ruthenium(II) – **Figure 8, N3 dye** – became the paradigm of efficient charge-transfer sensitization for nanocrystalline TiO_2 films. Its absorption threshold is around 800 nm and covers the visible to near-infrared region of the solar spectrum. In addition, the carboxylate groups used to anchor on the semiconductor surface act as electron channel, allowing the photo-excited electron injection through it. As the molecular electronic transition is a MLCT, this structure is energetically favoured in the electron injection process. Finally, the dye is reported to undergo more than 10^8 turnovers without loss of performances, which indicates a very good photostability[21].

Such properties were unmatched until the discovery of the *Black dye*, which increased the absorption threshold by covering a spectral region from 100 to 900 nm.

To compare the efficiency of the dyes with one-another, the Incident Photon to Current conversion Efficiency (IPCE) can be used, as it is a measure of the photocurrent ratio (converted in an electron transfer rate) versus the incident rate of photons (from a power-calibrated light source) as a function of wavelength[6]. The IPCE of the N3 and *Black dye* are reported in **Figure 9**.

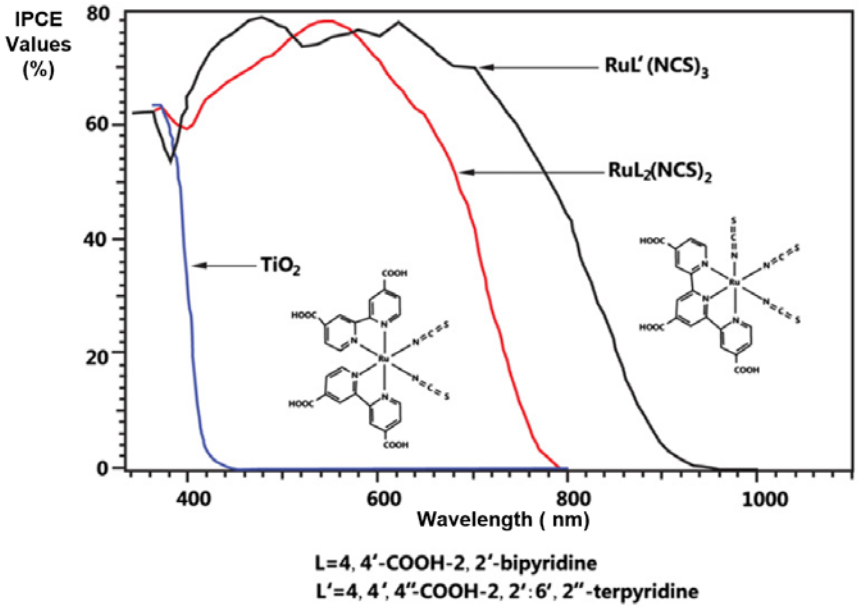

Figure 9: IPCE of TiO2 (blue), N3 (red) and "Black dye" (black) sensitizers[6].

As shown in **Figure 9**, the IPCE of TiO_2 alone is not efficient enough to cover sunlight's spectrum without any sensitizer as it only absorbs until 420nm. The addition of the dyes positively increases the overall IPCE values as well as the wavelength covering. Indeed, the *Black dye* increases the overall IPCE values and extends its spectrum covering up to near-IR region.

Excellent absorption, excellent electron injection, excellent stability, … These dyes seem to have it all! Unfortunately, photochemists will never solve the most predominant problem of such dyes, no matter how much they tune them, which is Ruthenium scarcity[22] (**Figure 10**).

Indeed, Ruthenium is only available at around 1 ppb of Earth's crust mass[23], which directly places him into the so-called Rare-Earth metals alongside Iridium, Osmium or Platinum. Moreover, the extraction cost of Ruthenium is also problematic, as this metal is only found in very diluted minerals, among other metals and impurities. Finally, its purification is also hard to achieve due to its high melting point. All of this explain the

high cost of this material, averaging 15.750€ per kilogram at the end of May 2023[24] . The high cost of Ruthenium as well as the scarcity of the resource therefore prevents it to be used in a high industrial production of DSPECs despite showing interesting properties in the search for new green energies. Consequently, it is becoming an urge to develop new dyes that could replace this metal without decreasing the overall properties of the DSPECs. Dyes that should exhibit similar properties as their Ruthenium counterparts.

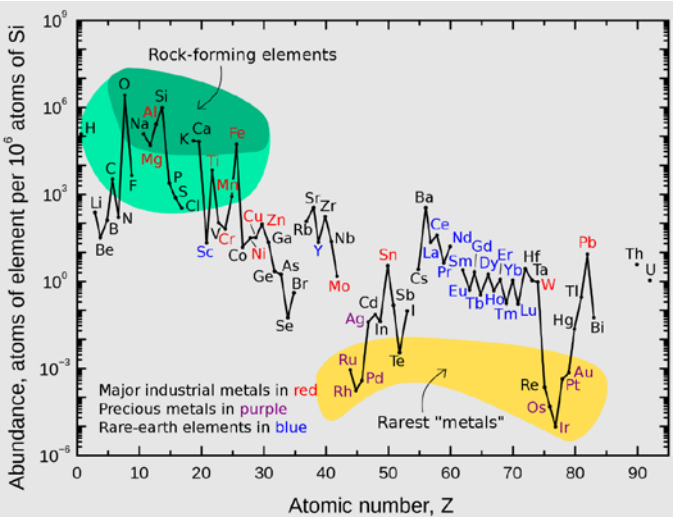

Figure 10: Atom abundances in earth crust per 10^6 atoms of silicon[23].

3 . b . Iron ?

When looking at the periodic table of the elements, Iron is the direct 3d-metal counterpart of Ruthenium. Given the fact that they are located in the same family on the table, Iron should share similar properties with Ruthenium and thus, should be a suitable candidate. In addition, Iron is the fourth most abundant element in the crust [23] (63 000 000 ppb, in comparison to the 1 ppb of Ruthenium, **Figure 10**) and its extraction is really easy, leading to low production costs (0,1051€/kg at the end of April 2023[25]). Iron is also bio-compatible, and many Iron complexes are already used by Nature to do vital reaction pathways such as photosynthesis or oxygen transport[26, 27]. This motivated chemists to research on this atom for photochemical uses and up to now, many Iron-centred organometallic complexes have been developed for this aim[26,28].

Therefore, one can speculate on the future use of this metal in such cells. As presented before, the solution could already be found ? One could simply replace the Ruthenium atoms in the previous structures to yields Iron-centred dyes for DSPECs usages ? Unfortunately, no, as the photophysics of Iron are still very different from its 4d cousin, thus preventing any use in photo-triggered devices. The next section is devoted to highlight their differences.

3 . c . Iron VS Ruthenium

The exited-states of Iron complexes typically tend to deactivate within pico- or femtoseconds, which is way too short to undergo any chemical reaction[29]. To seek any photochemical applications for such complexes, one must counter their short excited-state lifetimes. As an example, the same $[M(bpy)_3]^{2+}$ complex shows a decrease in its excited state lifetime from 1 µs to 150 fs for M = Ru and Fe respectively[30] (**Figure 11**).

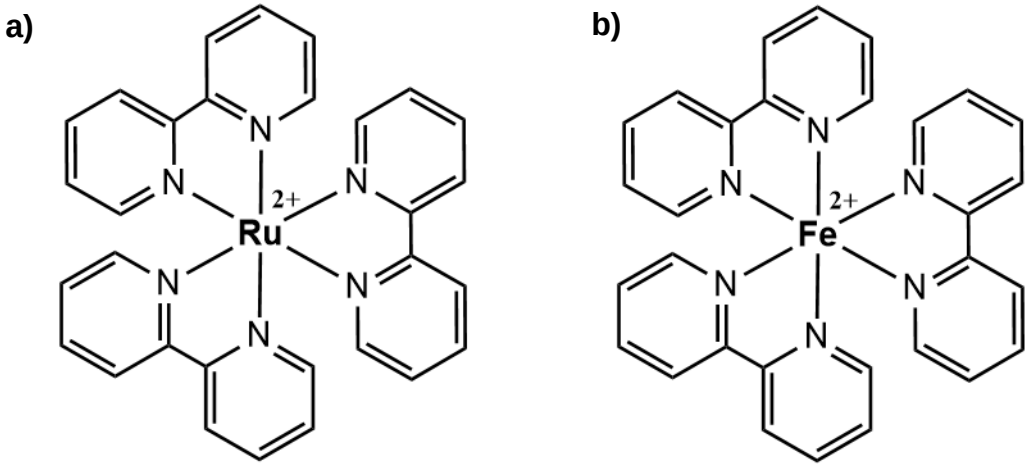

Figure 11: $[Ru(bpy)_3]^{2+}$ and $[Fe(bpy)_3]^{2+}$ complexes [30].

Such ultrafast relaxation time can be explained following the electronic configuration (**Figure 12.a**), Tanabe-Sugano diagram for d^6 complexes (**Figure 12.b**) as well as the simplified potential energy diagrams of $[Ru(bpy)_3]^{2+}$ and $[Fe(bpy)_3]^{2+}$ (**Figure 12.c and d**)[29].

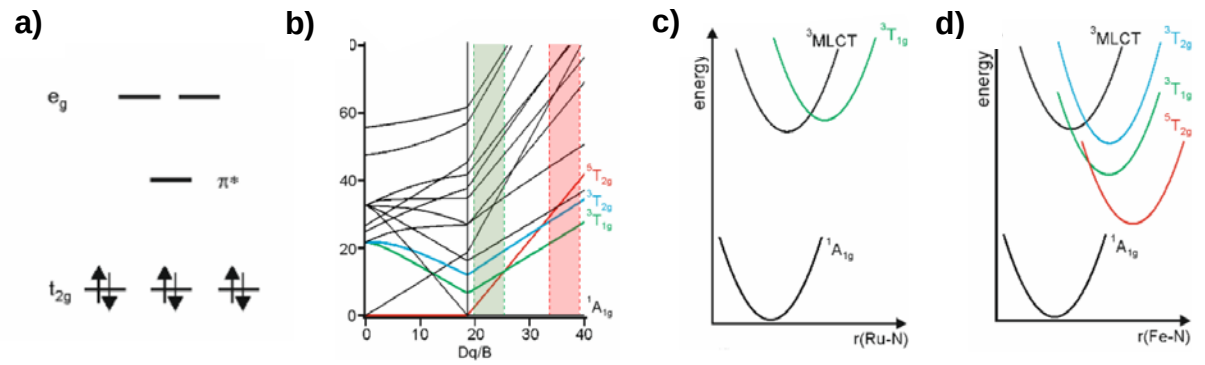

Figure 12: a) Low-spin configuration scheme of d^6 complexes; b) Tanabe Sugano diagram for d^6 complexes; simplified potential diagrams for c) $[Ru(bpy)_3]^{2+}$ and d) $[Fe(bpy)_3]^{2+}$. The highlighted zones of the Tanabe-Sugano diagram are explained in the next paragraphs[29].

For d^6 complexes, strong ligand fields typically achieved with bipyridine ligands (highlighted in red in **Figure 12.b**) result in low-spin configuration (**Figure 12.a**). In $[Ru(bpy)_3]^{2+}$, the t_{2g} - e_g splitting is so large that the π_L^* of the ligands are energetically lower than the e_g of the metal core. Consequently, the lowest ES will be obtained through MLCT transitions (**Figure 12.c**), with the promotion of an electron to the ligand π_L^*, following the spin rule. As mentioned before, heavy metals such as Ruthenium enable fast ISCs, which allows the singlet ES to relax into a triplet one, yielding the long-lived ^{3}MLCT excited states. Also, in the ^{3}MLCT state, the Ru-N distances are only weakly elongated in comparison to the initial A_{1g} ground state as promotion of an electron from non-bonding to antibonding ligand orbitals does not alter much of the metal-ligand bonding distances. This leads to only a small displacement between these two potential wells shown in **Figure 12.c** (see the $^1A_{1g}$ and ^{3}MLCT potential wells). The large energy gap between the two potentials as well as their small mutual displacements favours radiative ES relaxation. Also, this relaxation is in competition with the non-radiative one via the metal-centred $^3T_{1g}$ state derived from the promotion of an electron to the e_g orbital (**Figure 12.c**). In comparison to the ^{3}MLCT state, the potential well of $^3T_{1g}$ is markedly displaced along the Ru-N axis as one electron has moved from a largely non-bonding to an antibonding metal orbital. However, as the MC state is energetically disfavoured, few non-radiative relaxations are observed for this kind of complexes [29].

For Iron, the story is quite different. The metal being smaller with less electrons than Ruthenium, its intrinsic field is lower, leading to smaller e_g-t_{2g} gaps and changing the

situation compared to Ruthenium. Such field strength difference inevitably leads Iron complexes to be in the green zone of the Tanabe-Sugano diagram (**Figure 12. b**), thus stabilising the $^5T_{2g}$, $^3T_{1g}$, $^3T_{2g}$ well potentials (**Figure 12.d**). Moreover, these wells are typically greatly overlapped, leading to ultrafast deactivation by non-radiative vibrational cooling on the picosecond timescale. Any electron promotion to the MLCT state will inevitably come back to the GS within picoseconds by non-radiative deactivation, therefore preventing Iron to have CT-type transitions. Finally, promotion of an electron to MC states leads to bond elongation (which might in turn lead to decomplexation), because an antibonding orbital is filled by a previously non-bonding electron [29].

To bypass this issue that prevents Iron to undergo CT transition, two keys are in our possession. The first one would be ligand field tuning, as the $t_{2g} – e_g$ gap expanding would increase the energy of MC states (thus aiming for the same situation as for Ru(II) complexes, where the π_L^* is lower than the e_g). The second key would be to control the bonding distances between Iron and its ligands, as the MC states strongly displace them. Controlling the bonding distance (and geometry) could increase the displacement energetical cost and in consequence, favouring more CT states which displace them less. The first key could be obtained by adding strong σ-donors and/or π-acceptor ligands, while the second one could be obtained by increasing the ligand denticity. In fact, rigidity is commonly obtained with bi- or tridentate ligands that offer limited degrees of conformation freedom for the metal upon coordination [29].

Several attempts to produce such complexes have been done throughout the past decade [31]. Indeed, polypyridines were initially thought to be good ligand candidates as they offer strong donating effects and good chelating rigidity. Unfortunately, these modifications were not sufficient as only less than ps ES lifetime were obtained (**Figure 13.a**). Scientists then tried to add cyano groups to increase the π-acceptor effect and found out a 10 ps ES lifetime for complex b (**Figure 13.b**). Cyano groups are good candidates to decelerate the internal conversion (IC) decay but tend to interact with solvents, which gave undesirable shifts in the UV-visible spectra, as presented in [11]. Only recently, few examples of Iron complexes with ES lifetime approaching the ns were synthetized, such as $[Fe(btz)_3]^{2+}$ with its 528 ps ES lifetime (btz = 3,3′-dimethyl-1,1′-bis(p-tolyl)-4,4′-bis(1,2,3-tri-azol-5-ylidene) - **Figure 13.c**).

This structure combines strong π-acceptor ligand effects while remaining good σ-donors. Moreover, the use of mesoionic carbenes was enough stabilizing to have Fe(III) complexes exhibiting the firsts LMCT transitions[31]– **Figure 13.c**.

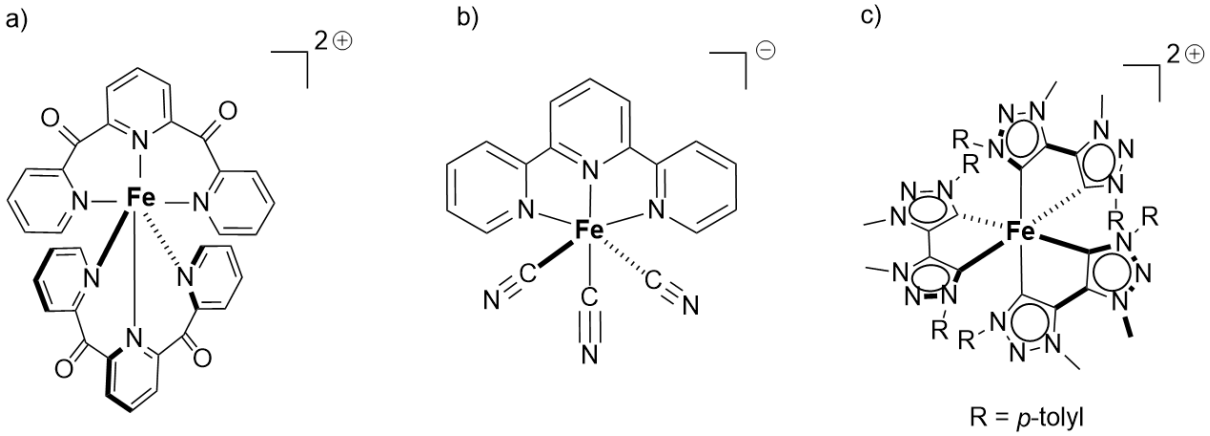

Figure 13: Iron complexes with ES lifetime of (a) less than 1 ps, (b) 10 ps and (c) 528 ps[31].

In 2019, the combination of all the previous learnings on the photophysics of Iron complexes was put together by Wärnmark et al., who synthetized a 2 ns ES lifetime complex with a strong LMCT transition at 502 nm [32]. The structure, absorption and emission spectra of $[Fe(phtmeimb)_2]^+$ (*phtmeimb* = phenyl[tris(3-methylimidazol-1-ylidene)]borate) are presented in **Figure 14.**

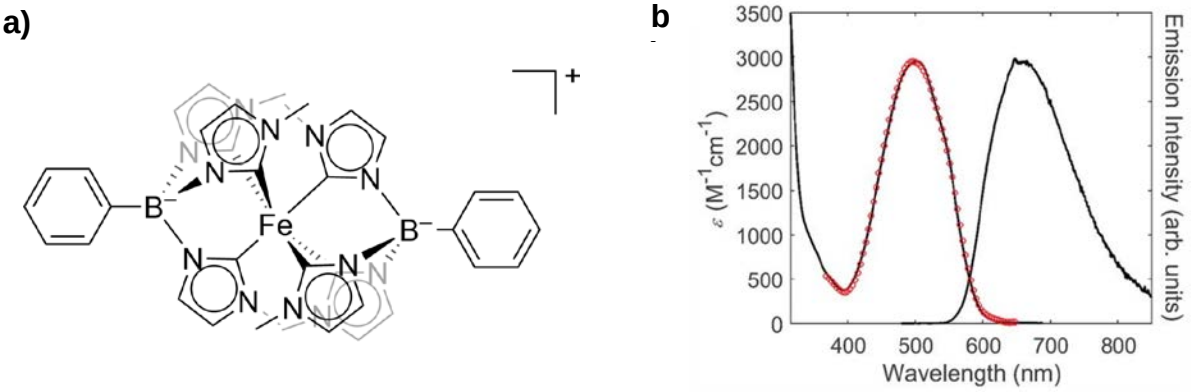

Figure 14: a) Structure of $[Fe(phtmeimb)_2]^+$ and b) its UV-visible absorption (red dotted line) and emission (black line) spectra[32].

This structure combines: i) a strong σ-donor and π-acceptor ligands brought by the N-heterocyclic carbenes (NHCs) in methylimidazoles; ii) a bond-length immobilization by tridentate ligands with strong C-Fe bonding, along with a perfect clamp angle (143°) to give a near-perfect octahedral configuration and iii) a stable Fe(III) centre allowing

LMCT-type transitions. All of these combined results in a distortion of the MC states, rendering them unreachable and thus avoiding fast deexcitation and a higher energy splitting of the orbitals allowing a new ^{2}LMCT excited state. Moreover, the luminescence quantum yield of this complex averages 2.1 % in acetonitrile at room temperature. Also, the redox potentials of this complex are $E_{III/II}$ = -0,51 V at the GS and $E_{III*/II}$ = 1,6 V when excited (vs Normal Hydrogen Electron *NHE*)[32].

However, to ensure the possible use of this structure in future DSSCs of DSPECs, one must ensure a correct adsorption to the surface of the semiconductor, which is described hereafter.

4 Surface Adsorption

4 . a . Covalent bonding

In an ideal case, electron injection from the dye to the semiconductor must be done with minimum loss to obtain high efficiency DSPECs. Typically, the photosensitizer is adsorbed on nanoparticles of semiconductor to maintain the dye close-by[33]. Electron injection also works in solution but will not be discussed in this work.

To be adsorbed on a surface, different options are already well developed and reported in the literature. The most common one is the addition of anchoring groups on the dye to allow chemical bonding to the semiconductor. These links must be able to work under operating conditions (in presence of light, solvents, ions, …) and need to be stable across a wide pH range as protons are generated inside the cell under irradiation in the case of water-splitting (see **Figure 5**). Also, a given anchoring group may not be suited for all applications. For example, dyes anchoring groups must ensure efficient electron injection whereas catalyst anchoring groups must endure long-lived charges as they commonly accumulate them for water oxidation.

Considering the previous statements, most anchoring groups used in DSSCs are not suited for DSPECs, as they do not have the same working conditions. Moreover, DSSCs generally employ organic solvents which do not require strong adsorption strength to operate successfully. Therefore, only few anchoring groups that meet the DSPECs requirements have been discovered and are presented in **Figure 15**.

The phosphonic and carboxylic acids are the most commonly used for such applications and will be the only ones described hereafter[33].

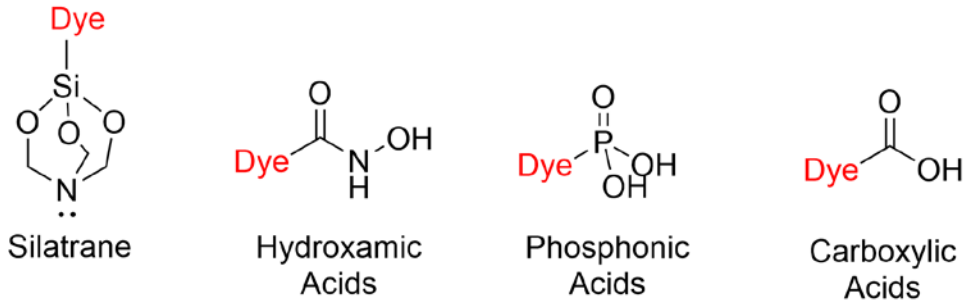

Figure 15: Anchoring groups used for dye anchoring in DSPECs[33].

In contact with the semiconductor (TiO_2 or SnO_2), carboxylic and phosphonic acids are capable of covalent bonding such as presented in **Figure 16**. Interestingly, each one has different bonding denticity, with bidentate bridging favoured for both. Experimentally, the bridging denticity is measured by infrared spectroscopy, with the C=O/P=O peak stretching bands disappearing while observing variations with C-OH/P-OH bands. DFT (Density Functional Theory) calculations are also capable of predicting anchoring denticity but remains uncertain in some cases.

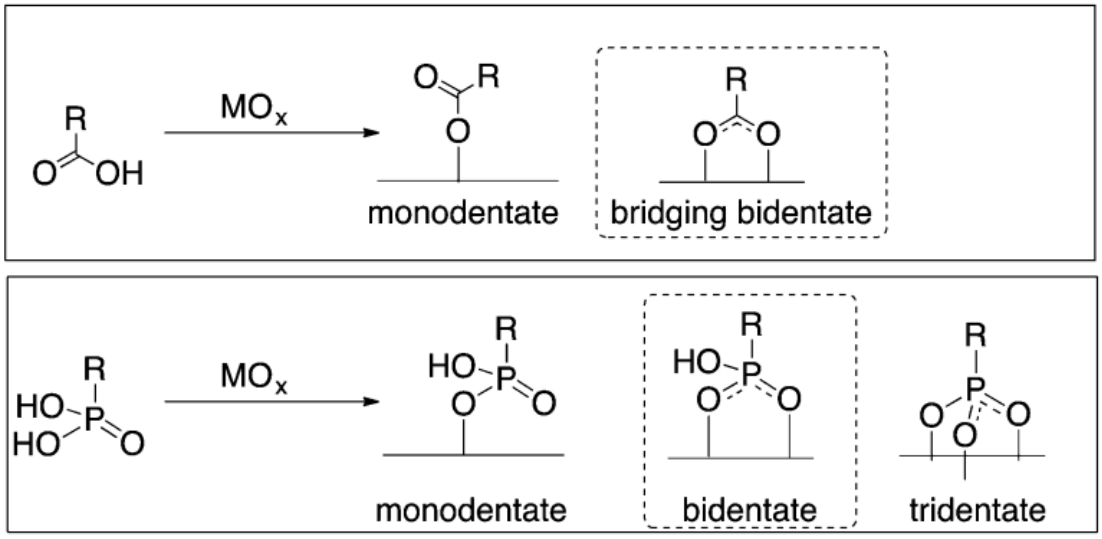

Figure 16: Bonding schemes of carboxylic and phosphonic acids onto a semiconductor surface (MOx on the figure)[33]. Note that different molecular representations for the phosphite anchoring can be seen in literature.

4 . b . Hydrophobic interactions

As explained earlier, covalent bonding is certainly the most common choice to bind dyes on semiconductors, but one could use other supramolecular interactions. Indeed, weak forces could also be suited for anchoring goals, as they are already under research, such as in reference [34] by Lei Zhang and Jacqueline M. Cole where they use hydrogen bonding to anchor dyes on surfaces.

Hydrogen bonding or hydrophobic interactions (done by adding long aliphatic chains on the dyes that interact with similar chains on the surface) are typically ranging below 12 kcal per mole which is significantly lower than covalent bonding, ranging between 30 to 260 kcal/mol[35]. The use of such weak forces must still be researched to see whether they are sufficient enough to enable correct dye anchoring and correct electron injection.

Part II

OBJECTIVES AND STRATEGIES

Considering the interest in renewables energies and solar fuels nowadays, the potential of DSPECs for harvesting visible light in order to store energy under valuable chemicals bonds such as dihydrogen and the new long-lived $[Fe(phtmeimb)_2]^+$ complex developed by Wärnmark's team, it has come to our mind to create a project where all these domains unite.

The main goal of this master thesis is thus centred around this Iron(III) complex presented in **Figure 14**. In particular, the focus of this work is to introduce anchoring functions which are needed for the development of new DSPECs designs based on the modified structures. To do so, ligand functionalization on the phenyl part will allow the introduction of new anchoring groups leading to the corresponding complexes. As explained before, two types of interaction between the photosensitizer and the surface could be explored: covalent bonding through a phosphonic acid (**Figure 17.D**) and hydrophobic interactions through long carbonated chains (**Figure 17.B and C**). Those anchoring groups will be introduced via a substitution of a bromine atom on the ligand, or on the complex itself which will also be synthesised during this work (**Figure 17.A**).

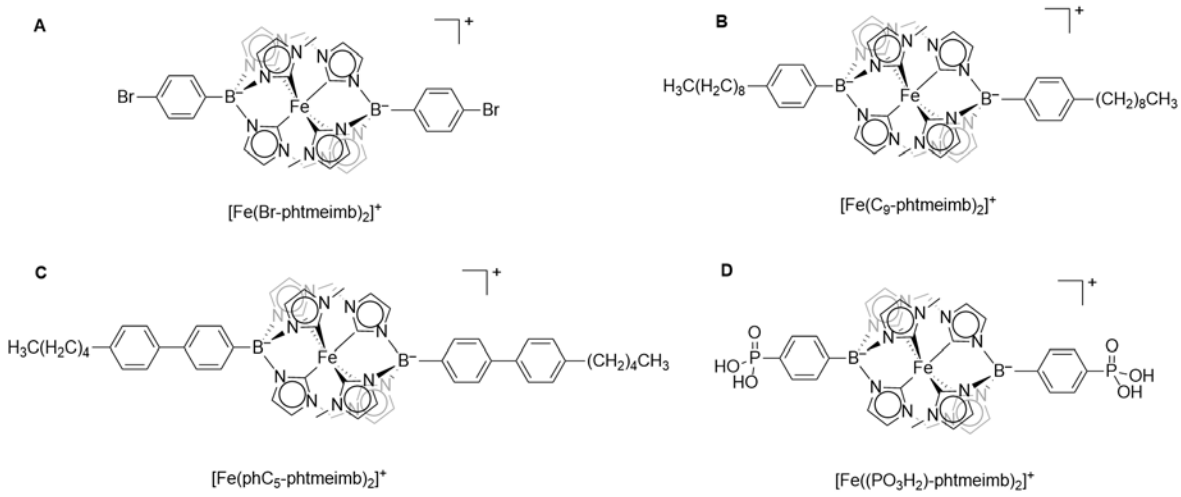

Figure 17: Structure of homoleptic Iron complexes targeted in this master thesis. Structure A is already reported in literature (C_9 = nonyl, phC_5 = phenylpentyl and PO_3H_2 = phosphonic acid) [13]

The overall synthesis strategy for modified Iron complexes $[Fe(Br\text{-}phtmeimb)_2]^+$, $[Fe((PO_3H_2)\text{-}phtmeimb)_2]^+$, $[Fe(C_9\text{-}phtmeimb)_2]^+$ and $[Fe(phC_5\text{-}phtmeimb)_2]^+$ is shown in **Scheme 1**.

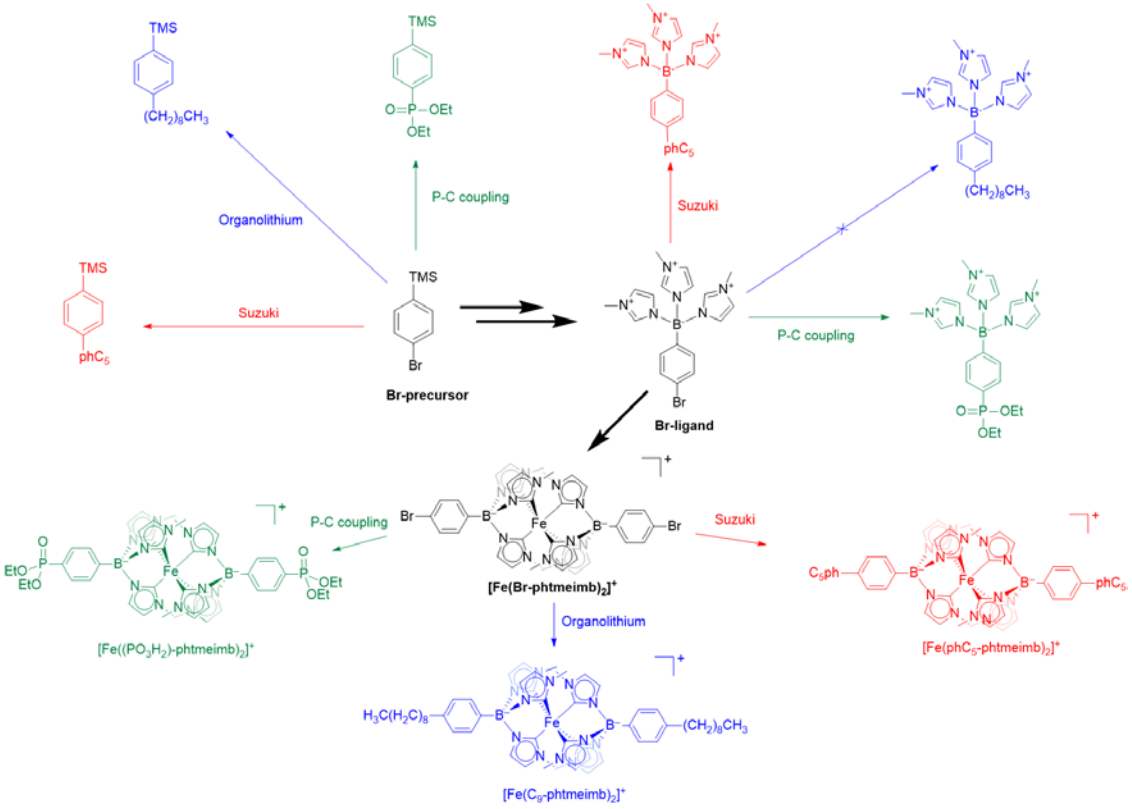

Scheme 1: Synthesis plan for the obtention of the structures aimed in this work.

Different synthetic routes will be explored throughout this work, as the anchoring groups can be introduced starting from the bromine substituted- precursor, ligand or complex.

Synthesis of the different compounds will be achieved according to one of the following procedures:

1) Blue way (Nonyl group addition): An organolithium will be formed starting from the bromine substituted precursor/complex with addition of 1-Bromononane. A SN_2 reaction will occur between them, linking the nonyl chain. Note that this pathway is expected to be unsuited for the modification on the ligand, as it possesses 3 acid protons which would interact with the organolithium.
2) Red way (Phenylpentyl group addition): A Suzuki coupling between (4-pentylphenyl) boronic acid and the bromine substituted precursor, ligand or

complex will be catalysed by [Pd(PPh_3)$_4$] (*tetrakis(triphenylphosphine) palladium(0))*.

3) Green way (Diethylphosphite group addition): A Phosphorus-Carbon (P-C) coupling between diethylphosphite and the bromine substituted precursor/ligand/complex will be catalysed by *[1,1'-Bis(diphenylphosphino) ferrocene]palladium(II) dichloride*.

With the synthetized complexes, the next step would be to anchor them onto a surface and, after proof of concept, build the very first DSPECs based on these iron(III) structures.

Finally, to understand the photophysics of the complexes and see whether modification of the outer coordination sphere would alter the spectroscopical properties of the resulting complexes, a theoretical investigation by DFT and TD-DFT (Time-Dependent Density Functional Theory) calculations will be done. Indeed, the different 3D structures will be optimised by DFT and their associated HOMO-LUMO transitions will be modelled by TD-DFT (both calculations will be done following the computational details on page 52).

Part III

RESULTS AND DISCUSSION

1 Synthesis of $[Fe(phtmeimb)_2]^+$ and $[Fe(Br\text{-}phtmeimb)_2]^+$

Experimentally, $[Fe(phtmeimb)_2]^+$ and $[Fe(Br\text{-}phtmeimb)_2]^+$ are synthesized as followed[32, 36] – **Scheme 2**.

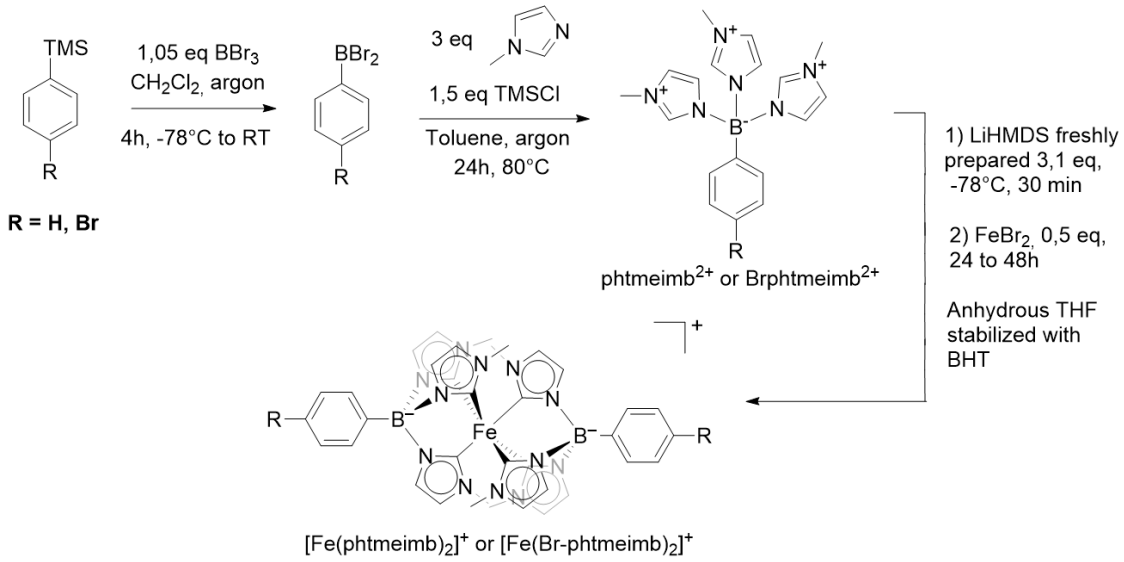

Scheme 2: $[Fe(phtmeimb)_2]^+$ and $[Fe(Br\text{-}phtmeimb)_2]^+$ synthesis route.

First, boron tribromide is added to PhTMS (phenyl-trimethylsilane) to yield the corresponding $PhBBr_2$ structure (dibromo(phenyl)borane). Then, by the addition of TMSCl (trimethylsilyl chloride) and methylimidazole, the $phtmeimb^{2+}$ (or Br-$phtmeimb^{2+}$) ligand is synthesized, precipitated with NH_4PF_6 and purified by washings (water, ethanol then diethylether). Finally, the corresponding complex is synthesized by deprotonating the ligand with freshly prepared LiHMDS and by adding the strongly oxygen sensitive $FeBr_2$ in anhydrous THF for 24h (or 48h for the $[Fe(Br\text{-}phtmeimb)_2]^+$). *Note that the synthesis of the $phtmeimb^{2+}$ ligand in this work was done from a commercial dichlorophenylborane available in the laboratory, which allowed us to skip the first synthesis step to make the $[Fe(phtmeimb)_2]^+$ structure*.

These complexes are easily purified by diethylether reprecipitation or by alumina column chromatography (eluent : CH_3CN 100%). Their characterization has been achieved by ^{1}H-NMR and Mass Spectrometry (MS) (see section V).

2 Synthesis of $[Fe((PO_3H_2)\text{-phtmeimb})_2]^+$

As explained in the introduction, anchoring the Iron complex is essential for the building of solar cells. Therefore, the addition of the diethylphosphite group quickly became a target of choice as the anchoring of such group is already well described in the literature[33].

2. a Diethyl(4-(trimethylsilyl)phenyl)phosphonate synthesis

Synthesis of phosphonic-acid substituted structures is typically done by P-C catalysed coupling with diethylphosphite. The anchoring group is then formed by hydrolysis of the diethylphosphite function under acid conditions (*note that this step should be done when the corresponding complex is formed*). – **Scheme 3**

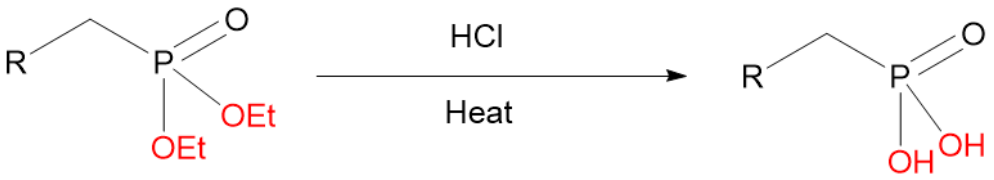

Scheme 3: Hydrolysis of diethylphosphite groups.

Initially, we wanted to achieve the complex synthesis by modifying the BrPhTMS ((4-bromophenyl)trimethylsilane) because of its good solubility and stability properties. The P-C coupling was done under $[Pd(dppf)Cl_2]$ catalysis, also known as [1,1'-Bis(diphenylphosphino)ferrocene]palladium(II) dichloride, following the conditions presented in **Scheme 1.** The desired product was surprisingly easy to clean by simple diethylether/water extraction, which gave a pure product. Once this diethylphosphite modified PhTMS was obtained, the next step seemed to be easily achievable. We tried to synthesise the corresponding ligand following the same path explained in **Scheme 2**. However, this step was found to be unfeasible as no traces of the final product were found after reaction – **Scheme 4**.

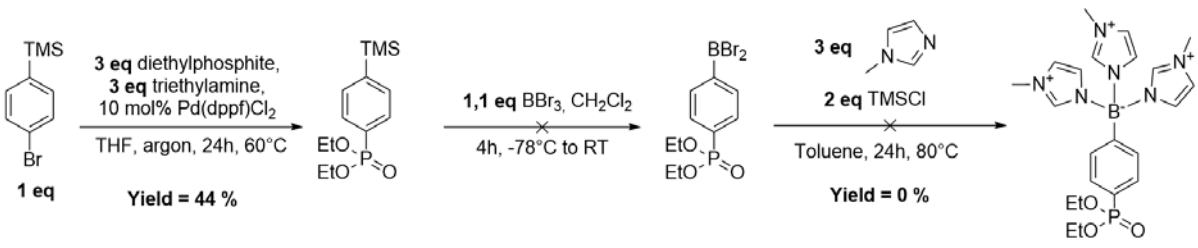

Scheme 4: Attempt for the synthesis of the diethylphosphite-modified ligand.

At the end of the reaction, a precipitate was formed but could not be identified. We suspect a side reaction of the diethylphosphite moiety with boron tribromide that degraded the reagent before being able to pursue the reaction. Thus, if the ligation step is problematic due to a possible diethylphosphite degradation, we decided to first modify the ligand.

2. b Diethylphosphite modification of the ligand

Scheme 5 shows the ligand modification path to achieve the diethylphosphite addition. Three trials of this reaction were done. The first one did not lead to any ^{1}H-NMR signal compatible with the desired product after reaction. The second one did produce the desired compound with 14% yield which was found to be pure by ^{1}H-NMR. However, only a brown oil was yielded, which does not correspond to the overall physical tendencies of these salts (white powders are generally expected, no matter what group modification is present). Therefore, we suspected that this batch still contained impurities not visible in ^{1}H-NMR. The last trial, done with the exact same conditions as the previous two, did not gave any ^{1}H-NMR signal after several washing/precipitations steps (which were not encountered in the previous trials) and did not lead to any final product. We suggest that the 4 charges present on the compound (around the boron atom) might have interfered with the coupling. Moreover, the differences in yields between the three trials could be due to impurities present in the different reagents. However, no significant evidence to confirm or infirm these hypotheses were found through the numerous tests done for this reaction.

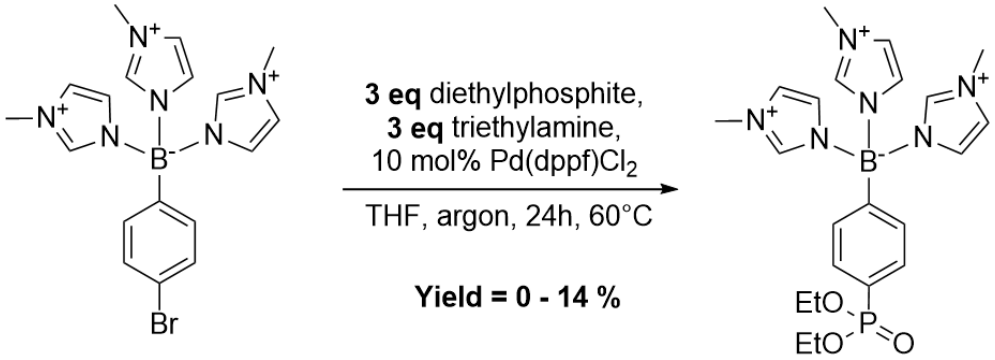

Scheme 5: Synthesis of (PO_3H_2)-phtmeimb^{2+} starting from the bromine substituted ligand.

2. c Diethylphosphite modification of the complex

As the previous reactions did neither give the same results nor yields for each trial, and no quantitative purified product were obtained, we attempted to perform the coupling directly on the bromine complex $[Fe(Br\text{-}phtmeimb)_2]^+$ – **Scheme 6**:

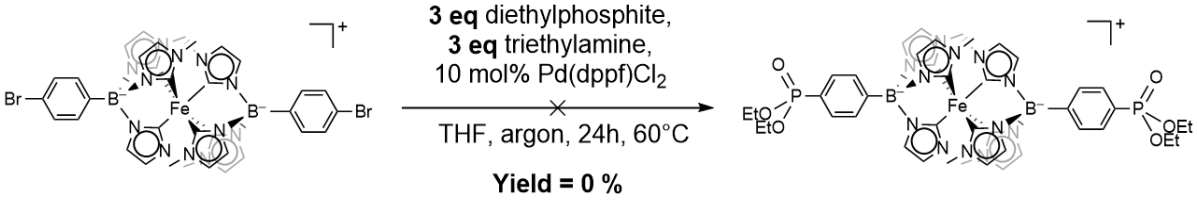

Scheme 6: Attempt for the synthesis of the $[Fe((PO_3H_2)\text{-}phtmeimb)_2]^+$ starting from the bromine substituted complex.

Following the same conditions as for the previous trials, no ^{1}H-NMR signals of the desired product could be observed. Surprisingly, the bromine complex was found intact at the end of the reaction, and did not degrade. In comparison to the previous reactions (**Schemes 5 and 4**), we tend to explain this non-reactivity by a strongly deactivated C-Br bonding, due to the peculiar structure and electron-donating properties of the direct coordination sphere of the Fe^{3+} (namely the borate and NHCs), that prevents the complex from reacting in such mild conditions. To achieve this coupling, temperature and solvent nature could be modified or harder reaction conditions could be tried, such as a microwave usage as reported in ref [37] by György Keglevich et al.

$[Fe((PO_3H_2)\text{-}phtmeimb)_2]^+$ could unfortunately not be synthesized during this work due to a lack of time, but remains a target of choice for anchoring the Iron complex on surfaces. Even so, the diethylphosphite modified PhTMS moiety has proven to be feasible and has shown that the synthesis still needs optimisation. Direct functionalization of the Br-complex also deserves other attempts, as the palladium-catalysed coupling of a phenyl-pentyl moiety on the complex has shown promising results (see section III.4) for this C-Br bond activation.

3 Synthesis of $[Fe(C_9\text{-phtmeimb})_2]^+$

3. a Nonyl modification of the complex

Early works on the bromine substituted complex showed possible organolithium formation by adding *n*-BuLi directly on the complex in an anhydrous solvent (typically THF), as presented by Wärnmark et al. to achieve the COOH- and MeO-functionnalized complex in 2022[38]. To attach long carbon chains, the addition of n-BuLi on aromatic bromines leads to the corresponding organolithium[39]. Then, the addition of the bromine substituted aliphatic chain (here, 1-Bromononane) would yield the modified aromatic ring (via an SN_2 reaction) as shown in **Scheme 7**:

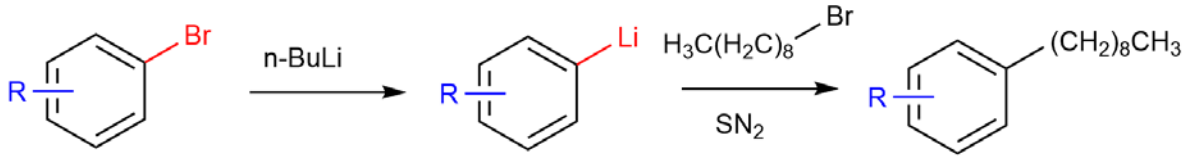

Scheme 7: General synthetic pathway used in this work to attach aliphatic chains.

Therefore, we tried to transpose this synthesis pathway with 1-Bromononane as the electrophile for direct functionalization of the Br-complex (**Scheme 8**).

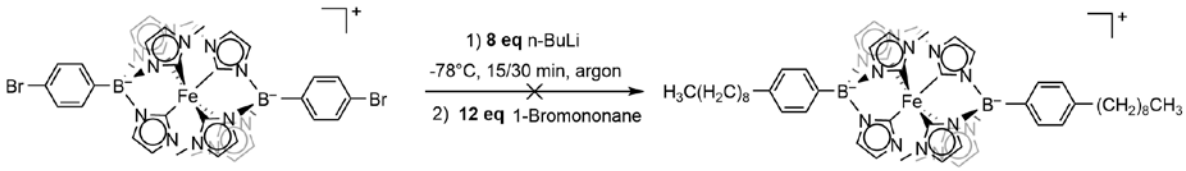

Scheme 8: Attempt of synthesis route towards $[Fe(C_9\text{-phtmeimb})_2]^+$ from $[Fe(Br\text{-phtmeimb})_2]^+$.

Several trials were done on this reaction, with different quantities of reagent, solvent, or even solvent supplier changes but no desired product could be detected. Unfortunately, ^{1}H-NMR always indicated the formation of the $[Fe(phtmeimb)_2]^+$ complex (*i.e.* a substitution of Br by H) with no signals of coupled-aliphatic chains. The first trials were achieved in presence of BHT, which is a protic stabiliser of THF that supposedly reacted via an acid-base reaction with *n*-BuLi. Then, we tried with anhydrous THF without stabiliser, which also gave the same results that still suggests an undesired source of protons inside the reaction medium. Moreover, as the quantities of Br-complex used were always low (average of 2.10^{-5} mol, mass = 20 mg), intrinsic sources of humidity contained in the gas or in the Bromononane could be

enough to react with the de-brominated complex and give the unwanted dehalogenated compound, even with numerous drying stages.

To bypass this issue, we could have used higher quantities of bromine complex to reduce the undesired acid-base side reaction proportion or make this reaction in a glove box, with stronger humidity removal before mixing the reagents. However, due to the lack of time, those trials could not be achieved.

3. b Trimethyl(4-nonylphenyl)silane synthesis

As the previously described Suzuki coupling of the hexyl-boronic acid on the ligand did not work, we tried a different strategy. To avoid any interactions with the acid protons of the ligand, the coupling was attempted on the PhTMS precursor. As reported in reference [39] by Holger Helten et al, the same reaction has been done with 1-bromobutane served as reference compound for our target (**Scheme 9**).

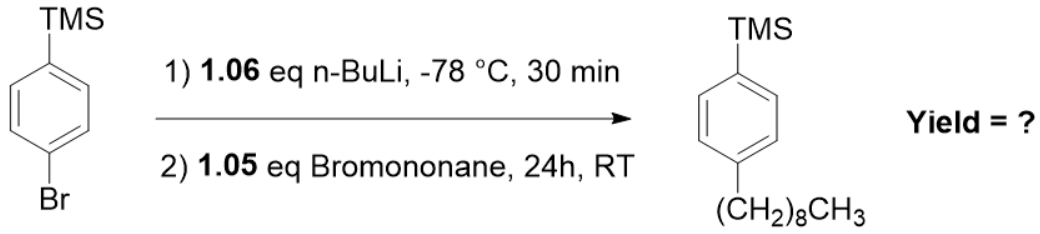

Scheme 9: Synthesis of C_9-PhTMS, using the conditions reported in [39].

The preliminary results for this reaction were encouraging, as the desired product was seen in ^{1}H-NMR and confirmed by COSY ^{1}H-NMR. However, distinct peaks attributed to the Bromononane (uncoupled) could still be observed (**Figure 18.a**), which was surprising considering that with 1.05 eq of Br-nonane introduced in the reaction, only an excess of 0.05 eq should appear assuming total conversion, which seems to be the case here regarding the fact that no Br-PhTMS signal was found at the end or the reaction. However, only by looking at the remaining Bromononane signals, a 0% conversion should be monitored as a near 1:1 Bromononane/product ratio is observed. Also, due to this unwanted quantity of Bromononane in the final batch and because alkane chains tend to form oily products, the yields could not be determined (more details explained hereafter). In the first ^{1}H-NMR spectrum (**Figure 18.a**), the peaks pointed with a red arrow indicate the distinct signals that allowed the

identification of un-reacted Bromononane. In addition, the integration of the protons of the coupled C_9-chain (1.25 to 1.5 ppm region) was too high (only 12 protons should be observed whereas 16.5 are monitored).

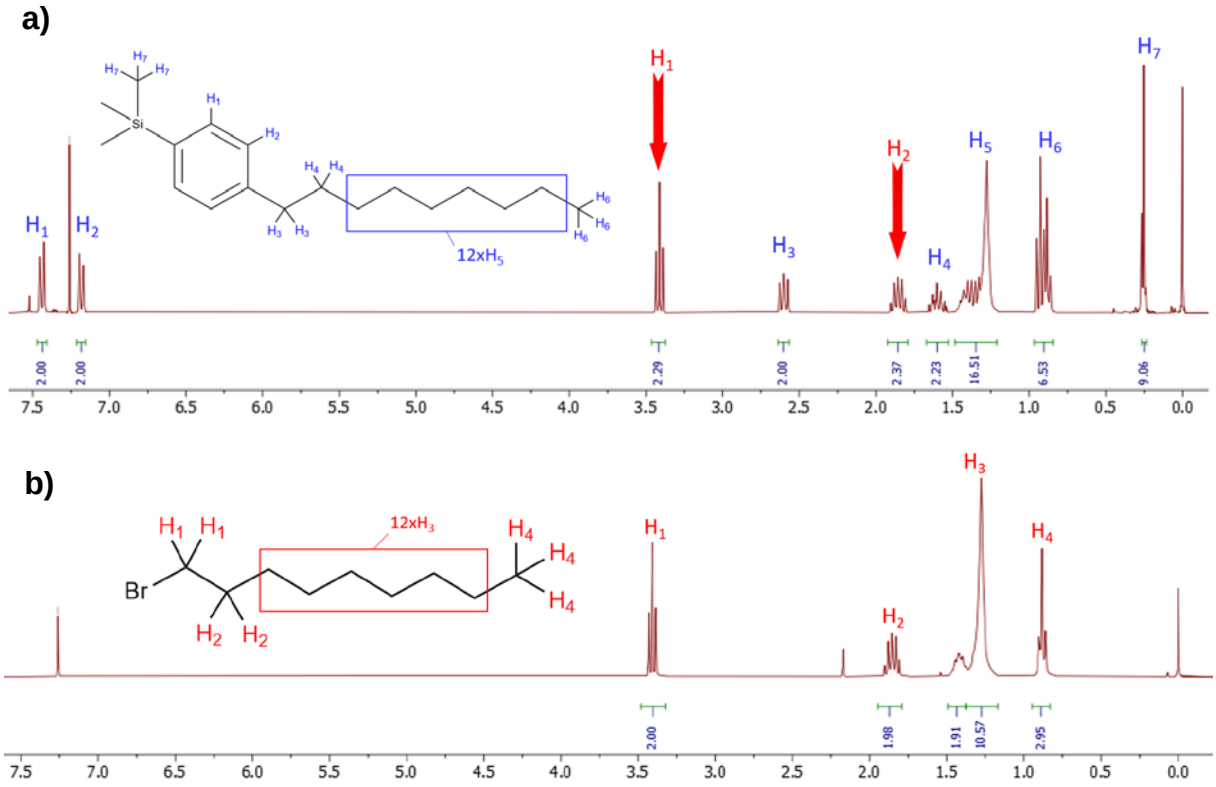

Figure 18: ^{1}H-NMR spectra (0 – 7.5 ppm, $CDCl_3$, 25°C) of a) the nonyl-modified precursor and b) pure Bromononane. The red arrows point the hydrogen peaks of Bromononane (H_1 and H_2, in red).

This could be easily explained as both aliphatic chains (coupled and Bromononane) having very similar ^{1}H-NMR-shifts, only the first two carbons (next to the Br or the phenyl) presents a significative chemical shift difference and allow an unambiguous identification of the desired product (the other signals from the chain overlap). Moreover, as the Bromononane and the C_9-precursor have identical properties (boiling point, polarity, size, solubility), no purification conditions could be found to separate the two products. Several columns were tried but none succeeded to yield the desired pure product. To solve this purification problem, we thought of pursuing the reaction path with the crude product. Because the ligand is a PF_6^- salt, it is insoluble in diethylether, in contrast to the highly soluble Bromononane and should therefore be easily separable from one another in the next synthetic steps.

Unfortunately, the methylimidazole used to build the ligand reacts quickly with Bromononane to afford an imidazolium salt (which is reported in reference [40] by D. Villemin et al, where 1-bromodecane reacts with methylimidazole to form the corresponding salt). This proved that the Br-nonane needs to be removed from the equation before introducing the product in the next step. At this stage, we could still not explain the presence of that much excess of Bromononane at the end of the reaction. Multiple attempts with different conditions were performed and are reported in **Table 1** but every one of them showed the undesired Bromononane peak seen in ^{1}H-NMR.

Entry	Organolithium formation temperature	Organolithium formation duration	Bromononane equivalent
1	RT (controlled by a water bath)	30 minutes	2
2	RT (controlled by a water bath)	30 minutes	1.05
3	0°C	30 minutes	1.05
4	-78°C	1 hour	1.05
5	-78°C	15 min	1.05
6	-78°C	1 hour	0.5

Table 1 : Trials for the 1-Bromononane linkage reaction

Therefore, we then tried to remove the bromine group by quenching it by *n*-BuLi, since the Bromine atom can interfere with the next reaction. Because it is already used in the first reaction, the use of excess *n*-BuLi should not alter the desired product (TMS has a good stability in these conditions), and we imagined the work-up for Bromononane removal by adding excess quantities of *n*-BuLi on the crude product.

The idea is quite simple: *n*-BuLi will react with the Bromononane by an SN_2 reaction or by forming the corresponding organolithium which in turn should be quenched by water. In both cases, only long carbon chains would be formed which should not influence the next steps. This work-up turned out to be successful and it did not interfere with the desired product. The C_9-PhTMS could then be recovered and purified by water/diethylether extraction. As we can see in the ^{1}H-NMR spectra (**Figure 19**), the Bromononane peaks (spotted by the red arrows) are clearly removed after *n*-BuLi treatment. Therefore, this purification methodology was applied for all the different batches, in order to start the ligand synthesis. The yields for this reaction could to date still not be determined, as unknown quantities of aliphatic chains (not distinguishable in ^{1}H-NMR as the peaks overlap) remains present in the reaction medium.

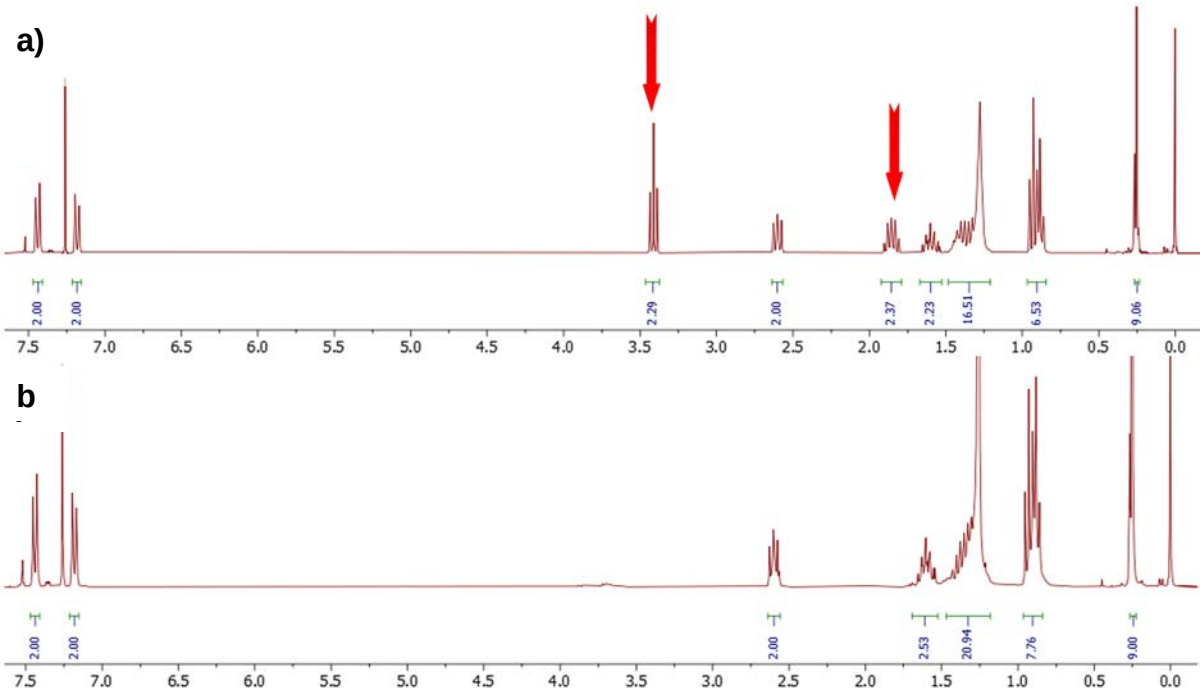

Figure 19: ^{1}H-NMR spectra (0 – 7.5 ppm, $CDCl_3$, 25°C) of the crude product a) before and b) after n-BuLi work up.

3. c Nonyl-modified complex synthesis

After obtaining a purification pathway for the C_9-PhTMS, the corresponding ligand and complex were synthesized using the same reaction conditions as in the original $[Fe(phtmeimb)_2]^+$ synthesis (**Scheme 10**). A pure product was obtained after a column purification (Alumina, eluant = CH_3CN 100%), but with only a 2% yield for the complex was obtained, which leaves room for optimisation.

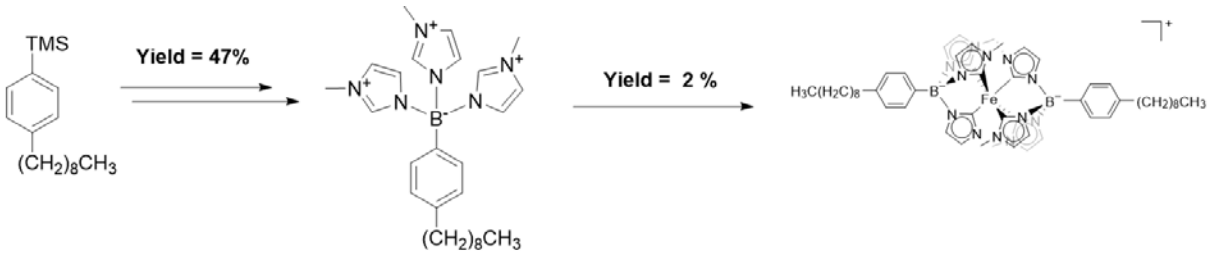

Scheme 10: Simplified synthesis route for the obtention of $[Fe(C_9\text{-}phtmeimb)_2]^+$.

Strikingly, several observations were not in agreement with the full obtention of the expected C_9-complex. The first one was on the ^{1}H-NMR analysis of the ligand (**Figure 20**). Indeed, the integration of the aliphatic chain was found to be less than expected (the 1.25 to 1.5 ppm region integrates for 5.20 protons while they should integrate for

12). Also, the terminal -CH_3 of the same aliphatic chain (H_9 – 0.95 ppm) integrates for less than 3. However, H_7 and H_8 protons are correctly integrated, as well as the different $H_{1\text{-}5}$ protons. Thus, the common skeleton of the ligand (phenyl-tris-imidazolinium borate) seemed correctly synthesized but the aliphatic chain was not long enough.

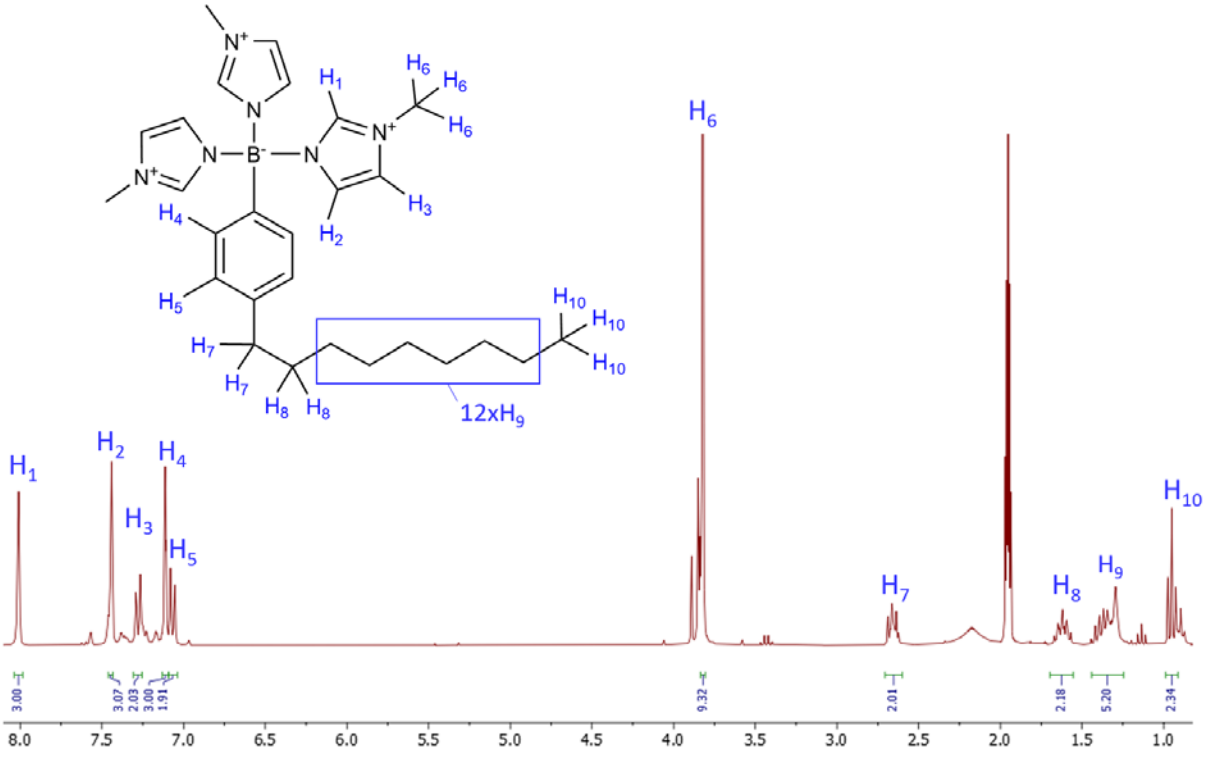

Figure 20: ^{1}H-NMR spectrum (1 – 8 ppm, CD_3CN, 25°C) of the C_9-ligand synthesized from the previous n-BuLi-purified batches.

A mass spectrum (MS) analysis was achieved on the final complex structure batch to try to understand these discrepancies. Surprisingly, three different molecular peaks in the molecular-weight region of the complex could be identified. Indeed, $[Fe(C_9\text{-phtmeimb})_2]^+$ has a molecular weight of 970 m/z which was found in the MS spectrum (**Figure 21.a, A**). However, peaks at 900 and 830 m/z (**Figure 21.a, B and C**) were also found. Moreover, if the three complexes have the same response factor, the 970 m/z and 830 m/z complexes would be respectively the least and most present. Interestingly, the three peaks are linked by removal of one or two “70 m/z” units from the expected 970 m/z complex. After some research, the different peaks could be attributed to two other complexes. Actually, peak B (at 900 m/z) corresponds to a heteroleptic C_9/C_4-complex, with one nonyl chain on one side and a butyl chain on the

other side of the complex (**Figure 21.b, B**). The last peak C at 830 m/z corresponds to the homoleptic C_4-complex (**Figure 21.b, C**). Each removal of a "C_5H_{10}" unit in the aliphatic chains from the C_9- complex directly removes 70 m/z, which concur with the previous results.

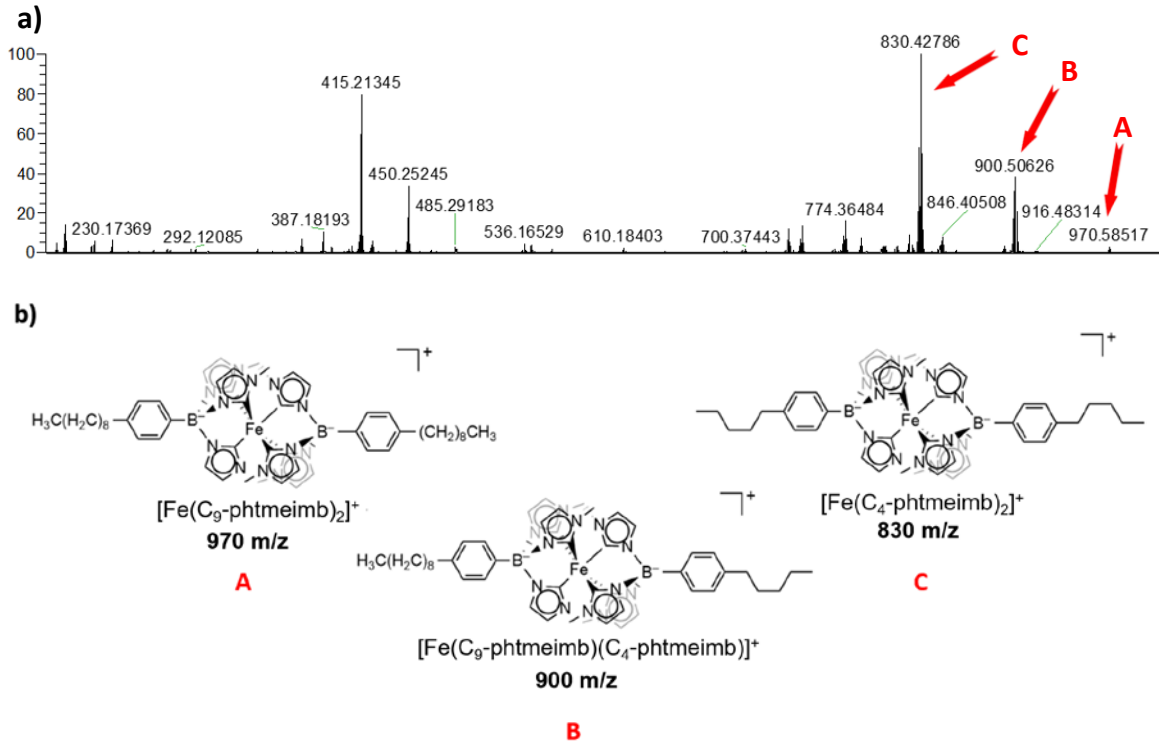

Figure 21: a) MS spectrum of the crude C_9-modified complex. b) Structures of $[Fe(C_9\text{-phtmeimb})_2]^+$ (A), $[Fe(C_9\text{-phtmeimb})(C_4\text{-phtmeimb})]^+$ (B) and $[Fe(C_4\text{-phtmeimb})_2]^+$(C).

These results, even if unexpected, brought the missing piece for understanding the previous odd signals attributions. Indeed, the presence of the butyl chain could only come from the very first step of the reaction which is the elimination of the bromine from BrPhTMS. The use of *n*-BuLi for this step allowed the formation of the organolithium but also of 1-Bromobutane, due to ion exchange between the two partners – **Scheme 11**:

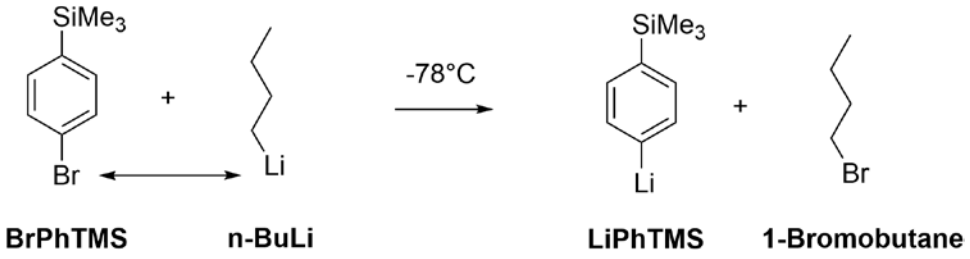

Scheme 11 : Lithium-Bromine exchange reaction at -78°C

The Bromobutane then enters in competition with the Bromononane for the SN_2 upon temperature increase (from -78°C to 25 °C), activating the reactants. This leads to the obtention of two major products (the C_4-PhTMS and C_9-PhTMS) and explains i) the high amount of Bromononane left at the end of the PhTMS derivative synthesis (coming from the necessary excess of bromoalkane, whether it is bromobutane or Bromononane), ii) the inaccurate peak integration observed for aliphatic part of the ligand and complex (C_4 and C_9 chains mixture) and iii) the presence of butyl groups on the complexes. Moreover, the overall SN_2 reaction with *in-situ* formed bromobutane by ion exchange with *n*-BuLi is reported in literature, (see e.g. reference [32]).

Separation of the three complexes seems possible, as a simple alumina column seemed to enrich some fractions with one of the three complexes. In **Figure 22.a**, the heteroleptic C_9/C_4 complex (900 m/z peak) seems enriched, whereas the homoleptic C_4-complex seems enriched in **Figure 22.b** (respectively corresponding to the starting and ending fractions of the column. *Note that this observation could be due to intermolecular interactions leading to different peak intensities without proving a real enrichment*). This result is in correlation with the lower polarity of the complexes when bearing longer carbon chains.

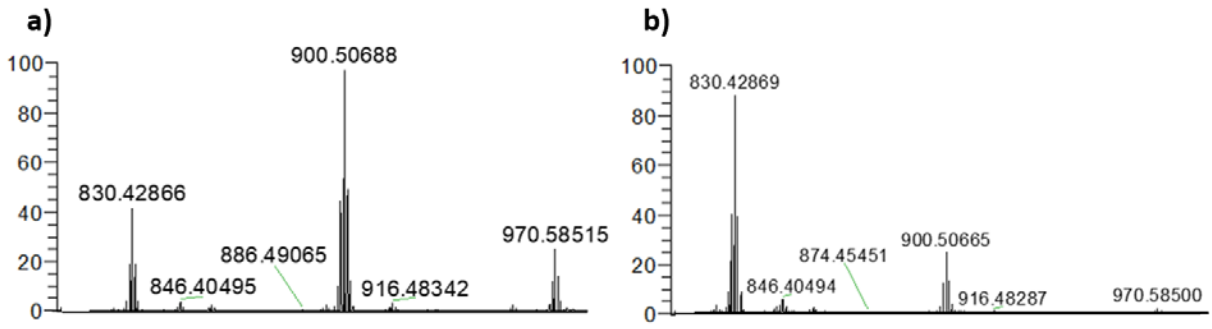

Figure 22: MS analysis of the batch showed in figure 21 a) before and b) after column chromatography.

However, this purification method did not allow to obtain pure compounds. An HPLC analysis could be a good option to increase the separation possibilities, but supplementary research is required to find a better route for a pure C_9-ligand, as the initial *n*-BuLi option would always lead to undesired butyl chains.

A final attempt with a Suzuki coupling was also tried to overcome the chain mixture issue, as it was proven to be robust enough even with the very polarised head of the phtmeimb ligand (see section III.4).

Also, as the hexylboronic acid was available in our laboratory, trials were achieved to investigate this possibility (and thus, forming at the end the $[Fe(C_6\text{-phtmeimb})_2]^+$ complex).

3. d Hexyl modification of the ligand

Two conditions were tested, with K_2CO_3 or K_3PO_4 as the base, and with dioxane or 1:1 dioxane/toluene ratio (**Scheme 12**) as solvent. Unfortunately, no product could be detected from the ^{1}H-NMR analysis for each condition tried. To date, these results remain unexplained and need more investigation to be understood.

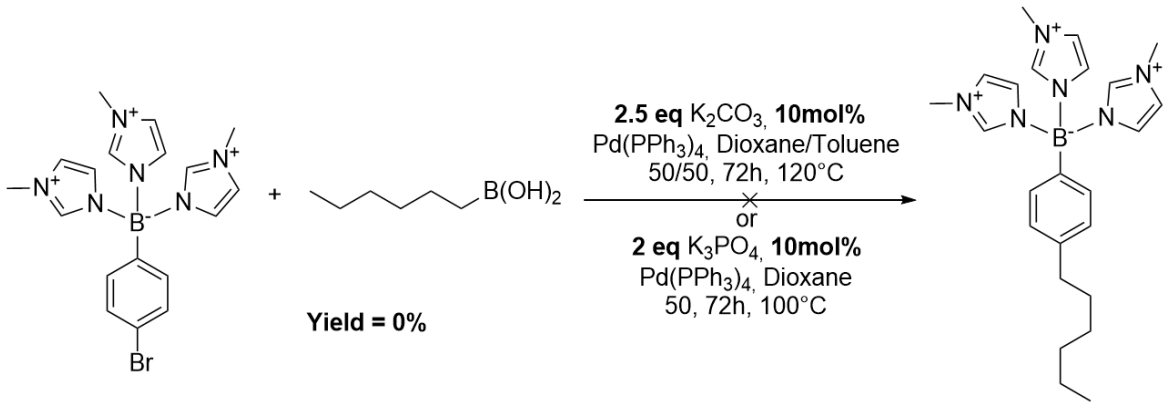

Scheme 12: Proposed synthesis route of the C_6-ligand using Suzuki coupling.

4 Synthesis of $[Fe(phC_5\text{-}phtmeimb)_2]^+$

The synthesis of the $[Fe(phC_5\text{-}phtmeimb)_2]^+$ structure has already been synthesized in the lab via a Suzuki coupling on the Br-complex in the Ph.D. work of Alexia Ripak, but were only observed in traces. Therefore, we tried to apply the acquired knowledge for this work.

The phenyl-pentyl moiety (phC_5) was successfully added to the ligand using the planned Suzuki coupling, as presented in **Scheme 13**. The relatively low yield is likely due to numerous purification steps required for this reaction, to remove the different impurities in the final product. However, due to lack of time, this complex synthesis could not be further investigated in this master thesis.

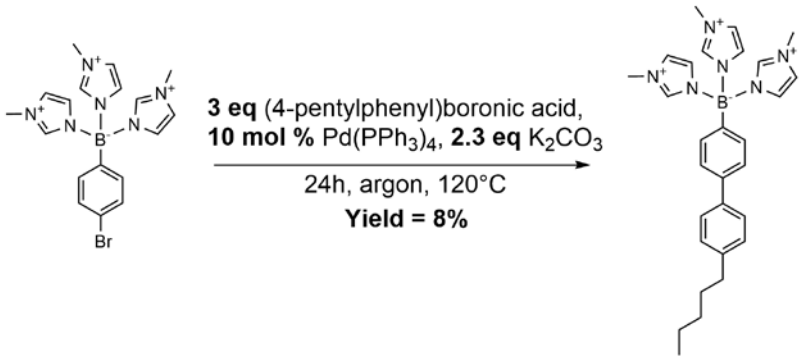

Scheme 13: Synthesis of the phenylpentyl modified ligand starting from the bromine substituted ligand.

5 DFT Studies

As mentioned in section II, a theoretical investigation of this new series of Iron complexes is helpful to better understand their photophysical properties. Therefore, as premises, we have started DFT on several model compounds. The structures of the different complexes were optimized following the computational details described before (page 52) and are reported in **Figure 23**. Each structure easily converged with the B3LYP functional and the different basis sets chosen for the different atoms.

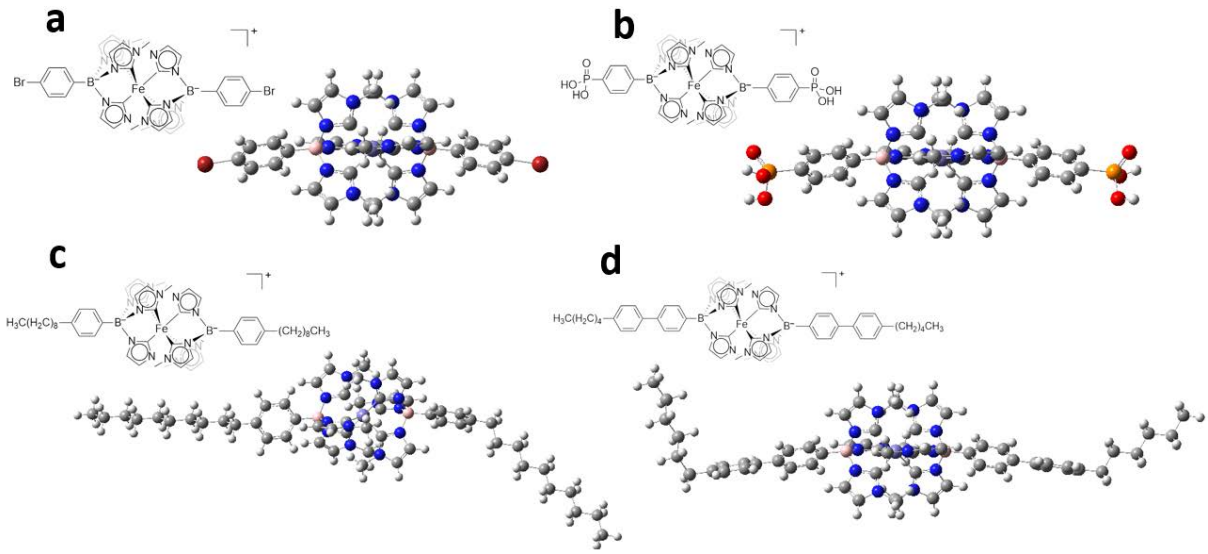

Figure 23: Optimized structures of $[Fe(Br\text{-}phtmeimb)_2]^+$ (a), $[Fe((PO_3H_2)\text{-}phtmeimb)_2]^+$ (b), $[Fe(C_9\text{-}phtmeimb)_2]^+$ (c) and $[Fe(phC_5\text{-}phtmeimb)_2]^+$ (d). The structures were optimized using DFT.

After that, each UV-Visible spectrum of each complex was calculated by TD-DFT. As expected from previous calculations, a strong wavelength gap was observed between the calculated and measured spectra for the maxima of absorption, as seen in **Figure 24**. To improve the DFT accuracy, a benchmark of different UV-Visible spectra calculated with different exchange correlation functionals was done, to see whether any improvement could be achieved. Unfortunately, no functional was able to improve the overall accuracy. Even if the O3LYP and TPSSh ones could improve the accuracy for the 500 nm transition, they still struggle to calculate a correct 200 nm absorption. Thus, we kept the B3LYP functional, as it seemed to have a relatively good accuracy for the visible transition and a good UV accuracy.

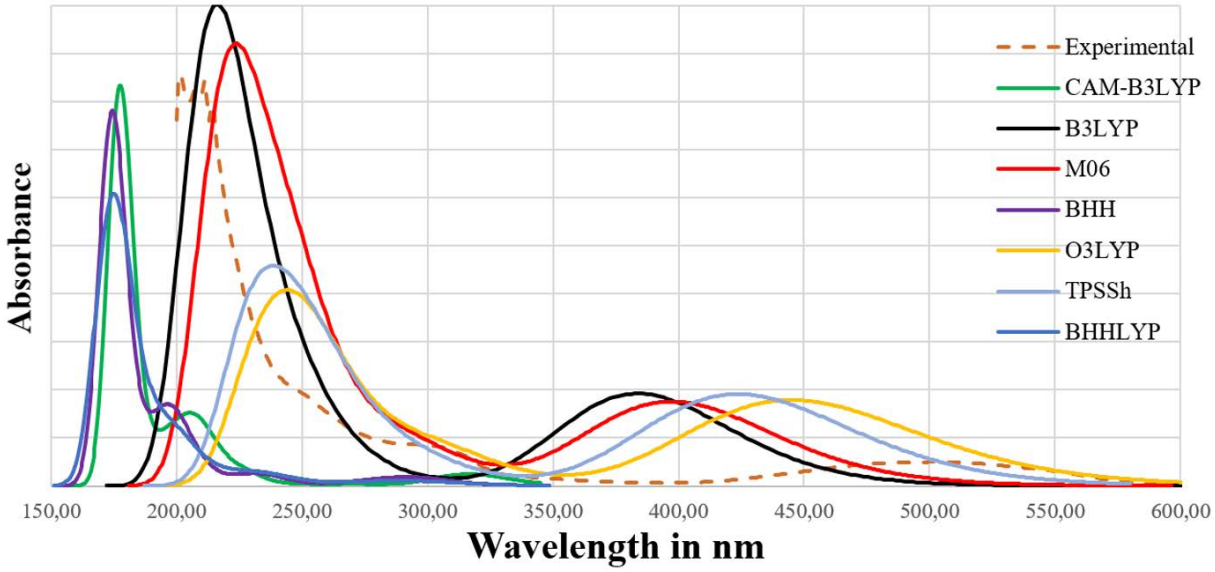

Figure 24: TD-DFT calculations with different functionals for the initial $[Fe(phtmeimb)_2]^+$ complex (full lines) in comparison to the experimental spectrum (brown dotted line). These calculations were done in collaboration with Pr. D. Escudero of KULeuven.

Moreover, this choice was confirmed by the correct LMCT modelling for $[Fe(phtmeimb)_2]^+$ following the computational details on page 52, which can be seen in **Figure 25:**

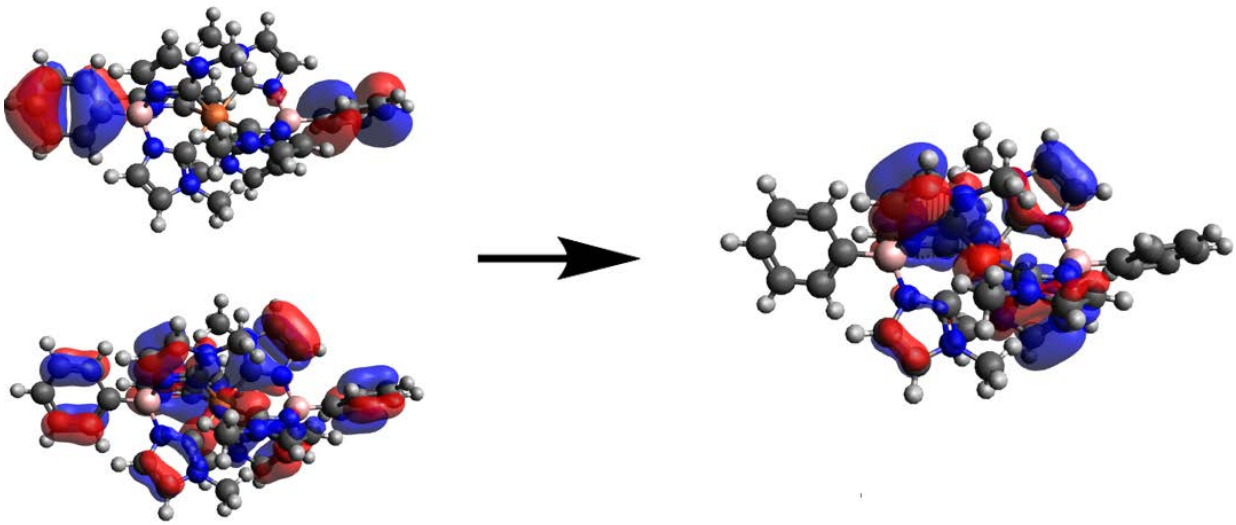

Figure 25: Starting orbital (HOMO – left) and ending orbital (LUMO – right) modelling for the $[Fe(phtmeimb)_2]^+$ complex. Calculations have been done following the previous computational details.

For each complex, their UV-Visible spectra were modelled (see the experimental section, pages 72 – 75) and the associated transitions of the visible part of the spectrum were calculated – **Figure 26** (the movement of the electrons is modelled from the left to the right orbitals). As expected from **Figure 24**, each HOMO/LUMO transition was described to have roughly the same 3.25 eV associated energy, corresponding to an average transition at λ = 380 nm, which is very far from the 2.5 eV measured transition (λ = 502 nm) as explained earlier. However, as the LMCT transition of the $[Fe(phtmeimb)_2]^+$ complex was correctly calculated (**Figure 25**), we trust these transitions to fit relatively well to future experimental data. Moreover, as the TD-DFT did not calculate any energy changes between each visible transition for each complex, we can expect that these groups will have only little influence on the absorption wavelengths. Also, this observation was confirmed for the methoxy- and carboxylic- modified structures that did not show any absorption shifts, as reported in reference [14] by Wärnmark's team.

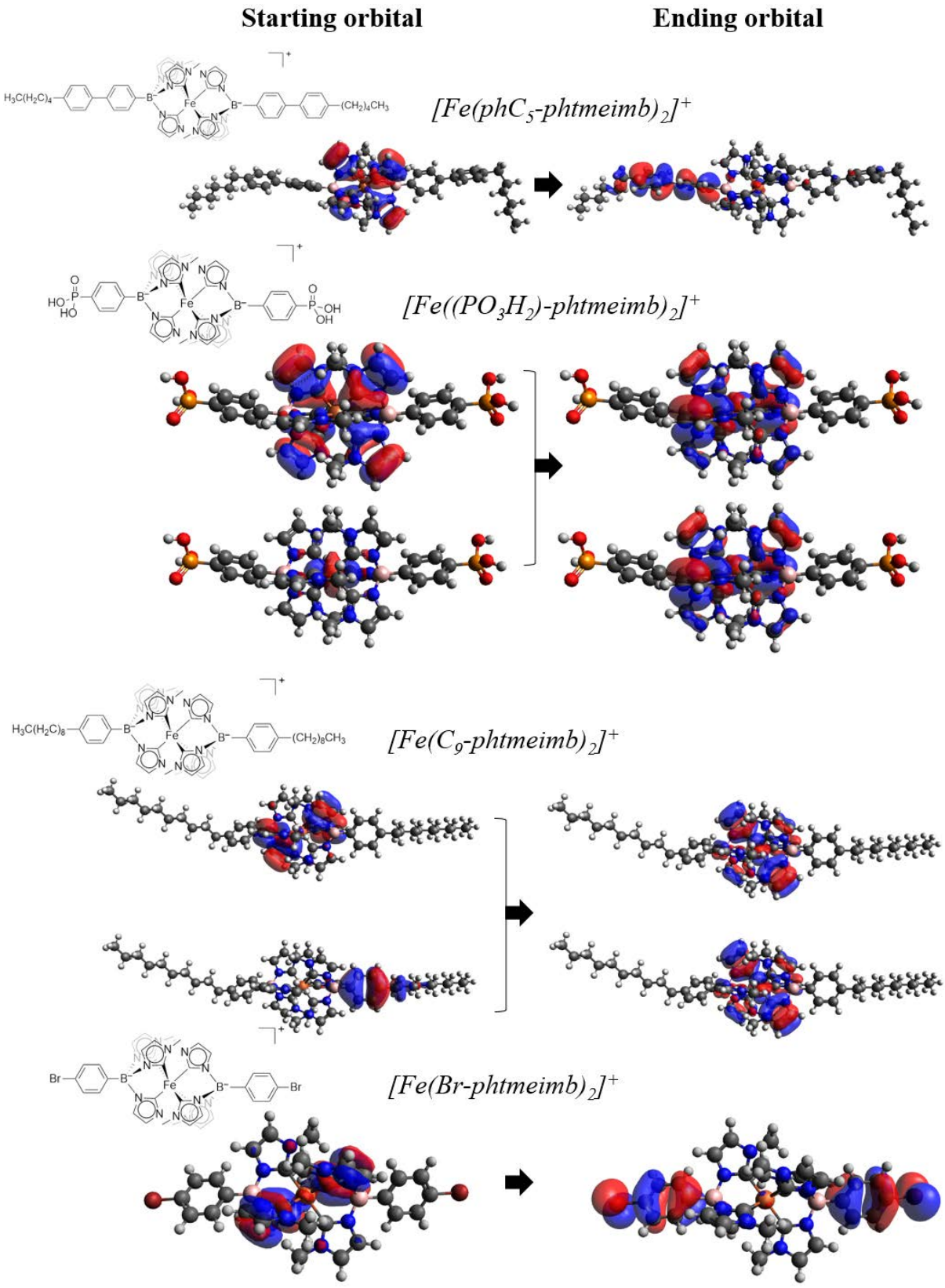

Figure 24: Starting (HOMO) and ending (LUMO) orbitals modelling for the $[Fe(phC_5\text{-}phtmeimb)_2]^+$, $[Fe((PO_3H_2)\text{-}phtmeimb)_2]^+$, $[Fe(C_9\text{-}phtmeimb)_2]^+$ and $[Fe(Br\text{-}phtmeimb)_2]^+$ structures, for the visible transition of the spectrum.

The nature of each transition is reported hereafter – **Table 2**. Note that some are modelled with two different sets of orbitals that contribute to the real transition, as calculated by TD-DFT (each set of orbitals does not contribute equally to the overall transition, which is dictated by the associated orbital coefficient).

Complex	Type of transition	Wavelength (nm)
$[Fe(Br\text{-}phtmeimb)_2]^+$	LLCT	385
$[Fe((PO_3H_2)\text{-}phtmeimb)_2]^+$	LC/LLCT	385 & 381
$[Fe(C_9\text{-}phtmeimb)_2]^+$	LMCT	384 & 381
$[Fe(phC_5\text{-}phtmeimb)_2]^+$	LLCT	384

Table 2: Type of transition for each studied complex as well as the associated wavelengths.

Interestingly, for the structures with electron withdrawing groups (EWG), the electron transition directionality is changed in comparison to the $[Fe(phtmeimb)_2]^+$ structure. Indeed, the directionality is inverted for the $[Fe(Br\text{-}phtmeimb)_2]^+$ structure whereas it is only changed for the $[Fe((PO_3H_2)\text{-}phtmeimb)_2]^+$ complex (for this structure, the benzene rings seem to have no impact on the transition, in comparison to the other structures). A strong competition between the Fe^{3+} attractive centre and electron withdrawing groups is observed, as shown in **Figure 27**:

Figure 25 : LLCT/LMCT competition between the attraction force of Iron and the EWG groups (EWG = Br or PO_3H_2)

Also, the $[Fe(phC_5\text{-}phtmeimb)_2]^+$ structure exhibited a strong shift in the UV transitions, up to the visible parts. Indeed, the different complexes have a calculated UV transition around 220 nm on average, while the $[Fe(phC_5\text{-}phtmeimb)_2]^+$ complex was modelled to undergo 267 nm transitions (which corresponds to a difference of 1 eV). The aromatic ring addition is largely involved in the UV transition and results in a mixture of LC and LLCT transitions – **Figure 28**. Therefore, we could expect a notable shift in the experimental UV-visible spectrum.

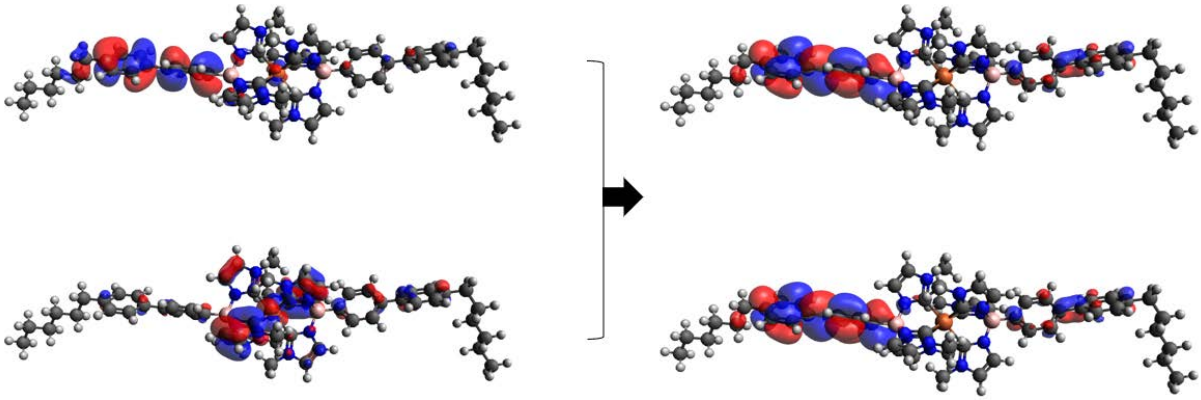

Figure 26: Modelling of the orbitals involved in the 267 nm transition for the [Fe(phC$_5$-phtmeimb)$_2$]$^+$ structure.

Finally, the addition of aliphatic chains did not alter the nature of transitions in comparison to the [Fe(phtmeimb)$_2$]$^+$ structure. Indeed, LMCT transitions were found for the [Fe(C$_9$-phtmeimb)$_2$]$^+$ structure with the same associated energies than the hydrogenated reference complex .

In conclusion, the different groups should have only little influence on the absorption wavelengths as no differences in the energy of the transitions were calculated. However, the electronic transition directionality is expected to change for the [Fe(Br-phtmeimb)$_2$]$^+$ and [Fe((PO$_3$H$_2$)-phtmeimb)$_2$]$^+$ structures. Also, the addition of a benzene ring was shown to stabilise UV transitions, up to the visible parts of the spectrum. Finally, no differences between the [Fe(phtmeimb)$_2$]$^+$ and [Fe(C$_9$-phtmeimb)$_2$]$^+$ structures were calculated, thus highlighting the absence of photophysical changes induced by aliphatic chains addition. Obviously, all of these theoretical data still need to be fully compared to experimental spectra in order to verify these hypotheses.

Part IV

CONCLUSION AND PERSPECTIVES

During this work, we aimed to synthesize four different complexes where three of them could potentially be anchored on surfaces, with the idea of building future experimental DSPECs based on these new structures.

Firstly, the addition of anchoring groups on the complexes have been studied, and some targeted structures were completed, such as the $[Fe(C_9\text{-phtmeimb})_2]^+$ complex However, several issues still need to be solved such as the chain length mixture or the overall low yields for the synthesis. Also, early research on the phenylpentyl-modified ligand shows encouraging results, as a simple Suzuki coupling was able to achieve a pure product with the targeted modification. Moreover, the diethylphosphite coupling on the precursor structure showed good results but needs optimization for further use in solar cells.

Also, the very first evidences of heteroleptic complexes have been found throughout this research, as the $[Fe(C_4\text{-phtmeimb})(C_9\text{-phtmeimb})]^+$ complex was observed in MS. With adequate chromatography purification, this structure could be purified, and characterized.

Finally, despite having wavelength shifts compared to the experimental data, DFT studies gave interesting results for the different structures studied. Indeed, the UV absorption shifts of the $[Fe(phC_5\text{-phtmeimb})_2]^+$, the electron directionality for the $[Fe(Br\text{-phtmeimb})_2]^+$ and $[Fe((PO_3H_2)\text{-phtmeimb})_2]^+$ such as the transition-type for each complex was modelled. Also, the quantum studies showed that no absorption shifts were observed in the visible part of the spectrum with the substitution in the para position of the phenyl ring. Thus, it would still be interesting to compare these results with future experimental data.

With these results, one could want to study the adsorption properties of each structure depending on their anchoring mode. **Figure 29** shows the possible adsorption possibilities for the $[Fe(C_9\text{-phtmeimb})_2]^+$ and $[Fe((PO_3H_2)\text{-phtmeimb})_2]^+$ structures:

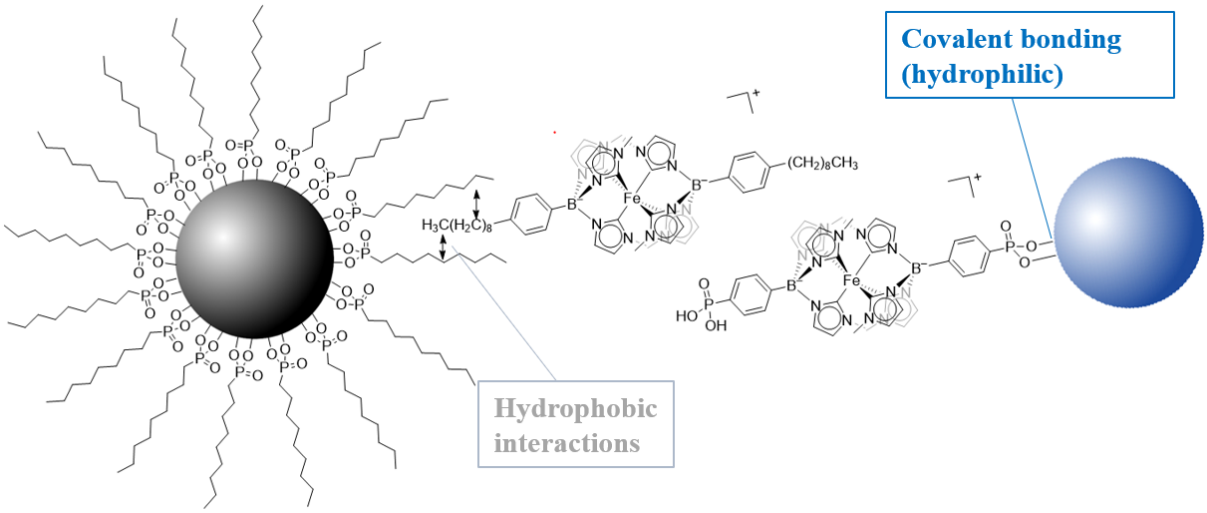

Figure 27: Adsorbed views of $[Fe(C_9\text{-phtmeimb})_2]^+$ and $[Fe((PO_3H_2)\text{-phtmeimb})_2]^+$ on surfaces, represented by the grey and blue spheres.

Finally, the next step would be to build the first Iron-based photoelectrode. Indeed, following the DSPEC design presented before, one could imagine to a photocathode as presented in **Figure 30:**

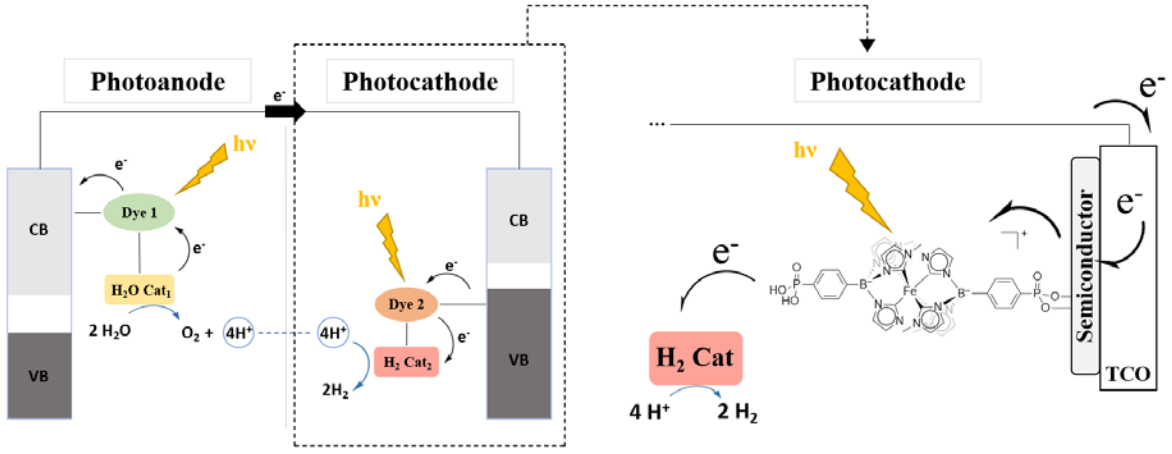

Figure 28 : Example of possible photocathode design based on the $[Fe((PO_3H_2)\text{-phtmeimb})]^+$ structure

Part V

EXPERIMENTAL SECTION

All solvents and reagents for the synthesis are of reagent grade and are used without any further purification. The different precipitates were isolated by filtration. ^{1}H-NMR experiments were performed on a Bruker AC-300 Avance II (300 MHz). The chemical shifts (given in ppm) were measured versus the residual peak of solvent as internal standard (CD_3CN and $CDCl_3$ were the two deuterated solvents used in this work). Mass spectrometry was performed with a direct injection mode, by an sElectrospray ionisator in positive mode. The analyser was an Thermofisher Orbitrap Q-Exactive.

DFT and TD-DFT calculations have been done on the *Gaussian* software. All 3D structures have been modelled by *GaussView* and the orbitals by *Avogadro*.

Moreover, the “gen” Basis set (BS) have been chosen (with 6-31G* for C,H,N,B,P,O atoms, MDF10 for Fe and Def2SVP for Br) because optimisation problems have already been encountered in previous trials, especially concerning the Iron and bromine atoms. This previous mix of BS have stood out as a rather accurate one, but no benchmark was done to find the optimal one. The exchange correlation functional was B3LYP as it was already proven to be suited for these calculations in a previous internship and the solvent model was the PCM (for Polarizable Continuum Model). Each calculation has been done in acetonitrile as a reference solvent. The different self-consistent fields have been performed using the default procedure of *Gaussian* which is a combination of EDIIS and CDIIS algorithms according to reference with a XQC method (which is an extra step of Quadratic Convergence) in case of the hard convergence cases as encountered throughout previous calculations.

1 Experimental procedures and characterization datas

- **(phtmeimb)$(PF_6)_2$**

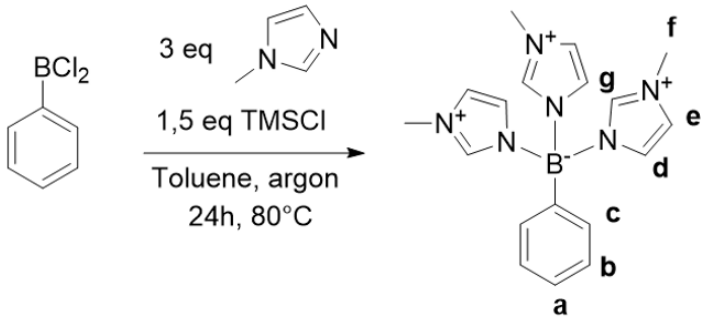

Dichloro(phenyl)borane (0.41 mL, 3.16 mmol, 1 eq) and methylimidazole (0.75 mL, 9.48 mmol, 3 eq) were added to a flame dried 50 mL round-bottom flask with 7.5 mL of toluene and an inert atmosphere was established. After 15 minutes of stirring, a solution of Trimethylsilyl chloride (0.6 mL, 4.74 mmol, 1.5 eq) in 10 mL of toluene was added dropwise. The reaction mixture was stirred at 80°C for 24 hours. After that, the volatiles were removed under reduced pressure and 20 mL of water was added to the medium until dissolution. The brown solution was filtered and a NH_4PF_6 saturated solution was added to the filtrate to precipitate the desired structure, up until no more precipitate was formed. The white precipitate was washed by 3x20 mL of water followed by 3x20 mL of diethylether and dried under vacuum to afford a white powder. Yield: 90% (1.7749 g). ^{1}H NMR (300 MHz, CD_3CN): δ (ppm), 8.05 (s, 3H, g), 7.45 (m, 6H, d, b and a), 7.15 (d, J = 6.37 Hz, 2H, c), 7.1 (s, 3H, e), 3.8 (s, 9H, f)

^{1}H NMR (300 MHz, CD_3CN, 25°C)

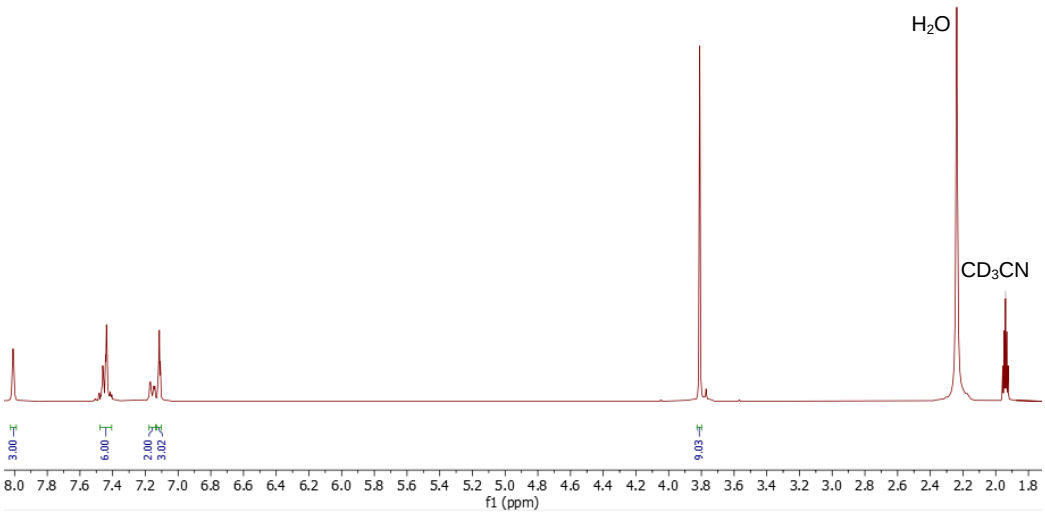

- **[Fe(phtmeimb)$_2$](PF$_6$)**

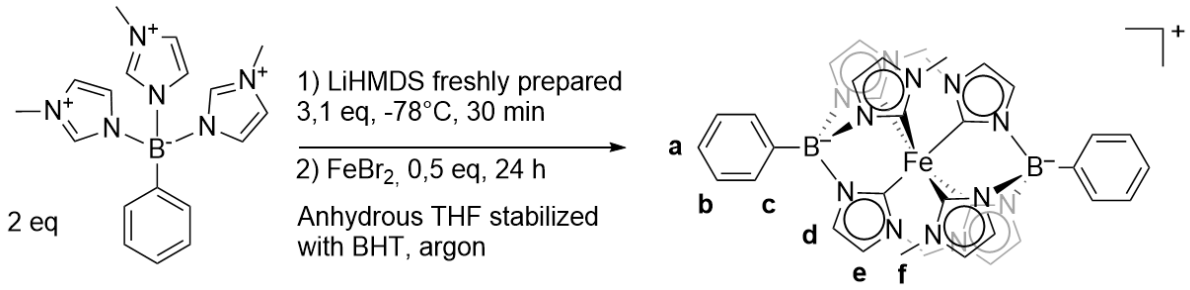

LiHMDS preparation

Hexamethyldisilazane (0.75 mL, 3.5 mmol, 1 eq) was added to a 25 mL flame-dried Schlenk under inert atmosphere. n-BuLi (2.25 mL, 3.6 mmol, 1.6 M in hexanes, 1.03 eq) was added dropwise at 0°C. The reaction was removed from the cooling bath and stirred for 30 min at RT. The alkanes were removed under vacuum, and the resulting white powder was dissolved in 3.5 mL of anhydrous THF stabilised with BHT.

Complexation

Tris(3-methyl-1H-imidazol-3-ium-1-yl)(phenyl)borate(PF$_6$)$_2$ (0.6567 g, 1.05 mmol, 2.1 eq) was added to a 50 mL Schlenk and dried under vacuum for 4 hours, then put under Argon. The ligand was dissolved in 20 mL of anhydrous THF stabilised with BHT and the medium was put at -78°C. The freshly prepared LiHMDS solution was added dropwise to the phtmeimb^{2+} solution, and the medium was stirred for 30 min at -78°C. Anhydrous FeBr$_2$ (0.1007g, 0,5 mmol, 1 eq), previously dissolved in 10 mL of THF, was added at -78°C to yield a black solution. The Schlenk was covered from light exposure and stirred for 24 hours at room temperature. The medium was let under air and a change of colour from black to red was observed. The solution was reduced under vacuum to yield a dark red product. 100 mL of dichloromethane were added to dissolve the solid and the solution was filtered. The filtrate was evaporated under vacuum. The red solid was dissolved in a minimum amount of CH$_3$CN and added dropwise to 150 mL of diethylether to yield a red precipitate, which was filtered and washed with 3x30 mL of diethylether. A column chromatography on neutral alumina was done to purify the product (eluant = acetonitrile), which was then re-precipitated in diethylether and dried. Yield: 33% (0.1417g). ^{1}H NMR (300 MHz, CD$_3$CN): δ (ppm), 14.95 (s, 4H, c), 10.4 (s, 4H, b), 9.8 (s, 2H, a), 4.95 (s, 18H, f), 1.55 (s, 6H, d), -12.5 (s, 6H, e)

^{1}H NMR (300 MHz, CD_3CN, 25°C)

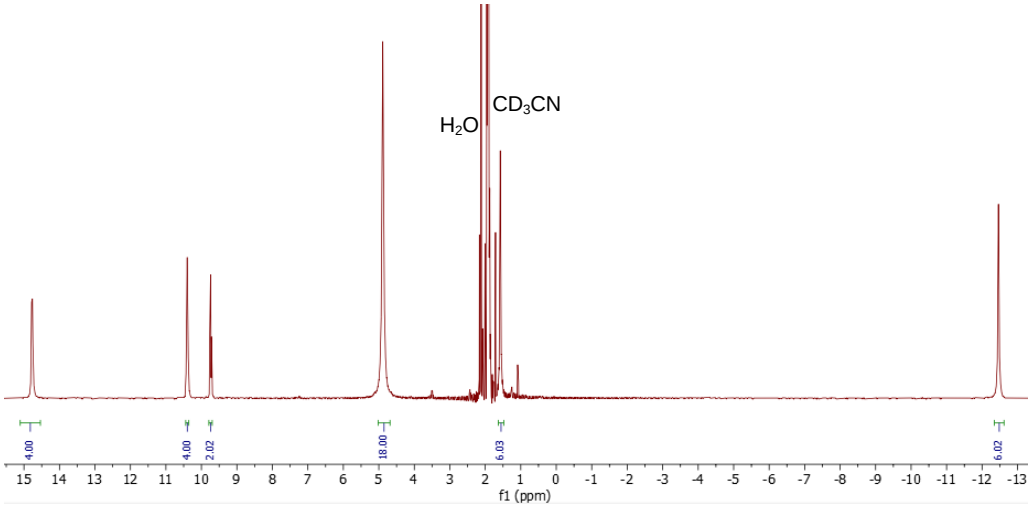

- **(Br-phtmeimb)$(PF_6)_2$**

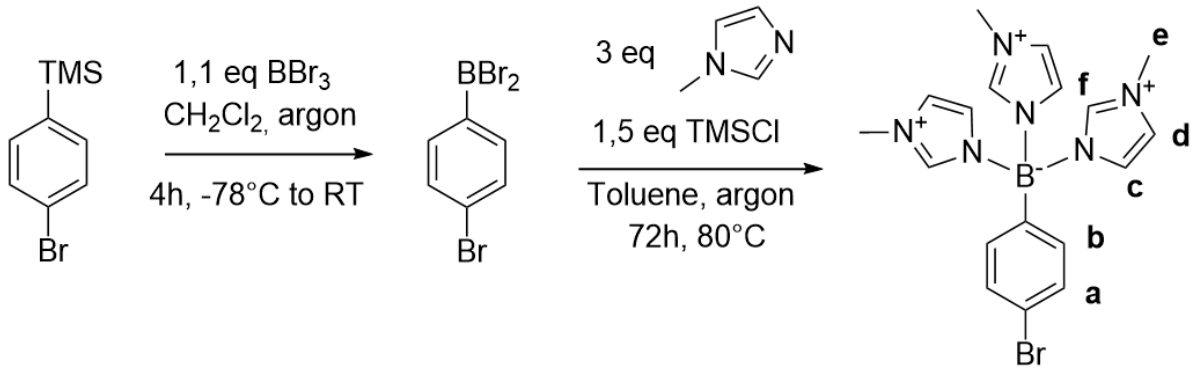

Boron tribromide (3.5 mL, 3.5 mmol, 1 mmol/mL in CH_2Cl_2, 1.1 eq) was added to a flame dried 20 mL round-bottom flask. An inert atmosphere was established and the medium was cooled to -78°C. (4-Bromophenyl)trimethylsilane (0.6 mL, 3.15 mmol 1 eq) was added dropwise and the reaction was stirred for 1 hour at -78°C then 3 hours at room temperature. After that, the solution was dried under vacuum. 7.5 mL of toluene were added to dissolve the brown crude and the inert atmosphere was re-established. Methylimidazole (0.75 mL, 9.48 mmol, 3 eq) was added, and the reaction was stirred for 15 minutes. A solution of Trimethylsilyl chloride (0.6 mL, 4.74 mmol, 1.5 eq) in 10 mL of toluene was added dropwise. The reaction mixture was stirred at 80°C for 72 hours. After that, the volatiles were evaporated under reduced pressure. 20 mL of water were added to the medium and the brown solution was filtered. A NH_4PF_6 saturated solution was added to the filtrate to precipitate the desired structure, up until no more precipitate was formed. The white-beige precipitate was washed by 3x20 mL of water followed by 3x20 mL of diethylether and dried under vacuum to afford a white powder. Yield: 56% (1.2389 g). ^{1}H NMR (300 MHz, CD_3CN): δ (ppm), 8.00 (s, 3H, f), 7.63 (d, J = 8,41 Hz, 2H, a), 7.45 (s, 3H, c), 7.12 (s, 3H, d), 7.09 (d, J = 8.34 Hz, 2H, b), 3.9 (s, 9H, e)

^{1}H NMR (300 MHz, CD_3CN, 25°C)

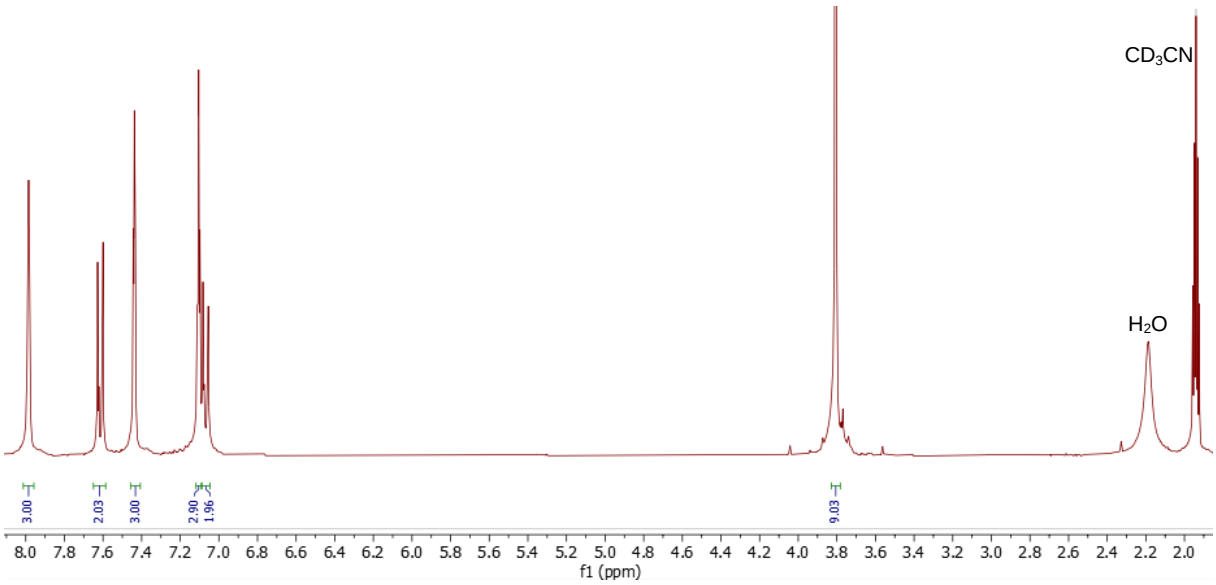

- **[Fe(Br-phtmeimb)$_2$](PF$_6$)**

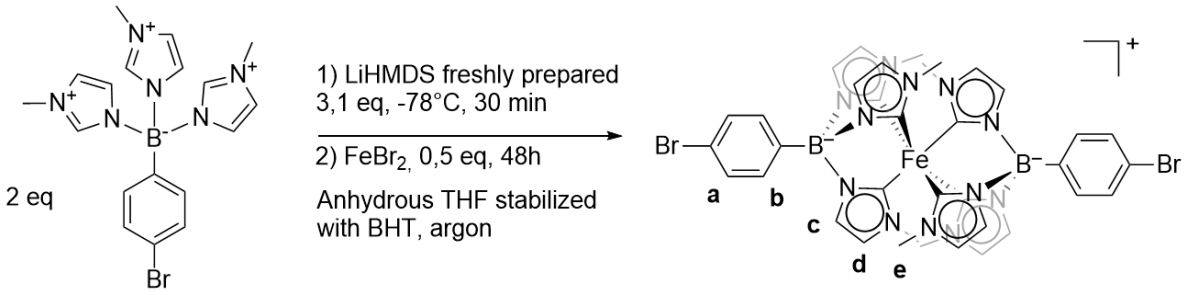

LiHMDS preparation

Hexamethyldisilazane (0.69 mL, 3.22 mmol, 1 eq) was added to a 25 mL flame-dried Schlenk under inert atmosphere. n-BuLi (2.05 mL, 3.28 mmol, 1.6 M in hexanes, 1.02 eq) was added dropwise at 0°C. The reaction was removed from the cooling bath and stirred for 30 min at RT. The alkanes were removed under vacuum, and the resulting white powder was dissolved in 3.2 mL of anhydrous THF stabilised with BHT.

Complexation

(4-bromophenyl)tris(3-methyl-1H-imidazol-3-ium-1-yl)borate(PF$_6$)$_2$ (0.606 g, 0.862 mmol 2 eq) was added to a 50 mL Schlenk and dried under vacuum for 4 hours, then put under Argon. The ligand was dissolved in 18 mL of anhydrous THF stabilised with BHT and the medium was put at -78°C. The freshly prepared LiHMDS solution was added dropwise to the Br-phtmeimb^{2+} solution, and the medium was stirred for 30 min at -78°C. Anhydrous FeBr$_2$ (0.0942 g, 0.431 mmol, 1 eq), previously dissolved in 8 mL of THF, was added at -78°C to yield a black solution. The Schlenk was covered from light exposure and stirred for 24 hours at room temperature. The medium was let under air and a change of colour from black to red was observed. The solution was reduced under vacuum to yield a red a dark red product. 100 mL of dichloromethane were added to dissolve the solid and the solution was filtered. The filtrate was evaporated under vacuum. The red solid was dissolved in a minimum amount of CH_3CN and added dropwise to 150 mL of diethylether to yield a red precipitate, which was filtered and washed with 2x10 mL of cold methanol and 3x30 mL of diethylether. Finally, the red powder was dried under vacuum. Yield: 29% (0.1174 g). ^{1}H NMR (300 MHz, CD_3CN): δ (ppm), 14.8 (s, 4H, b), 10.6 (s, 4H, a), 5 (s, 18H, e), 1.4 (s, 6H, c), -12.3 (s, 6H, d)

^{1}H NMR (300 MHz, CD_3CN, 25°C)

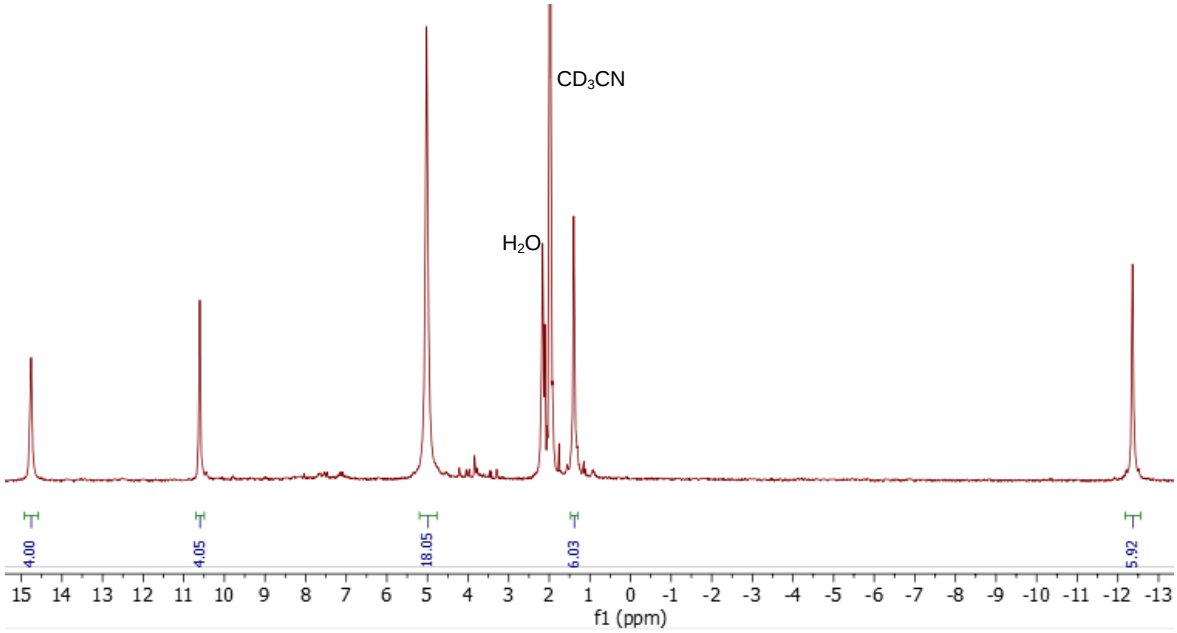

- **(PO_3H_2)PhTMS**

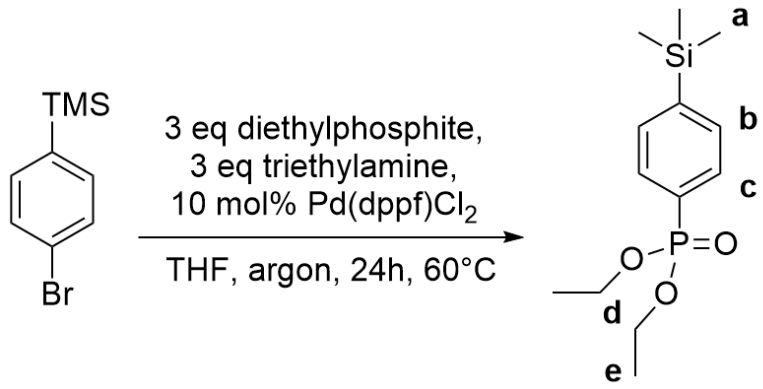

(4-Bromophenyl)trimethylsilane (200 mg, 0.88 mmol, 1 eq), diethylphosphite (363.15 mg, 0.338 mL, 2.63 mmol, 3 eq), triethylamine (266.12 mg, 0.366 mL, 2.63 mmol, 3 eq) and 15 mL of anhydrous THF stabilized with BHT were added to a sealed tube. The solution was stirred and deoxygenated with argon bubbling for 30 minutes. After that, (1,1'-Bis(diphenylphosphino)ferrocene)palladium(II) dichloride (72.3 mg, 0.0988 mmol, 10 mol%) was added to the medium, which has been sealed after 15 more minutes of bubbling and stirring. The solution was left to stir at 60°C for 24 hours. After that, the medium was filtered in a 3 cm silica pad to yield a clear orange solution which was dried under vacuum to yield an orange oil. 30 mL of diethylether and 30 mL of water were added and the phases separated. A yellow precipitate instantaneously formed in the separating funnel, which was filtered. The organic layer was then extracted with 3x30 mL of water, dried over $MgSO_4$ then dried under vacuum to yield a colourless oil. Yield: 44% (0.1109 g). ^{1}H NMR (300 MHz, CD_3CN): δ (ppm), 7.75 (dd, J = 13.25 Hz, J = 8.19 Hz, 2H, c), 7.61 (dd, J = 8.20 Hz, J = 4.39 Hz, 2H, b), 4.12 (m, 4H, d), 1.3 (t, J = 7.09 Hz, 6H, e), 0.27 (s, 9H, a)

^{1}H NMR (300 MHz, $CDCl_3$, 25°C)

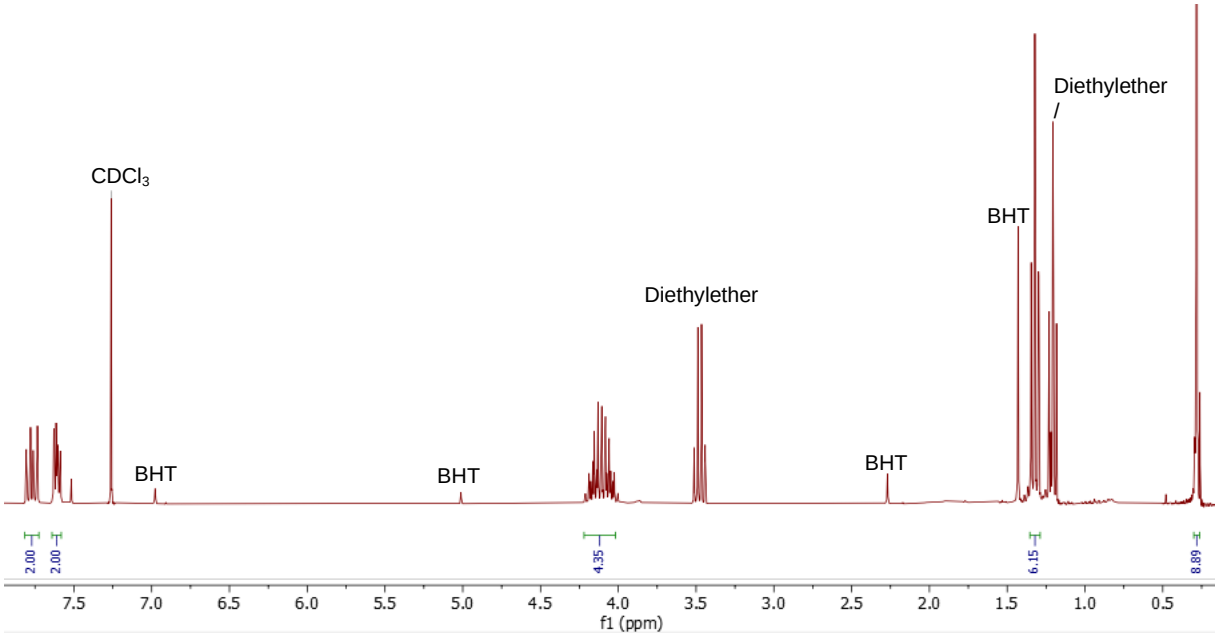

- **(PO_3H_2)-phtmeimb$(PF_6)_2$ from BrPhTMS**

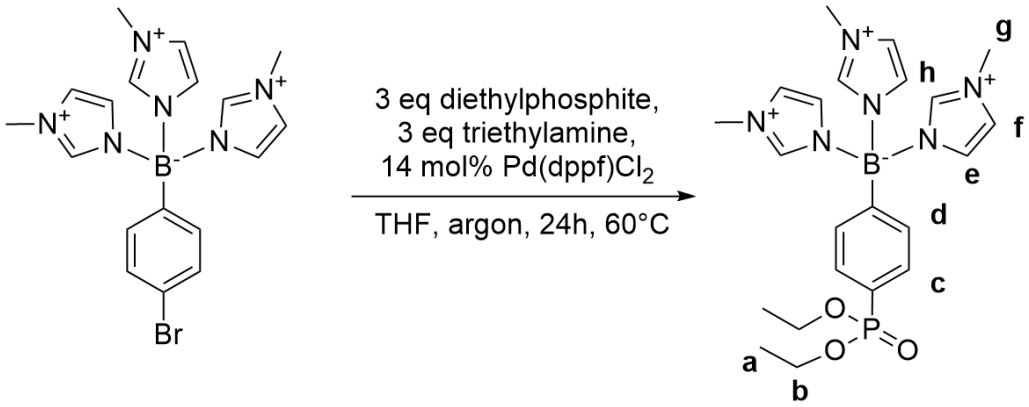

(4-bromophenyl)tris(3-methyl-1H-imidazol-3-ium-1-yl)borate$(PF_6)_2$ (201 mg, 0.285 mmol, 1 eq), diethylphosphite (0.11 mL, 0.852 mmol, 3 eq) and triethylamine (0.12 mL, 0.852 mmol, 3 eq) were added to a sealed tube with 5 mL of THF. After 30 minutes of stirring and argon bubbling, (1,1'-Bis(diphenylphosphino)ferrocene)palladium(II) dichloride (31.7 mg, 0.388 mmol, 14 mol%) was added to the medium, which gave a bright orange suspension. The mixture was stirred 15 more minutes under argon bubbling, before sealing the tube for 24 hours at 60°C. After that, an orange solution was obtained with a yellow precipitate. The precipitate was filtered and washed with 10 mL of THF and 3x10 mL of diethylether. The solid was dissolved in a minimum amount of CH_3CN and put into 50 mL of water, to yield a brown sticky oil, which was dried overnight under vacuum. Yield: 14 % (30.6 mg). ^{1}H NMR (300 MHz, CD_3CN): δ (ppm), 8.1 ppm (s, 3H, h), 7.58 (dd, J = 13.09 Hz, J = 8.38 Hz, 2H, c), 7.45 (s, 3H, e), 7.27 (dd, J = 13.09 Hz, J = 8.38 Hz, 2H, d), 7.25 (s, 3H, f), 4.2 (m, 4H, b), 1.3 (t, J = 7.05 Hz, 6H, a).

^{1}H NMR (300 MHz, CD_3CN, 25°C)

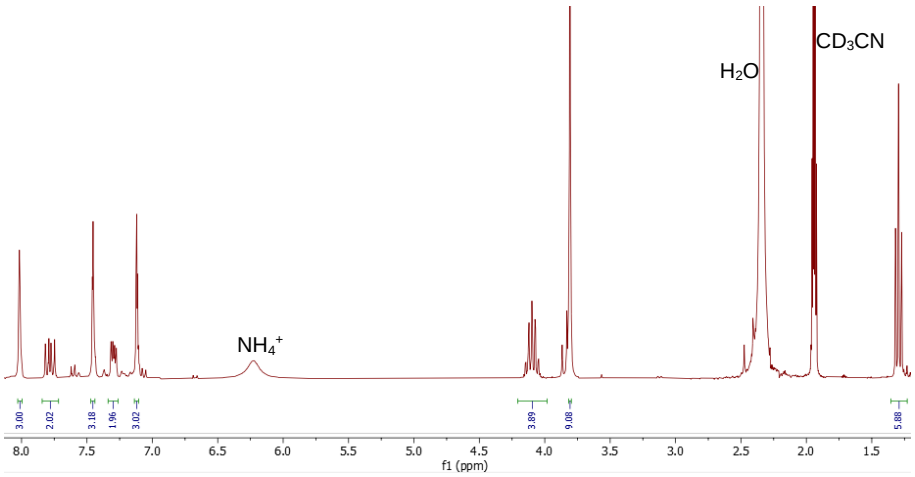

- **C_9PhTMS**

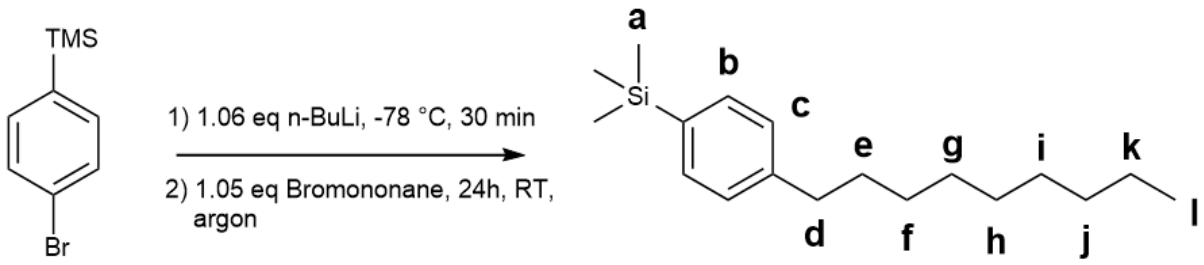

(4-Bromophenyl)trimethylsilane (597.8 mg, 2.62 mmol, 1 eq) was added to a 20 mL flame-dried round-bottom flask with 5 mL of anhydrous THF and an inert atmosphere was established. The solution was cooled down to -78°C before adding *n*-BuLi (1.75 mL, 2.8 mmol, 1.6 mol/L in hexanes, 1.06 eq) dropwise. After 30 minutes, 1-Bromononane (0.53 mL, 2.762 mmol, 1.05 eq) was added and the medium was stirred for 24 hours at room temperature. After that, the solution was dried under vacuum before being extracted with 20 mL of diethylether and 3x30 mL of water. The organic phase was collected, dried with $MgSO_4$ then dried under vacuum to yield a yellow oil. 3 mL of anhydrous THF were added and the solution was cooled down to 0°C. *n*-BuLi (0.9 mL, 1.44 mmol, 1.6 mol/L in hexanes, 0.55 eq) was added and the medium was stirred 3 hours. Water (30 mL) and diethylether (30 mL) were added and the organic phase was extracted with 2x30 mL of water before being dried with $MgSO_4$ and dried by vacuum overnight. *As explained in the part III of this work, the yield could not be calculated and the chain length may be a butyl one*. The COSY NMR was done before the second addition of n-BuLi. ^{1}H NMR (300 MHz, CD_3CN): δ (ppm), 7.45 (d, J = 7.9 Hz, 2H, b), 7.21 (d, J = 7.8 Hz, 2H, c), 2.55 (t, J = 7.9 Hz, 2H, d), 1.65 (m, 2H, e), 1.4-1.2 (m, 12H, f-k), 0.8 (t, J = 7.62 Hz, 3H, l), 0.5 (s, 9H, a)

^{1}H NMR (300 MHz, $CDCl_3$, 25°C)

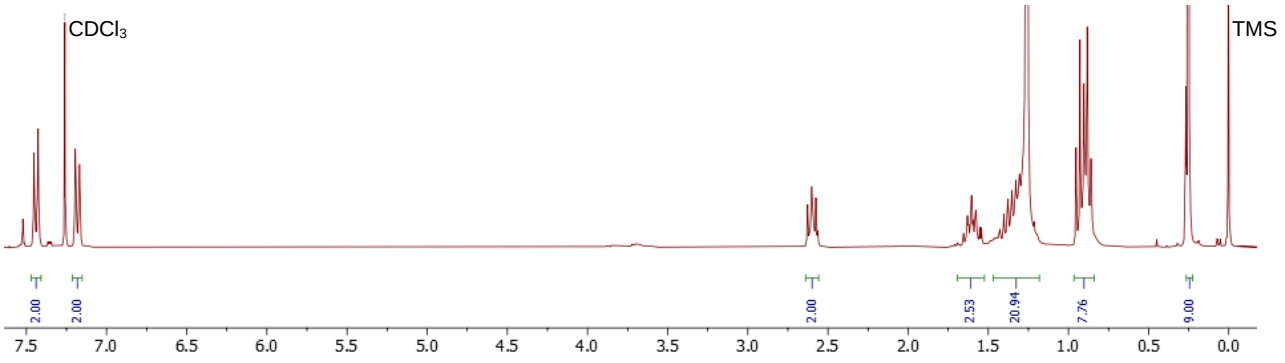

^{1}H COSY NMR (300 MHz, $CDCl_3$)

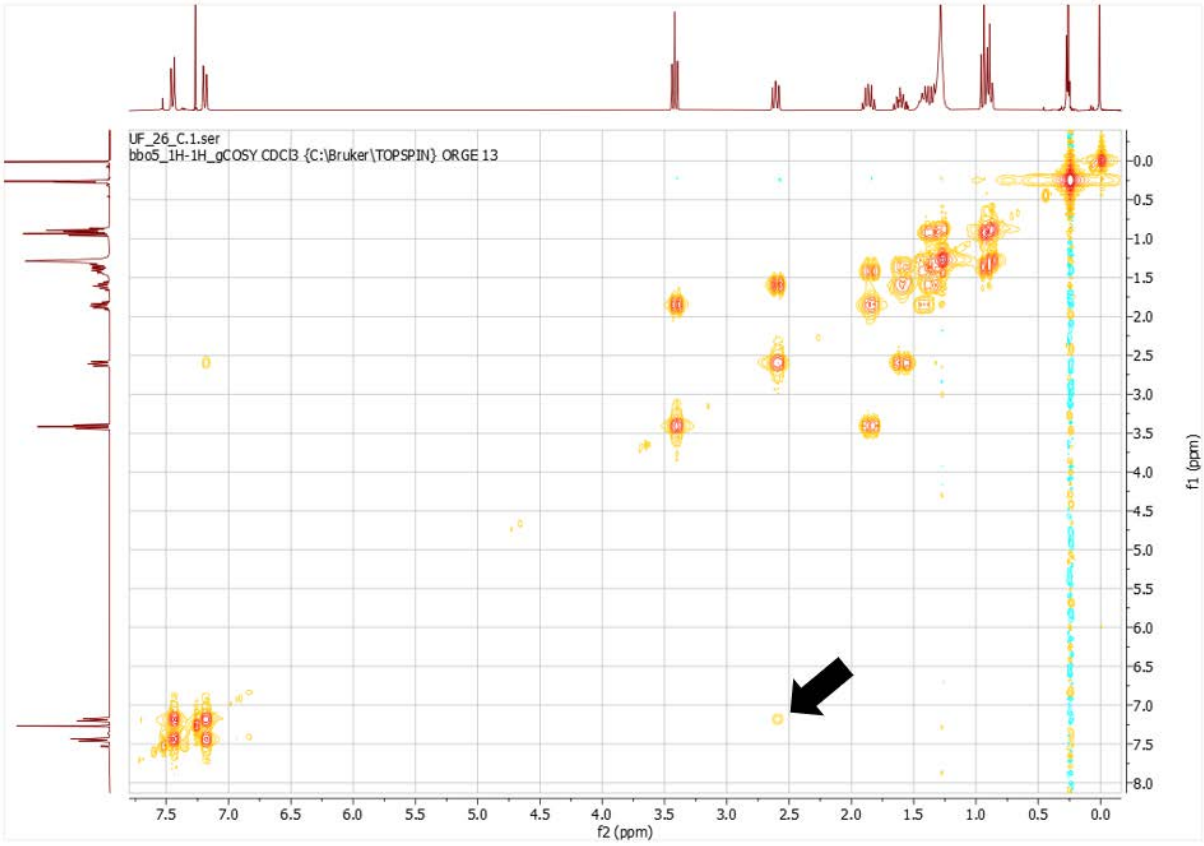

Correlations between peaks b-c (7.45 & 7.21 ppm) and d-e (2.2 & 1.65 ppm) is observed as well as a 4-bond distance connection between peaks c and d was observed (7.21 – 2.2 ppm), thus confirming the aliphatic chain linkage.

- **(C_9-phtmeimb)(PF_6)$_2$ from the modified C_9PhTMS**

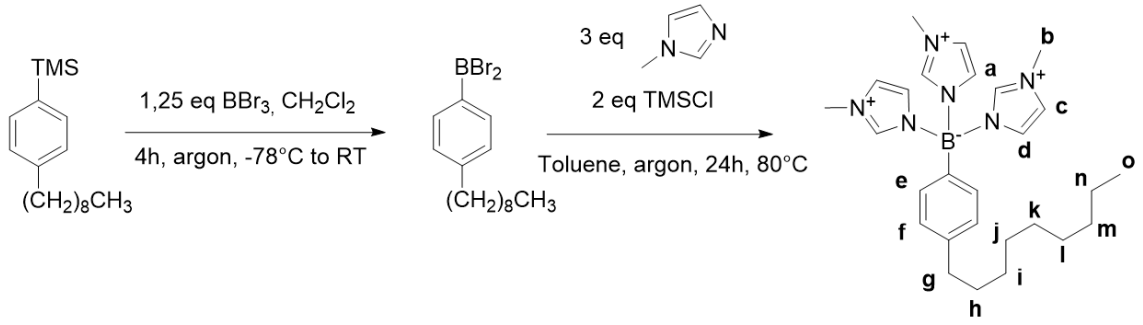

Boron tribromide (3 mL, 3 mmol, 1 mol/L in CH_2Cl_2, 1.25 eq) was added to a 50 mL flame-dried round-bottom flask at -78°C and an inert atmosphere was established. Trimethyl(4-nonylphenyl)silane (0.6548 g, 2.368 mmol, 1 eq) was added and the reaction was stirred 1 hour at -78°C then 3 hours at room temperature. The volatiles were evaporated under vacuum and the crude was resolubilized in 10 mL of toluene. Methylimidazole (0.71 mL, 8.679 mmol, 3 eq) and trimethylsilyl chloride (0.6 mL, 4.736 mmol in 5 mL of toluene,) were added and the inert atmosphere was re-established. The mixture was stirred 24h at 80°C. After evaporation of the reaction solvent, 30 mL of water was added and the solution was filtered. A saturated solution of NH_4PF_6 was added on the filtrate to yield a brown oil, until no more was formed upon addition. The product was solubilized in a minimum amount of CH_3CN and precipitated in 100 mL of diethyl ether, to yield a beige precipitate collected by filtration. The beige powder was stirred in 100 mL of n-hexane overnight before being dried under vacuum. Yield = 47 % (0.842 g). ^{1}H NMR (300 MHz, CD_3CN): δ (ppm), 8.1 (s, 3H, a), 7.45 (s, 3H, d), 7.28 (d, J = 7.77 Hz, 2H, e), 7.25 (s, 3H, c), 7.2 (d, J = 7.98 Hz, 2H, f), 3.7 (s, 9H, b), 2.6 (t, J = 7.65 Hz, 2H, g), 1.6 (m, 2H, h), 1.4-1.25 (m, 12H, i-n), 0.95 (t, J = 7.32 Hz, 3H, o). *Note that the aliphatic chain is probably a butyl one, as explained in the section III of this work.*

^{1}H NMR (300 MHz, CD_3CN, 25°C)

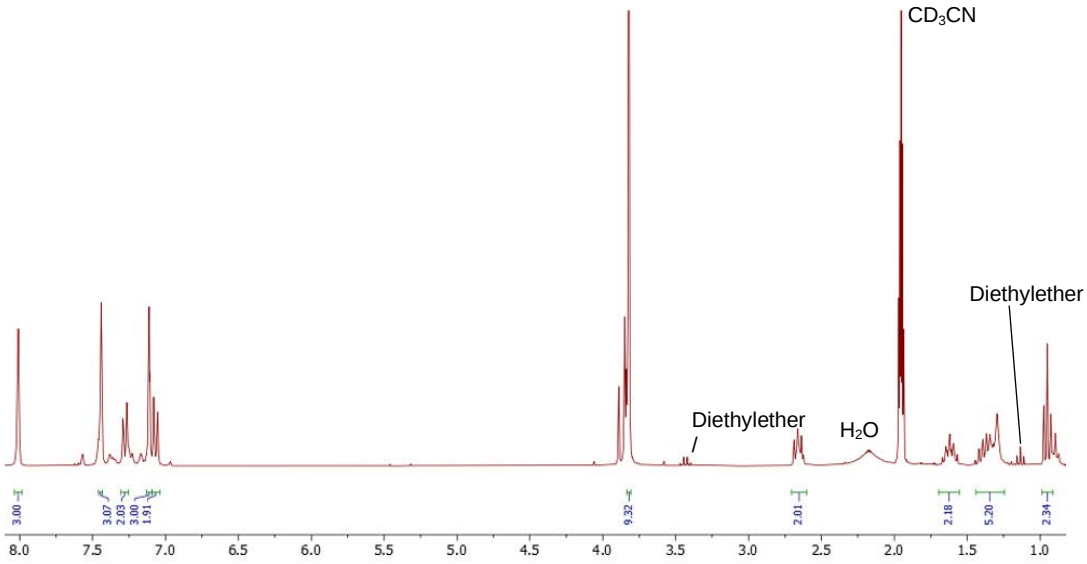

- **[Fe(C_9-phtmeimb)$_2$](PF_6) from the modified C_9phtmeimb(PF_6)$_2$**

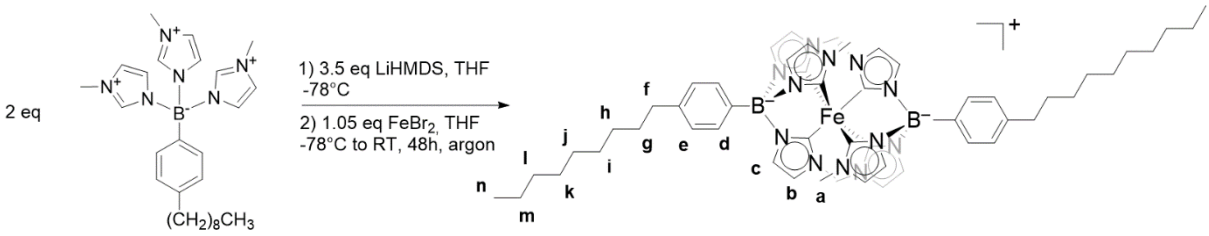

LiHMDS preparation

Hexamethyldisilazane (0.46 mL, 2.146 mmol, 1 eq) was added to a 25 mL flame-dried Schlenk under inert atmosphere. n-BuLi (1.4 mL, 2.24 mmol, 1.6 M in hexanes, 1.04 eq) was added dropwise at 0°C. The reaction was removed from the cooling bath and stirred for 30 min at RT. The alkanes were removed under vacuum, and the resulting white powder was dissolved in 2.15 mL of anhydrous THF stabilised with BHT.

Complexation

tris(3-methyl-1H-imidazol-3-ium-1-yl)(4-nonylphenyl)borate(PF_6)$_2$ (0.4612 g, 0.615 mmol, 2 eq) was added to a 50 mL Schlenk and dried under vacuum for 4 hours, then put under Argon. The ligand was dissolved in 12.5 mL of anhydrous THF stabilised with BHT and the medium was put at -78°C. The freshly prepared LiHMDS solution was added dropwise to the phtmeimb^{2+} solution, and the medium was stirred for 30 min at -78°C. Anhydrous $FeBr_2$ (68.7 mg, 0,321 mmol, 1.05 eq), previously dissolved in 6 mL of THF, was added at -78°C to yield a black solution. The Schlenk was covered from light exposure and stirred for 24 hours at room temperature. The medium was let under air and a change of colour from black to red was observed. The solution was reduced under vacuum to yield a red a dark red product. 100 mL of dichloromethane were added to dissolve the solid and the solution was filtered. The bright red filtrate was dried under vacuum. 5 mL of CH_3CN was added to dissolve the red crust and added to 150 mL of diethylether to yield a red precipitate, which was purified by column chromatography (alumina, 100% CH_3CN). A second column was done one the purified complex to enrich certain fraction with the different structures obtainable (alumina, CH_3CN/Toluene gradient). Yield: 2% (10.6 mg). *Note that the [Fe(C_4phtmeimb)$_2$](PF_6) structure is probably the one obtained here, as explained in the section III of this work*

.

^{1}H NMR (300 MHz, CD_3CN): δ (ppm), 14.7 (s, 4H, d), 10.3 (s, 4H, e), 4.9 (s, 18H, a), 4.38 (t, J = 7.83 Hz, 4H, f), 3.15 (m, 4H g), 2.57 (m, 4H, h), 1.77 (t, J = 7.44 Hz, 6H, n), 1.67 (s, 6H, c), -12.5 (s, 6H, b)

^{1}H NMR (300 MHz, CD_3CN, 25°C)

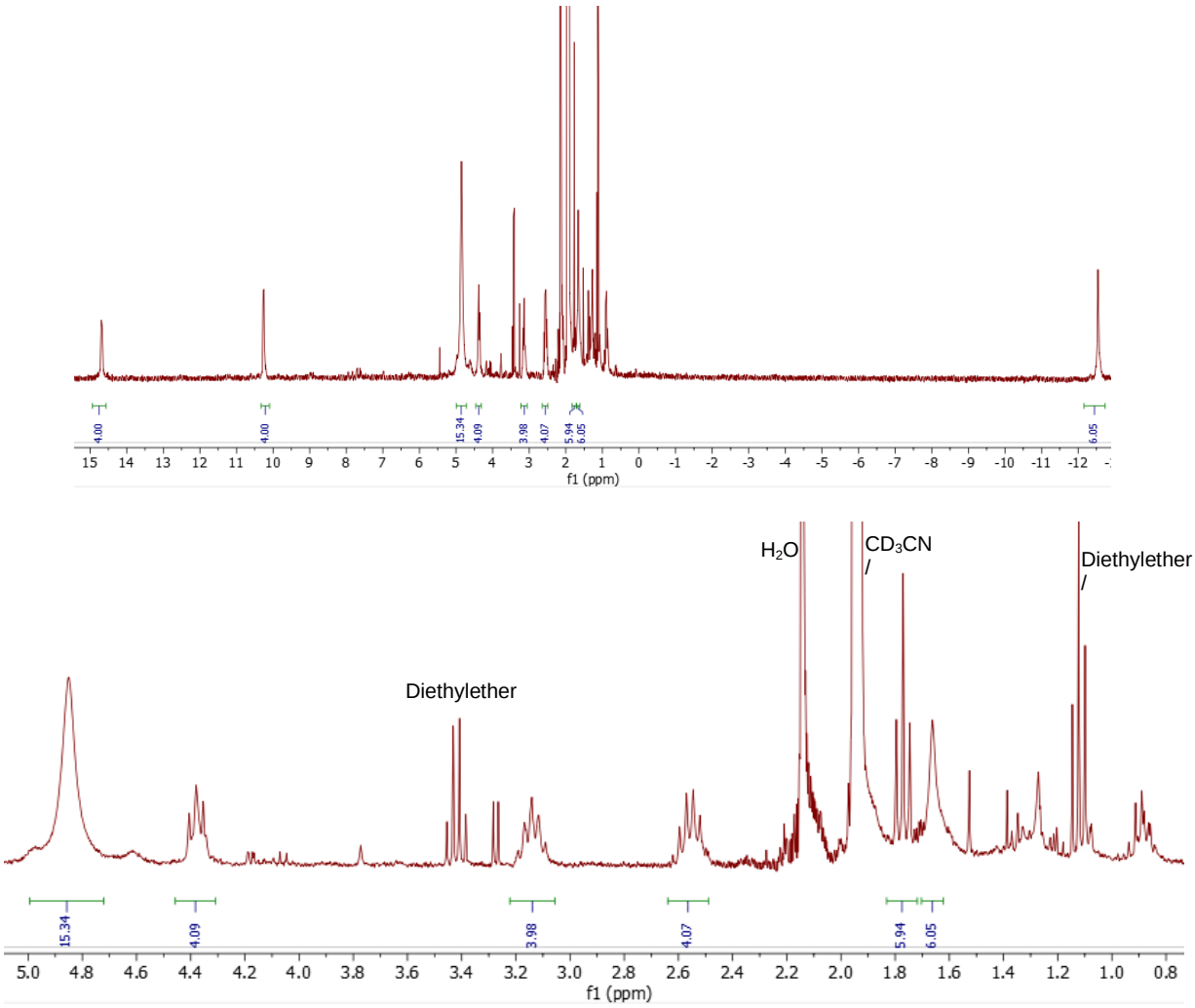

MS Analysis – Before the second column

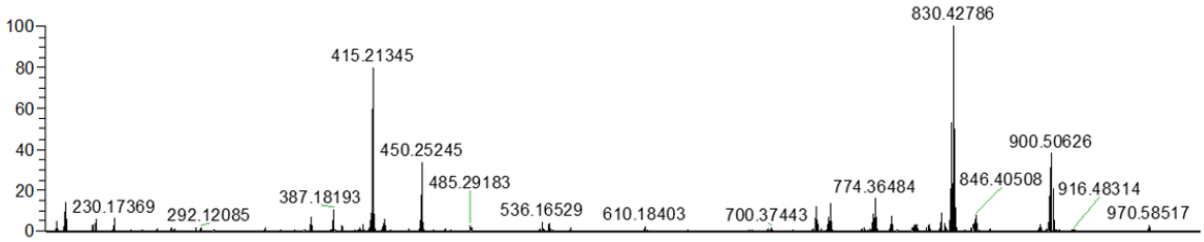

MS Analysis – After the second column (7th fraction)

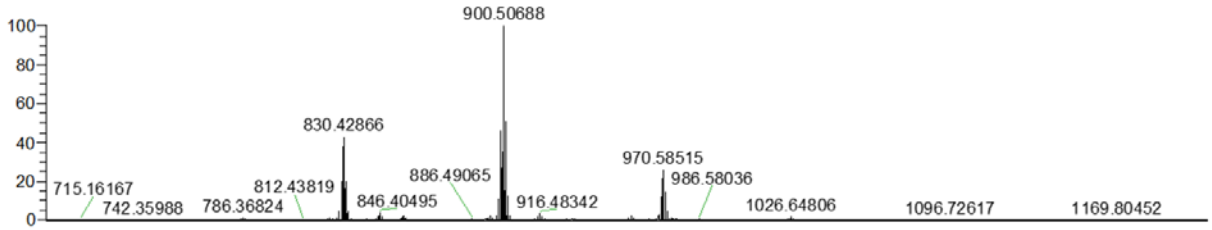

MS Analysis – After the second column (24th fraction)

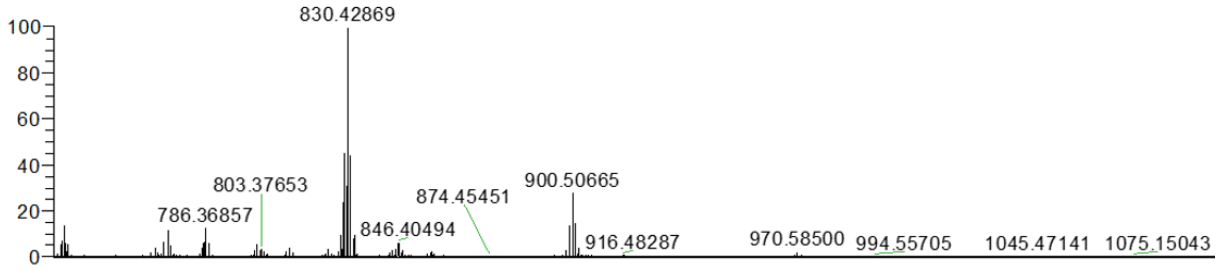

- **phC$_5$-phtmeimb(PF$_6$)$_2$**

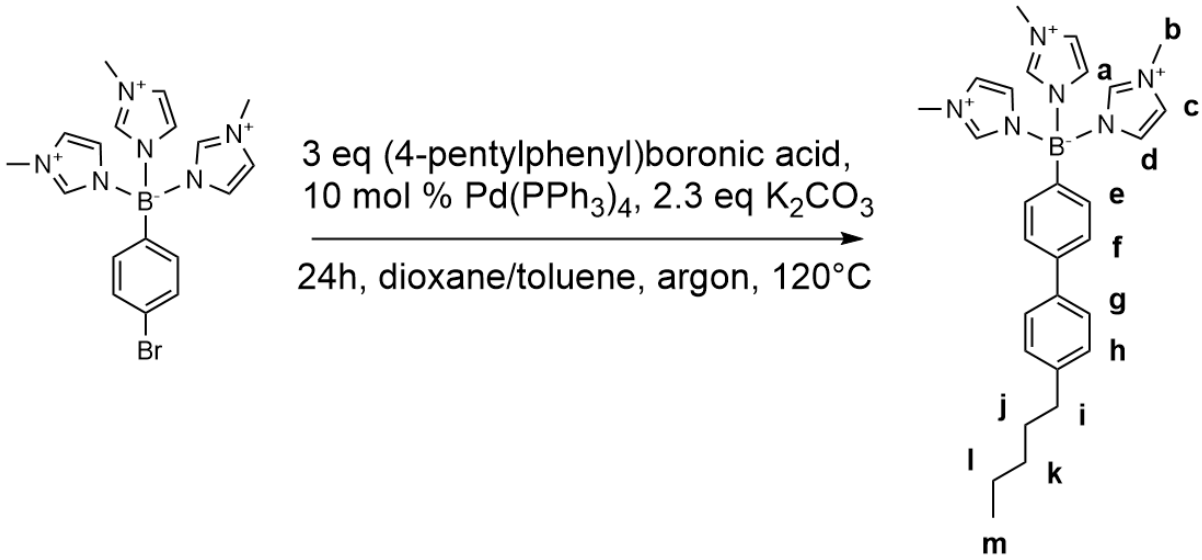

(4-bromophenyl)tris(3-methyl-1H-imidazol-3-ium-1-yl)borate(PF$_6$)$_2$ (598.6 mg, 0.8487 mmol, 1eq), (4-pentylphenyl)boronic acid (491 mg, 2.56 mmol, 3 eq) and potassium carbonate (0.270g, 1.9596 mmol, 2.3 eq) were added to a sealed tube with 7.2 mL of dioxane and 7.2 mL of toluene. The solution was bubbled for 30 minutes with argon before adding the tetrakis(triphenylphosphine)palladium(0) (106.4 mg, 0.092 mmol, 10 mol%) to the solution. The medium was stirred and bubbled 15 more minutes before sealing the tube at 120°C for 24 hours. After that, the black precipitate was filtered, redissolved in a minimum amount of CH_3CN and precipitated in 100 mL of water to yield a black sticky paste. After removing the water overflow and dried the precipitate by vacuum, 3 mL of CH_3CN were used to dissolve the paste which was purified by a 5-cm alumina pad filtration, to yield a colourless solution. This solution was dried under vacuum to yield white crystals. Yield: 8%. ^{1}H NMR (300 MHz, CD_3CN): δ (ppm), 8.02 (s, 3H, a), 7.71 (d, J = 8.19 Hz, 2H, f), 7.62 (d, J = 8.2 Hz, 2H, g), 7.48 (s, 3H, d), 7.31 (d, J = 8.15 Hz, 2H, e), 7.22 (d, J = 8.21 Hz, 2H, h), 7.15 (s, 3H, c), 3.78 (s, 9H, b), 2.65 (t, J = 9.0 Hz, 2H, i), 1.65 (m, 2H, j), 1.35 (m, 4H, k-l), 0.9 (t, J = 6.0 Hz, 3H, m)

^{1}H NMR (300 MHz, CD_3CN, 25°C)

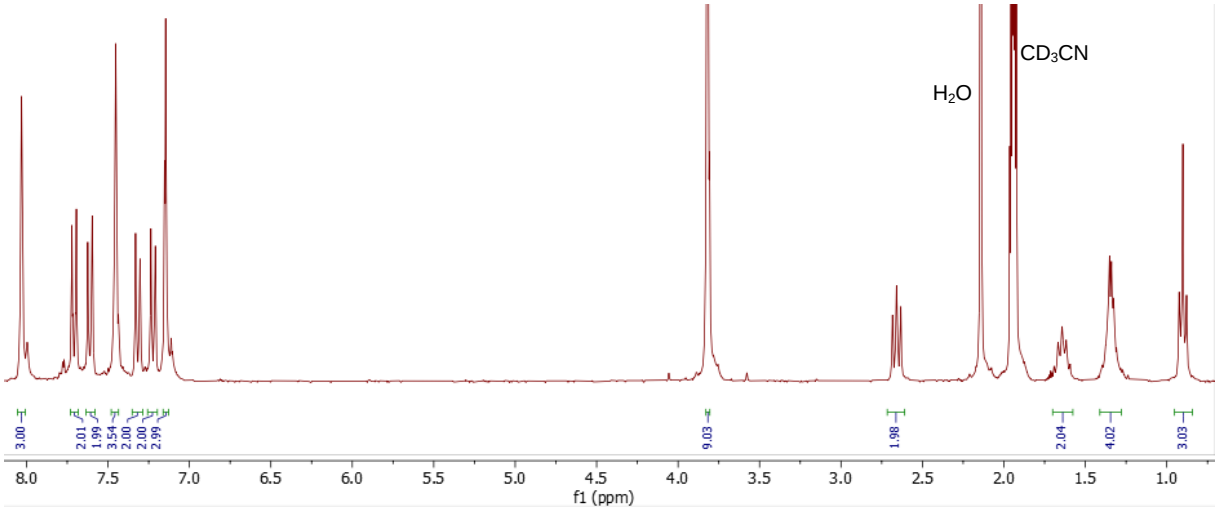

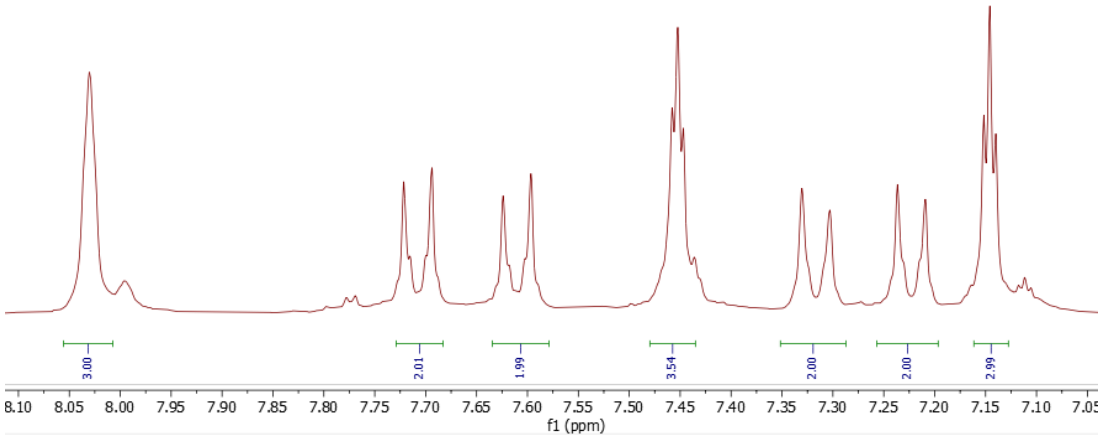

2 DFT Studies

All calculation were done following the computational details on page 52. The yellow-coloured data are calculated from a combination of multiple orbitals not shown hereafter as only the higher orbital coefficient transition was transcribed.

Calculated spectra and associated transitions :

$[Fe(Br\text{-}phtmeimb)_2]^+$

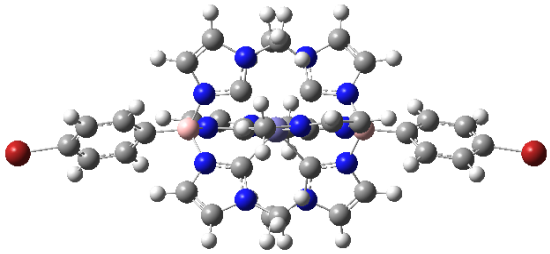

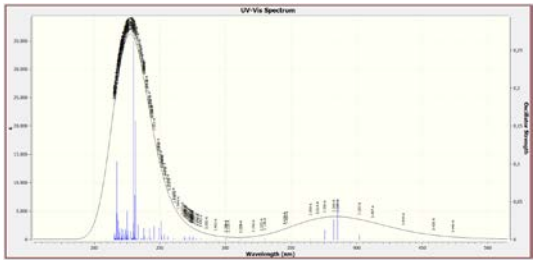

Excited state	Wavelength	Oscillator strength	Starting Orbital	Ending Orbital	Energy of transition (eV)	Type of transition
8	385.4	0.0538	211 A	217 A	3.2170	LLCT
79	231.2	0.1570	213 B	218 B	5.36215	LLCT
82	230.1	0.2625	217 A	218 A	5.3882	LC

(HOMO = 217th orbital)

Excited state	Starting orbital modelling	Ending orbital modelling
8	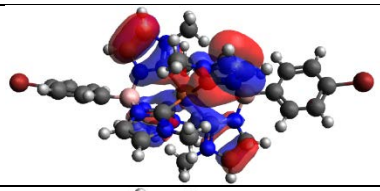	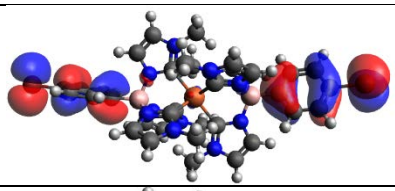
79	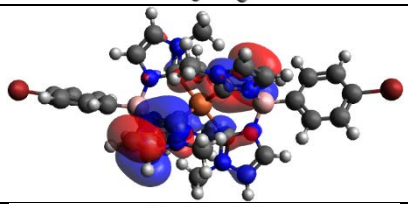	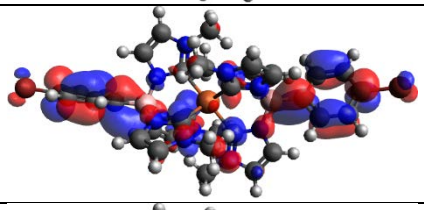
82	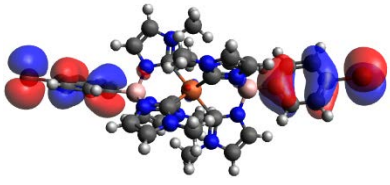	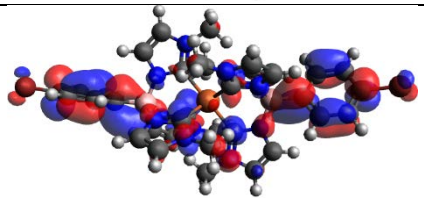

[Fe(phC$_5$-phtmeimb)$_2$]$^+$

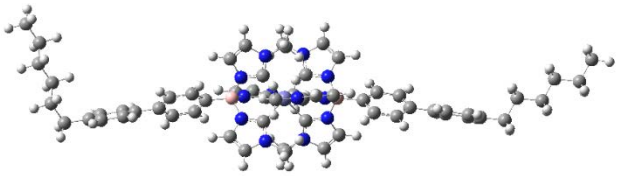

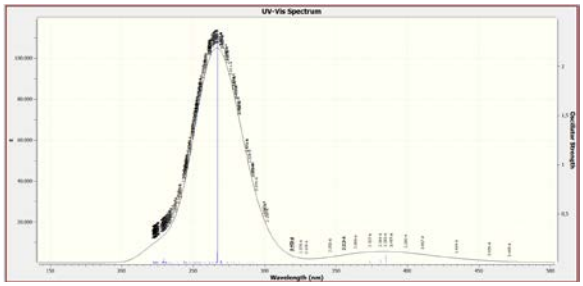

Excited state	Wavelength	Oscillator strength	Starting Orbital	Ending Orbital	Energy of transition	Type of transition
10	384.52	0.082	265B	271 B	3.224 eV	LLCT
50	266.96	2.3383	271A	273A	4,64 eV	LC/LLCT

Homo = 271st orbital

Excited state	Starting orbital modelling	Ending orbital modelling
10		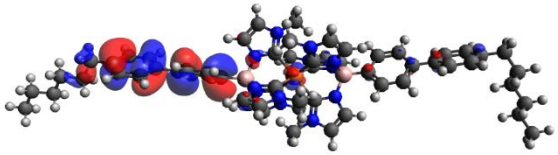
50	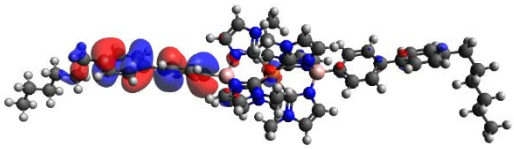	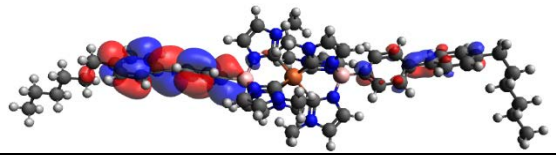

[Fe((PO$_3$H$_2$)-phtmeimb)$_2$]$^+$

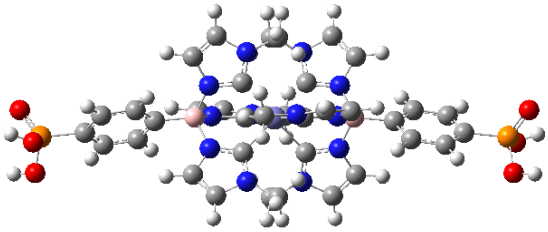

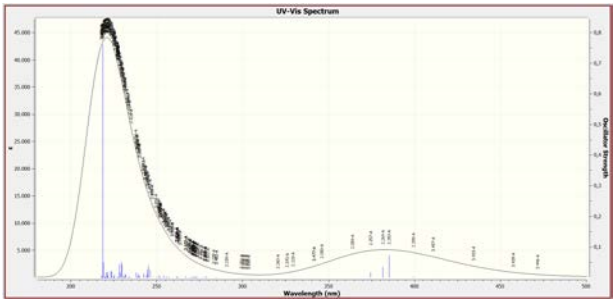

Excited state	Wavelength	Oscillator strength	Starting Orbital	Ending Orbital	Energy of transition	Type of transition
8	385.14	0.0723	219B	223B	3.2192 eV	LMCT/LC
9	381.56	0.0341	217B	223B	3.2494 eV	MLCT
146	218.39	0.761	215A	224A	5.6771 eV	LC

Homo = 223rd orbital

Excited state	Starting orbital modelling	Ending orbital modelling
8	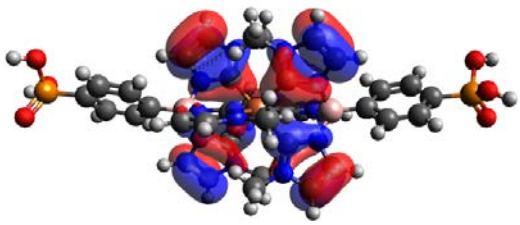	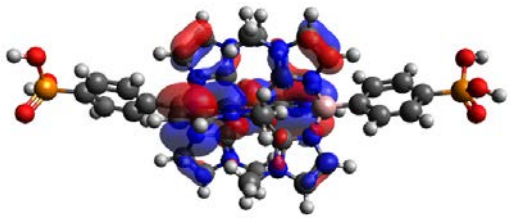
9	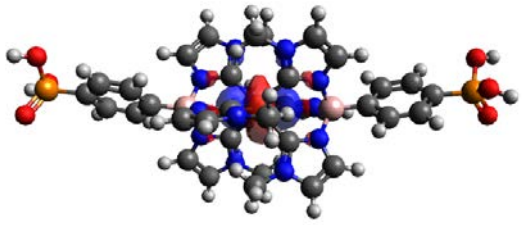	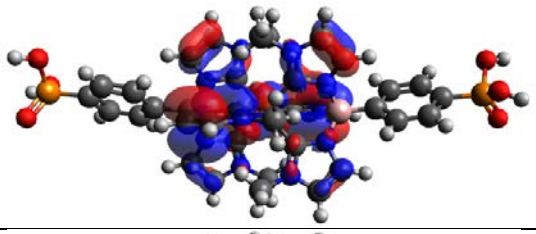
146	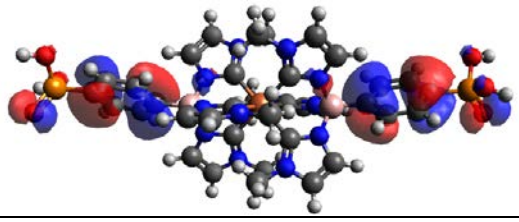	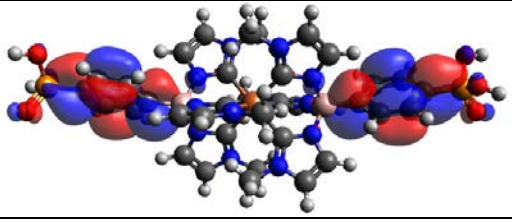

[Fe(C_9-phtmeimb)$_2$]$^+$

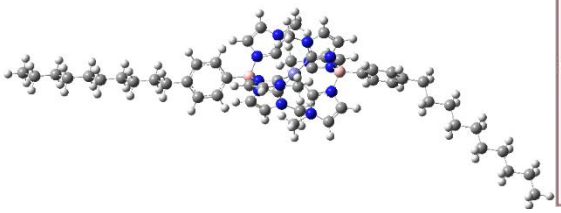

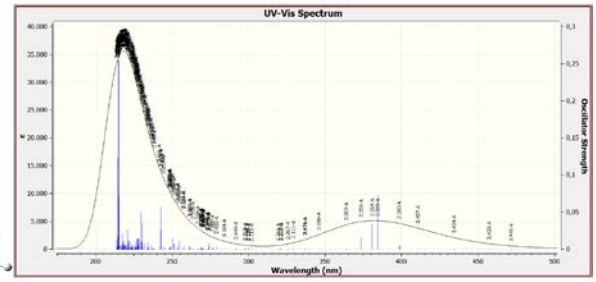

Excited state	Wavelength	Oscillator strength	Starting Orbital	Ending Orbital	Energy of transition	Type of transition
8	384.31	0.0721	259B	263B	3.2261	LMCT
9	380.69	0.0339	257B	263B	3.2568	LMCT
141	214.75	0.2543	256A	264A	5.7734	LC/LLCT
146	214.26	0.1234	257B	266B	5.7866	LC/LLCT

Homo = 263rd orbital

Excited state	Starting orbital modelling	Ending orbital modelling
8	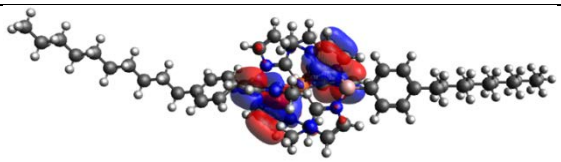	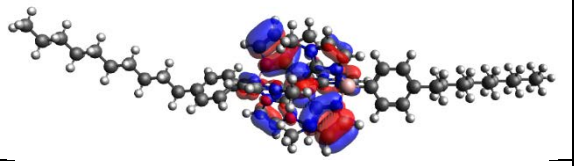
9	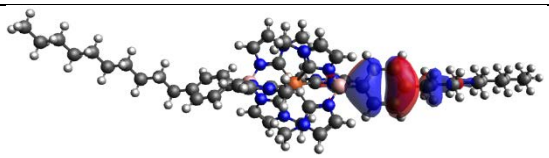	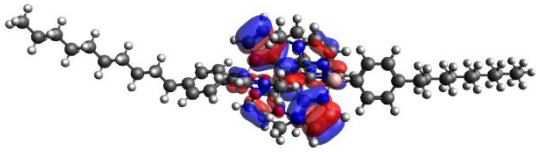
141	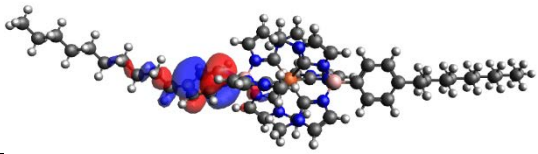	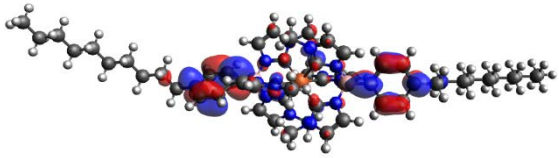
146	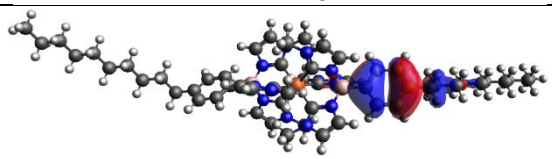	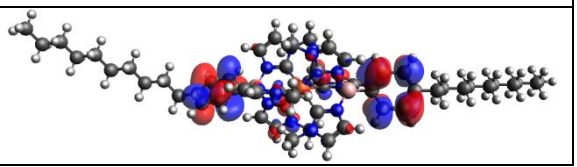

Part VI

REFERENCES

[1] Hannah Ritchie, Max Roser and Pablo Rosado (2022), “Energy”, Our World in Data, consulted the 31/05/2023 on the following link : https://ourworldindata.org/energy-production-consumption.

[2] Hannah Ritchie, Max Roser and Pablo Rosado (2022), “CO_2 and Greenhouse Gas Emissions”, Our World in Data, consulted the 31/05/2023 on the following link : https://ourworldindata.org/co2-emissions.

[3] Hannah Ritchie, Max Roser and Pablo Rosado (2022), “Solar Power Generation 2022”, Our World in Data, consulted the 31/05/2023 on the following link : https://ourworldindata.org/grapher/solar-energy-consumption.

[4] Unknown author, Unknown date of publication, “How a Solar Cell Works”, American Society of Chemistry, consulted the 31/05/2023 on the following link: https://www.acs.org/education/resources/highschool/chemmatters/past-issues/archive-2013-2014/how-a-solar-cell-works.html.

[5] Ranjan, S.; Balaji, S.; Panella, R. A.; Ydstie, B. E. Silicon Solar Cell Production. *Computers & Chemical Engineering* **2011**, *35* (8), 1439–1453. https://doi.org/10.1016/j.compchemeng.2011.04.017.

[6] Gong, J.; Liang, J.; Sumathy, K. Review on Dye-Sensitized Solar Cells (DSSCs): Fundamental Concepts and Novel Materials. *Renewable and Sustainable Energy Reviews* **2012**, *16* (8), 5848–5860. https://doi.org/10.1016/j.rser.2012.04.044.

[7] Klein, M.; Pankiewicz, R.; Zalas, M.; Stampor, W. Magnetic Field Effects in Dye-Sensitized Solar Cells Controlled by Different Cell Architecture. *Sci Rep* **2016**, *6* (1), 30077. https://doi.org/10.1038/srep30077.

[8] Youngblood, W. J.; Lee, S.-H. A.; Kobayashi, Y.; Hernandez-Pagan, E. A.; Hoertz, P. G.; Moore, T. A.; Moore, A. L.; Gust, D.; Mallouk, T. E. Photoassisted Overall Water Splitting in a Visible Light-Absorbing Dye-Sensitized Photoelectrochemical Cell. *J. Am. Chem. Soc.* **2009**, *131* (3), 926–927. https://doi.org/10.1021/ja809108y.

[9] Gao, Y.; Ding, X.; Liu, J.; Wang, L.; Lu, Z.; Li, L.; Sun, L. Visible Light Driven Water Splitting in a Molecular Device with Unprecedentedly High Photocurrent Density. *J. Am. Chem. Soc.* **2013**, *135* (11), 4219–4222. https://doi.org/10.1021/ja400402d.

[10] Wang, D.; Marquard, S. L.; Troian-Gautier, L.; Sheridan, M. V.; Sherman, B. D.; Wang, Y.; Eberhart, M. S.; Farnum, B. H.; Dares, C. J.; Meyer, T. J. Interfacial Deposition of Ru(II) Bipyridine-Dicarboxylate Complexes by Ligand Substitution for Applications in Water Oxidation Catalysis. *J. Am. Chem. Soc.* **2018**, *140* (2), 719–726. https://doi.org/10.1021/jacs.7b10809.

[11] Wang, D.; Hu, J.; Sherman, B. D.; Sheridan, M. V.; Yan, L.; Dares, C. J.; Zhu, Y.; Li, F.; Huang, Q.; You, W.; Meyer, T. J. A Molecular Tandem Cell for Efficient Solar Water Splitting. *Proc. Natl. Acad. Sci. U.S.A.* **2020**, *117* (24), 13256–13260. https://doi.org/10.1073/pnas.2001753117.

[12] Sherman, B. D.; McMillan, N. K.; Willinger, D.; Leem, G. Sustainable Hydrogen Production from Water Using Tandem Dye-Sensitized Photoelectrochemical Cells. *Nano Convergence* **2021**, *8* (1), 7. https://doi.org/10.1186/s40580-021-00257-8.

[13] Zhang, X.; Lei, L.; Wang, X.; Wang, D. Ultrathin TiO2 Blocking Layers via Atomic Layer Deposition toward High-Performance Dye-Sensitized Photo-Electrosynthesis Cells. *Sustainability* **2023**, *15* (9), 7092. https://doi.org/10.3390/su15097092.

[14] Niu, F.; Zhang, P.; Zhang, Z.; Zhou, Q.; Li, P.; Liu, R.; Li, W.; Hu, K. Ultrathin Corrugated Nanowire TiO $_2$ as a Versatile Photoanode Platform for Boosting Photoelectrochemical Alcohol and Water Oxidation. *J. Mater. Chem. A* **2023**, *11* (8), 4170–4182. https://doi.org/10.1039/D2TA09613G.

[15] Pashchenko, D. Natural Gas Reforming in Thermochemical Waste-Heat Recuperation Systems: A Review. *Energy* **2022**, *251*, 123854. https://doi.org/10.1016/j.energy.2022.123854.

[16] Fujishima, A.; Honda, K. Electrochemical Photolysis of Water at a Semiconductor Electrode. *Nature* **1972**, *238* (5358), 37–38. https://doi.org/10.1038/238037a0.

[17] Maeda, K.; Domen, K. Photocatalytic Water Splitting: Recent Progress and Future Challenges. *J. Phys. Chem. Lett.* **2010**, *1* (18), 2655–2661. https://doi.org/10.1021/jz1007966.

[18] Pastore, M. First Principle Modelling of Materials and Processes in Dye-Sensitized Photoanodes for Solar Energy and Solar Fuels. *Computation* **2017**, *5* (4), 5. https://doi.org/10.3390/computation5010005.

[19] Unknown author (2014), ““Solar Radiation and Photosynethically Active Radiation.” Fondriest Environmental Inc, consulted the 31/05/2023 on the following link :https://www.fondriest.com/environmental-measurements/parameters/weather/photosynthetically-active-radiation/.

[20] Campagna, S.; Puntoriero, F.; Nastasi, F.; Bergamini, G.; Balzani, V. Photochemistry and Photophysics of Coordination Compounds: Ruthenium. In *Photochemistry and Photophysics of Coordination Compounds I*; Balzani, V., Campagna, S., Eds.; Topics in Current Chemistry; Springer Berlin Heidelberg: Berlin, Heidelberg, 2007; Vol. 280, pp 117–214. https://doi.org/10.1007/128_2007_133.

[21] Hagfeldt, A.; Grätzel, M. Molecular Photovoltaics. *Acc. Chem. Res.* **2000**, *33* (5), 269–277. https://doi.org/10.1021/ar980112j.

[22] Amy Tikkanen (Unknown date of publication), “Ruthenium”, Britannica, consulted the 31/05/2023 on the following link: https://www.britannica.com/science/bohrium.

[23] Unknown author (2023), “Abundance of elements in Earth’s crust” Wikipedia, consulted the 31/05/2023 on the following link : https://en.wikipedia.org/wiki/Abundance_of_elements_in_Earth%27s_crust.

[24] Unknown author (2023), “Ruthenium price” Umicore, consulted the 31/05/2023 on the following link: https://pmm.umicore.com/en/prices/ruthenium/.

[25] Unknown author (2023), “Iron Ore Prices for the Last Day”, Daily Metal Prices, consulted the 31/05/2023 on the following link: https://www.dailymetalprice.com/metalprices.php?c=fe&u=kg&d=1.

[26] Chen, J.; Browne, W. R. Photochemistry of Iron Complexes. *Coordination Chemistry Reviews* **2018**, *374*, 15–35. https://doi.org/10.1016/j.ccr.2018.06.008.

[27] Darensbourg, M. Y.; Lyon, E. J.; Smee, J. J. The Bio-Organometallic Chemistry of Active Site Iron in Hydrogenases. *Coordination Chemistry Reviews* **2000**, *206–207*, 533–561. https://doi.org/10.1016/S0010-8545(00)00268-X.

[28] Nagashima, H. Catalyst Design of Iron Complexes. *BCSJ* **2017**, *90* (7), 761–775. https://doi.org/10.1246/bcsj.20170071.

[29] Wenger, O. S. Is Iron the New Ruthenium? *Chem. Eur. J.* **2019**, *25* (24), 6043–6052. https://doi.org/10.1002/chem.201806148.

[30] Chen, J.; Browne, W. R. Photochemistry of Iron Complexes. *Coordination Chemistry Reviews* **2018**, *374*, 15–35. https://doi.org/10.1016/j.ccr.2018.06.008.

[31] Sinha, N.; Wenger, O. S. Photoactive Metal-to-Ligand Charge Transfer Excited States in 3d ^{6} Complexes with Cr ^{0} , Mn ^{I} , Fe ^{II} , and Co ^{III}. *J. Am. Chem. Soc.* **2023**, *145* (9), 4903–4920. https://doi.org/10.1021/jacs.2c13432.

[32] Kjær, K. S.; Kaul, N.; Prakash, O.; Chábera, P.; Rosemann, N. W.; Honarfar, A.; Gordivska, O.; Fredin, L. A.; Bergquist, K.-E.; Häggström, L.; Ericsson, T.; Lindh, L.; Yartsev, A.; Styring, S.; Huang, P.; Uhlig, J.; Bendix, J.; Strand, D.; Sundström, V.; Persson, P.; Lomoth, R.; Wärnmark, K. Luminescence and Reactivity of a Charge-Transfer Excited Iron Complex with Nanosecond Lifetime. *Science* **2019**, *363* (6424), 249–253. https://doi.org/10.1126/science.aau7160.

[33] Materna, K. L.; Crabtree, R. H.; Brudvig, G. W. Anchoring Groups for Photocatalytic Water Oxidation on Metal Oxide Surfaces. *Chem. Soc. Rev.* **2017**, *46* (20), 6099–6110. https://doi.org/10.1039/C7CS00314E.

[34] Zhang, L.; Cole, J. M. Anchoring Groups for Dye-Sensitized Solar Cells. *ACS Appl. Mater. Interfaces* **2015**, *7* (6), 3427–3455. https://doi.org/10.1021/am507334m.

[35] Unknown author (2023), “Intermolecular force”, Wikipedia, consulted the 31/05/2023 on the following link : https://en.wikipedia.org/wiki/Intermolecular_force.

[36] Ripak, A.; De Kreijger, S.; Sampaio, R. N.; Vincent, C. A.; Cauët, É.; Jabin, I.; Tambar, U. K.; Elias, B.; Troian-Gautier, L. Photosensitized Activation of Diazonium Derivatives for C–B Bond Formation. *Chem Catalysis* **2023**, *3* (2), 100490. https://doi.org/10.1016/j.checat.2022.100490.

[37] Keglevich, G.; Jablonkai, E.; Balázs, L. B. A “Green” Variation of the Hirao Reaction: The P–C Coupling of Diethyl Phosphite, Alkyl Phenyl- *H* -Phosphinates and Secondary Phosphine Oxides with Bromoarenes Using a P-Ligand-Free Pd(OAc) $_{2}$ Catalyst under Microwave and Solvent-Free Conditions. *RSC Adv.* **2014**, *4* (43), 22808–22816. https://doi.org/10.1039/C4RA03292F.

[38] Prakash, O.; Lindh, L.; Kaul, N.; Rosemann, N. W.; Losada, I. B.; Johnson, C.; Chábera, P.; Ilic, A.; Schwarz, J.; Gupta, A. K.; Uhlig, J.; Ericsson, T.; Häggström, L.; Huang, P.; Bendix, J.; Strand, D.; Yartsev, A.; Lomoth, R.; Persson, P.; Wärnmark, K. Photophysical Integrity of the Iron(III) Scorpionate Framework in Iron(III)–NHC Complexes with Long-Lived ^{2} LMCT Excited States. *Inorg. Chem.* **2022**, *61* (44), 17515–17526. https://doi.org/10.1021/acs.inorgchem.2c02410.

[39] Ayhan, O.; Riensch, N. A.; Glasmacher, C.; Helten, H. Cyclolinear Oligo- and Poly(Iminoborane)s: The Missing Link in Inorganic Main-Group Macromolecular Chemistry. *Chem. Eur. J.* **2018**, *24* (22), 5883–5894. https://doi.org/10.1002/chem.201705913.

[40] Jean, E.; Villemin, D.; Lebrun, L. New Ionic Liquids with Fluorous Anions for Supported Liquid Membranes and Characterization. *Journal of Fluorine Chemistry* **2019**, *227*, 109365. https://doi.org/10.1016/j.jfluchem.2019.109365.

UNIVERSITÉ CATHOLIQUE DE LOUVAIN
Faculté des sciences
Place des sciences, 2 bte L6.06.01, 1348 Louvain-la-Neuve, Belgique | **www.uclouvain.be/sc**